Benedikt Schrode, BSc

Crystal Structure Phase Analysis of C_8O-BTBT-OC_8 Films by Raman and Infrared Spectroscopy

MASTER'S THESIS

to obtain the university degree of
Diplom-Ingenieur
Master's degree programme: Technical Physics

submitted to

Graz University of Technology

Supervisor

Ao.Univ.-Prof. Dipl.-Ing. Dr.techn. Roland Resel

Institute of Solid State Physics

Graz, April 2016

Affidavit

I declare that I have authored this thesis independently, that I have not used other than the declared sources/resources, and that I have explicitly indicated all material which has been quoted either literally or by content from the sources used. The text document uploaded to TUGRAZonline is identical to the present master's thesis.

Date

Signature

Acknowledgements

First I thank my supervisor Roland Resel for making this work possible and the good support throughout the last year. Many thanks to the people of the k-Raum, namely Paul Christian, Andrew Jones, Stefan Pachmajer, Christian Röthel and Magdalena Truger for help with and discussions about problems arising during this project. Thanks also to Katrin Unger and Georg Urstöger from the group of Anna Coclite. I really enjoyed working with all of you.

Furthermore I thank all the people from the institute, especially Robert Schennach and Günther Leising for access to their equipment and discussion of my results, Egbert Zojer for access to his evaporation set-up and Oliver Hofmann for theoretical calculations. I also thank Aldo Brillante, Elisabetta Venuti and especially Tommaso Salzillo from the University of Bologna for making my stay there successful and enjoyable.

Thanks to Boril Chernev, Christian Brandl and Harald Fitzek from FELMI-ZFE Graz for Raman and ATR measurements.

Thanks to the Yves Geerts, Christian Ruzié and Michelle Sferrazza from Université Libre de Bruxelles for providing C_8O-BTBT-OC_8.

Thanks to my parents and brothers for continuous support. Last but not least I want to thank my girl friend, Ingrid. Thank you for your support, the fruitful discussions and proofreading this document.

Abstract

In the field of organic electronics knowledge about the crystal structure of films is of great importance since device relevant properties heavily depend on the crystalline properties. This work is focussed on the molecule dioctyloxy-benzothieno-benzothiophene (C_8O-BTBT-OC_8). Two different crystal structures are known: on the one hand a parallel stacking of the conjugated units (bulk phase) and on the other hand a herringbone packing of the aromatic units. The type of phase which is present within thin films depends on the sample preparation conditions and on the subsequent treatment of the thin film (e.g. solvent vapour annealing). Different concentrations of C_8O-BTBT-OC_8 in o-xylene were used to prepare drop casted and spin coated samples. It is shown that the crystal structure of “as prepared” and solvent vapour annealed drop casted films can be determined by lattice phonon Raman spectroscopy and by infrared spectroscopy in the mid-infrared range. The crystal structure of “as prepared” and annealed spin coated films cannot be identified by Raman spectroscopy due to insufficient film thickness. However, infrared spectroscopy can still be used to determine the present phase. In a subsequent step the crystal structures of C_8O-BTBT-OC_8 powder and crystals prepared by solution processing using highly and less volatile solvents are determined by lattice phonon Raman spectroscopy and attenuated total reflection, an infrared spectroscopy method. The herringbone structure can be related to irregular and small crystals resulting from faster evaporation of the solvent. Crystals with extended size and a more regular shape are found to be in the bulk phase.

Zusammenfassung

Im Arbeitsgebiet der organisches Elektronik ist Wissen über die Kristallstruktur von hoher Bedeutung, da die Eigenschaften elektronischer Bauteile sehr stark von den Kristalleigenschaften abhängen. Die vorliegende Arbeit beschäftigt sich mit dem Molekül Dioctyloxy-Benzothieno-Benzothiophene (C_8O-BTBT-OC_8). Zwei verschiedene Kristallstrukturen sind bekannt: Einerseits eine parallele Anordnung der konjugierten Einheiten (Festkörperphase), andererseits eine Herringbone-Anordnung der aromatischen Einheiten. Die in Filmen vorhandene Phase hängt von den Bedingungen während der Probenherstellung und der darauffolgenden Behandlung des dünnen Films (z. B. „Solvent Vapour Annealing“) ab. Verschieden konzentrierte C_8O-BTBT-OC_8/o-Xylol-Lösungen wurden zur Herstellung von Proben mittels „Drop Casting“ und „Spin Coating“ verwendet. Es wird gezeigt, dass die Kristallstruktur von Proben, die mit „Drop Casting“ hergestellt wurden, mit Hilfe von Ramanspektroskopie im Bereich der Gitterphononen und Infrarotspektroskopie im mittleren Infrarot bestimmt werden kann. Die Kristallstruktur der mit „Spin Coating“ produzierten Proben kann nicht mehr mit Ramanspektroskopie ermittelt werden. Der Grund hierfür ist zu geringe Filmdicke. Allerdings kann mittels Infrarotspektroskopie die vorhandene Phase noch immer bestimmt werden. In einem weiteren Schritt wurden die Kristallstrukturen des einfachen C_8O-BTBT-OC_8-Pulvers und Kristallen, die mit verschieden flüchtigen Lösungsmitteln hergestellt wurden, mit Ramanspektroskopie und „Abgeschwächter Totalreflexion“, einer Methode der Infrarotspektroskopie, bestimmt. Durch schnelleres Verdampfen des Lösungsmittels entstehen unregelmäßige, kleine Kristalle in der Herringbone-Struktur. Größere und regelmäßigere Kristalle liegen in der Festkörperphase vor.

Contents

1 Introduction 15

1.1 Organic Semiconductor 15

1.1.1 C_8O-BTBT-OC_8 16

2 Experimental Methods 19

2.1 Spectroscopy 19

2.1.1 Degrees of Freedom 20

2.1.2 Rotations 20

2.1.3 Vibrations 22

2.2 Introduction to Infrared Spectroscopy 27

2.2.1 Absorption 27

2.2.2 Fourier Transform Infrared Spectrometer 28

2.2.3 Measurement Methods 29

2.3 Introduction to Raman Spectroscopy 33

2.3.1 Raman Scattering 33

2.3.2 Practical Realisation 35

2.4 X-Ray Diffraction and X-Ray Reflectivity 37

2.4.1 Williamson-Hall Analysis 38

2.5 Grazing Incidence X-Ray Diffraction 39

3 Experimental Set-Up 41

3.1 Bruker IFS 66v/S Infrared Spectrometer 41

3.1.1 Transmission Measurements 41

3.1.2 Reflection Measurements 43

3.2 Bomem MB-102 Infrared Spectrometer 43

3.2.1 Solution Measurements 44

3.3 Bruker Tensor 27 Infrared Spectrometer 45

3.4 HORIBA Jobin-Yvon T64000 Triple Monochromator Raman Microscope 45

3.4.1 Alignment of Intermolecular Raman Spectra 45

3.5 PANalytical Empyrean 46

3.6 BESSY KMC-2 Beamline 46

3.7 Sample Preparation . . . 48
    3.7.1 Potassium Bromide (KBr) Pellet . . . 48
    3.7.2 Crystal Growth . . . 48
    3.7.3 Substrate . . . 48
    3.7.4 Drop Casting . . . 48
    3.7.5 Spin Coating . . . 49
    3.7.6 Solvent Vapour Annealing . . . 49

4 Results 51
4.1 Polycrystalline Powder . . . 51
    4.1.1 Raman Spectroscopy . . . 51
    4.1.2 Attenuated Total Reflection Measurements . . . 54
    4.1.3 Potassium Bromide Pellet . . . 54
4.2 C_8O-BTBT-OC_8 in Solution . . . 57
4.3 Crystals . . . 58
    4.3.1 Raman Spectroscopy . . . 60
    4.3.2 Attenuated Total Reflection Measurements . . . 63
    4.3.3 Overview . . . 64
4.4 Drop Casted Films . . . 66
    4.4.1 X-Ray Reflectivity and X-Ray Diffraction . . . 66
    4.4.2 Grazing Incidence X-Ray Diffraction . . . 69
    4.4.3 Raman Spectroscopy . . . 71
    4.4.4 Infrared Reflection Measurements . . . 72
    4.4.5 Infrared Transmission Measurements . . . 74
    4.4.6 Overview . . . 75
4.5 Spin Coated Films . . . 77
    4.5.1 X-Ray Reflectivity and X-Ray Diffraction . . . 77
    4.5.2 Raman Spectroscopy . . . 80
    4.5.3 Infrared Reflection Measurements . . . 81
    4.5.4 Infrared Transmission Measurements . . . 82
    4.5.5 Overview . . . 82
4.6 Heating . . . 84
    4.6.1 Heating Process . . . 84
    4.6.2 Infrared Spectroscopy . . . 86

5 Conclusions 87

Abbreviations and Acronyms 91

List of Figures 93

List of Tables **97**

Bibliography **99**

Appendix **105**
A.1 Calculation of Infrared and Raman Spectra 105

1 Introduction

The ability of one molecule to form two or more different crystal structures is called polymorphism [1]. It is often found in organic semiconductors, e.g. in the benchmark molecule of organic electronics, pentacene [2, 3]. Different reasons for the appearance of polymorphs are discussed: One possibility is a so called substrate-induced phase (SIP). Close to the substrate surface the SIP is present due to improved compatibility with the surface [4]. Other theories suggest metastable phases appearing due to preparation methods far from equilibrium conditions (e.g. crystallisation kinetics [5]).

Knowledge about the crystal structure of films is, due to the dependency of device relevant characteristics on the crystalline properties, of great importance. During this thesis the differentiability of the two known polymorphic forms of C_8O-BTBT-OC_8 [4] by means of infrared (IR) and Raman spectroscopy is investigated. The phase can be easily determined by Raman spectroscopy in the region of lattice phonons (lattice phonon Raman spectroscopy) since intermolecular interactions are probed [6].

However, also the spectral region of intramolecular vibrations obtained by IR spectroscopy allows the identification of the crystal structure in bulk samples [7, 8] as well as thin films [9–11]. Here, absorption of infrared light due to excitation of molecular vibrations is probed.

1.1 Organic Semiconductor

After years of pentacene dominance in the field of organic electronics different types of molecules are coming more and more into focus. One group are benzothienobenzothiophene (BTBT) derivatives, i.e. molecules consisting of a BTBT core with different substituents. Especially symmetrically dialkylated BTBT derivates (C_n-BTBT-C_n, $n = 5 - 14$) were studied recently [12–14]. Advantages of C_n-BTBT-C_n molecules

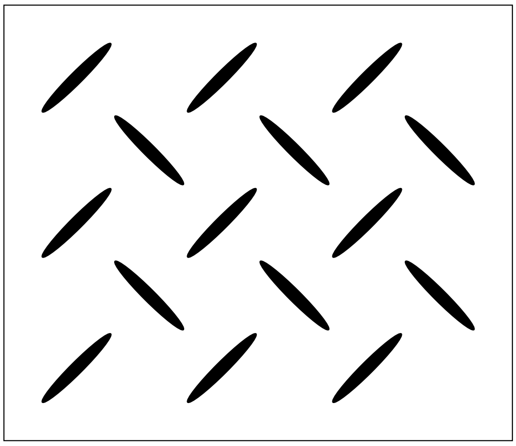

Figure 1.1: Schematic drawing of a herringbone packing, looking down the long axis of the molecule.

are their very good solubility in common solvents (for $n < 12$) [12] and therefore easy fabrication of thin films via e.g. spin coating [12, 14] and drop casting (also variations of the standard method [13]). Furthermore stability in air can be greatly improved [12]. Mobility values of over $1.0\,\mathrm{cm^2\,V^{-1}\,s^{-1}}$ have been reported for organic field-effect transistors produced by spin coating different symmetrically dialkylated BTBT derivatives [12]. Mobilities of up to $5\,\mathrm{cm^2\,V^{-1}\,s^{-1}}$ can be achieved by drop casting C_8-BTBT-C_8 on inclined substrates [13].

All the investigated symmetrically alkylated BTBT derivatives show a herringbone (HB) packing, no different crystal forms could be found [12, 15]. In a HB packing the conjugated cores arrange in a zigzag pattern as schematically shown in Figure 1.1.

1.1.1 C_8O-BTBT-OC_8

In this work a symmetrical BTBT derivative, 2,7-dioctyloxy[1]benzothieno[3,2-*b*]benzothiophene (C_8O-BTBT-OC_8), was investigated. Its molecular structure is shown in Figure 1.2. Additional to the alkyl chains the substituents contain an oxygen atom between the BTBT core and the octyl chain.

In previous research [4] two different crystal structures for this molecule were found: The HB structure, known from the C_n-BTBT-C_n derivatives, and a slipped π-π stacking as bulk form (Figure 1.3). It is described that the HB structure is a SIP. The unit-cell parameters of the two forms are given in Table 1.1. In both cases there are two molecules

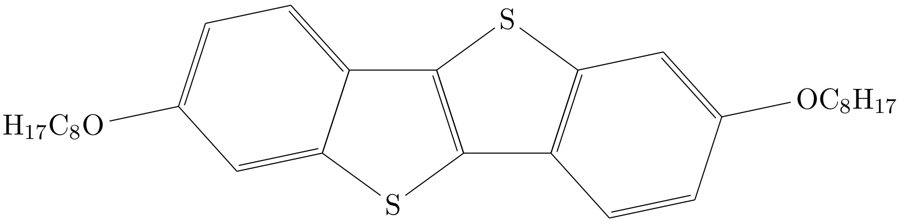

Figure 1.2: Molecular structure of C_8O-BTBT-OC_8 ($C_{30}H_{40}O_2S_2$).

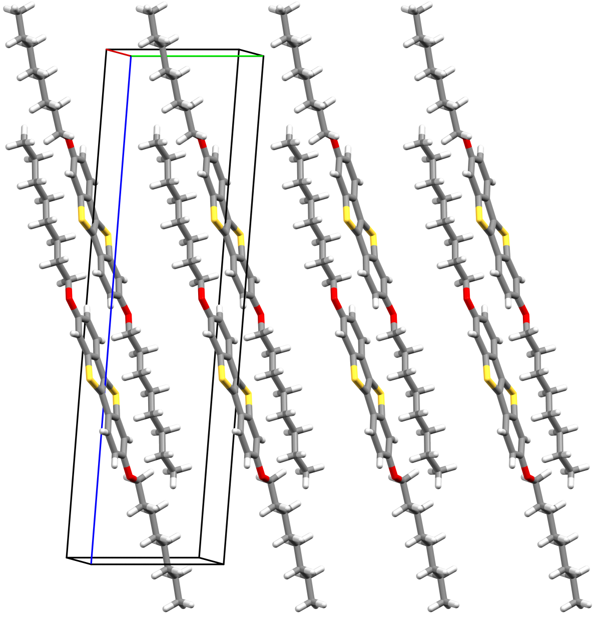

Figure 1.3: Crystal structure and unit cell of the C_8O-BTBT-OC_8 single crystal [4].

Table 1.1: Unit-cell parameters of the two known crystal structures of C_8O-BTBT-OC_8: Single crystal data collected at 123 K, data for the solvent vapour annealed sample (Bulk SVA) at room temperature [4].

	Single Crystal	Bulk SVA	Herringbone
a (Å)	5.5225	5.56	6.02
b (Å)	8.0712	8.27	7.75
c (Å)	31.058	30.89	31.08
α (°)	94.482	96.50	90
β (°)	92.994	93.00	97.00
γ (°)	105.696	107.80	90
ρ (g/cm^3)	1.245	1.233	1.146

in the unit cell. The HB structure is present in as prepared spin coated films. From there two possibilities exist to transfer the sample to the bulk form: Over time the sample goes to the thermodynamically more stable structure. However, this conversion is very slow. After six months storing at room temperature the HB form is still the dominant phase. It is not known if for longer waiting times the sample will turn to bulk completely. The speed of the phase transition can be highly increased by solvent vapour annealing (SVA). In SVA the sample is placed in an environment saturated with solvent vapour which partially dissolves the film, leading to higher molecular order and crystallinity as well as improved organic device performance [16, 17].

2 Experimental Methods

In the following sections short introductions to the theoretical background of IR and Raman spectroscopy are given (based on [18–20], unless mentioned differently). Furthermore, some X-ray scattering techniques are described (based on [21–23]). Images were reproduced or reprinted from the same sources, unless noted.

2.1 Spectroscopy

Spectroscopy describes a wide range of different techniques used in physics, chemistry and many other fields of science to study the interaction of electromagnetic radiation with matter. IR spectroscopy is based on absorption of infrared light due to excitation of different vibrations or rotations of the molecule. Infrared light can only be absorbed when there is a dipole moment change during the vibration or when the molecule has a permanent dipole moment. In case of Raman spectroscopy the incoming photon has a much higher energy than the vibrational levels and gets absorbed when exciting a vibration. A secondary photon is created with an energy corresponding to the energy difference of the incoming photon and the energy needed for the excitation of the vibration. To observe the Raman effect, the transition has to lead to a change of the polarizability of the molecule.

The unit typically used in spectroscopy (first introduced by Johannes Rydberg in the late 1880s [24]) is the wavenumber $\tilde{\nu}$ (number of waves per unit length) in units of inverse centimetres

$$\tilde{\nu}\ [\mathrm{cm^{-1}}] = \frac{10^4}{\lambda\ [\mathrm{\mu m}]} = \frac{1}{10^2}\frac{\nu\ [\mathrm{s^{-1}}]}{c\ [\mathrm{m\,s^{-1}}]}, \tag{2.1}$$

with wavelength λ, frequency ν and speed of light c ($c = 299\,792\,458\,\mathrm{m\,s^{-1}}$ [25]). The term “wavenumber” is typically used for $\tilde{\nu}$ and for the unit of it, $\mathrm{cm^{-1}}$. So “A peak at 2000 wavenumbers” means that there is a peak at $\tilde{\nu} = 2000\,\mathrm{cm^{-1}}$.

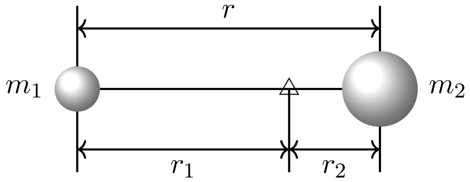

Figure 2.1: Simple mechanical model of two masses at a fixed distance r. The centre of mass is marked by the triangle $\triangle$. The distances between the masses and the centre of mass are r_1 and r_2 respectively.

Energy and wavenumber are related by the following equation:

$$E = h\nu = hc\tilde{\nu}. \tag{2.2}$$

2.1.1 Degrees of Freedom

In a molecule built out of N atoms there are always $3N$ degrees of freedom (DOF). These are divided into translations, rotations and vibrations:

$$\mathrm{DOF}_{\mathrm{trans.}} + \mathrm{DOF}_{\mathrm{rot.}} + \mathrm{DOF}_{\mathrm{vib.}} = 3N. \tag{2.3}$$

Independent of the molecule there are always three translational modes (in x, y and z direction). For vibrations and rotations one has to distinguish between linear and non linear molecules. For non linear molecules (e.g. water), the number of independent rotations is three. Therefore the number of vibrational modes is, according to Equation 2.3, $\mathrm{DOF}_{\mathrm{vib.}} = 3N - \mathrm{DOF}_{\mathrm{trans.}} - \mathrm{DOF}_{\mathrm{rot.}} = 3N - 6$. For linear molecules (e.g. carbon dioxide) only two independent rotations exist, so that there are $3N - 5$ vibrational modes left.

2.1.2 Rotations

The simplest model to describe rotations is shown in Figure 2.1. Two molecules with masses m_1 and m_2 are apart from each other by a fixed distance r. Classically the energy of the rotating system E_{r} can be described by

$$E_{\mathrm{r}} = \frac{1}{2} I \omega^2, \tag{2.4}$$

where I is the moment of inertia and ω the angular velocity. I can be calculated by

$$I = m_1 r_1^2 + m_2 r_2^2 = \frac{m_1 m_2}{m_1 + m_2} r^2 = m_{\mathrm{red}} r^2, \tag{2.5}$$

where the reduced mass m_{red} was introduced. Instead of looking at two rotating masses m_1 and m_2 the system can now be described as a rotation of one mass m_{red} at distance r from the axis. From quantum mechanics it is known that a system like that can only have certain energies. Using $I\omega = \frac{h}{2\pi}\sqrt{J(J+1)}$, where J is the rotational quantum number ($J = 0,\ 1,\ 2,\ \dots$), in the Schrödinger equation gives the following expression for the energies of the rotating system:

$$E_{\mathrm{r}} = \frac{h^2}{8\pi^2 I} J(J+1). \tag{2.6}$$

Dividing by hc gives the following expression for the term diagram:

$$F(J) = \frac{E_{\mathrm{r}}}{hc} = \frac{h}{8\pi^2 c I} J(J+1) = BJ(J+1), \tag{2.7}$$

with the rotational constant B, which is unique for each molecule and only dependent on the moment of inertia. Only transitions between F states with $\Delta J = \pm 1$ are allowed, leading to the following equation for the wavenumber for a transition between two rotational states:

$$\tilde{\nu} = 2B(J+1). \tag{2.8}$$

In reality the distance between the two masses is not constant. For higher J values stretching of the bond due to the centrifugal force has to be considered. Including this changes Equation 2.8 to

$$\tilde{\nu} = B\left[1 - uJ(J+1)\right] J(J+1), \tag{2.9}$$

where u describes the increasing distance between the two masses and $u \ll 1$.

The intensity of rotational lines depends on the transition probability (given by the Hönl-London factor) and the occupation, which is proportional to

$$\exp\left(-\frac{hcBJ(J+1)}{k_{\mathrm{B}}T}\right), \tag{2.10}$$

with the Boltzmann constant k_B and temperature T (Boltzmann distribution) [26].

As one can see from Equation 2.7 the rotational constant B only depends on the moment of inertia I. Therefore from rotational spectroscopy I and information on bond length and angle between atoms in molecules with a permanent dipole moment can be determined. Furthermore the dipole moment can be determined experimentally: In an electric field the rotational levels split due to the Stark effect. The size of the splitting depends on the electric field applied and on the dipole moment.

2.1.3 Vibrations

The vibrational modes of a molecule can be divided into two subgroups: valence and deformational vibrations. In the case of valence vibrations the bond length between the atoms changes periodically whereas the bond angle stays constant. The vibration can either be symmetrically or asymmetrically. For deformational vibrations a periodic change in the bond angle occurs but the bond length stays constant. For molecules with atoms of different masses and low symmetry every possible vibration can lead to absorption at different energies. For molecules with higher symmetry some of the vibrations can have the same frequency and energy, i.e. they are degenerate.

Figure 2.2 shows the different vibrational normal modes for water and carbon dioxide. In a normal mode the vibrating atoms have the same frequency and go through their equilibrium positions at the same time. Furthermore the center of mass stays fixed and the molecule does not rotate.

Carbon dioxide (CO_2) as a linear molecule with $N = 3$ atoms has four vibrational modes, shown in Figure 2.2. There is one symmetric (ν_s) and one asymmetric stretch (ν_{as}). Furthermore two deformational vibrations (δ) occur. However, these are degenerate ($\tilde{\nu}_3 = \tilde{\nu}_4$). CO_2 has two rotational modes. However, rotation around the molecular axis is difficult to excite due to the small moment of inertia. Water (H_2O) is an example of a non linear molecule. Again, one symmetric and one asymmetric stretching but only one deformational vibration can be found. Here no degeneracies occur. Water has three different rotational modes.

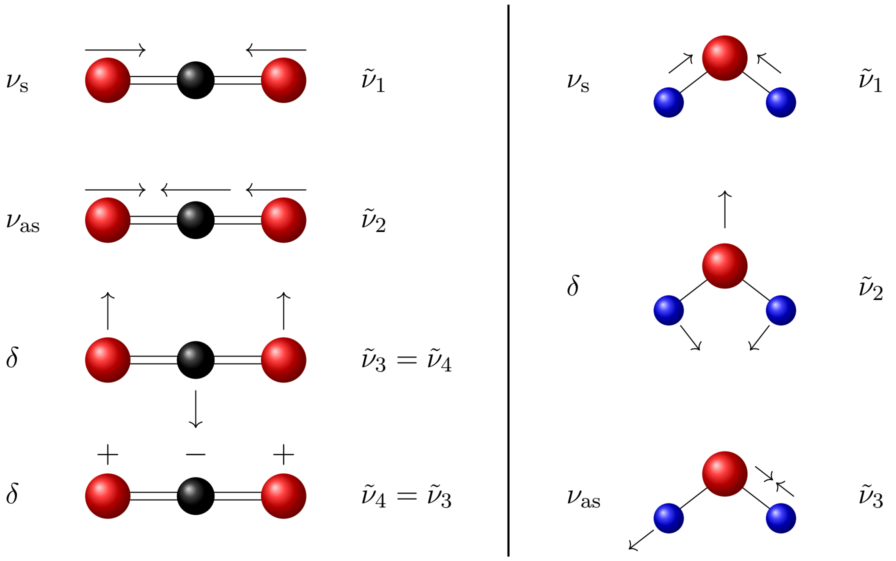
ν_s
$\tilde{\nu}_1$
ν_{as}
$\tilde{\nu}_2$
δ
$\tilde{\nu}_3 = \tilde{\nu}_4$
+
−
+
δ
$\tilde{\nu}_4 = \tilde{\nu}_3$
ν_s
$\tilde{\nu}_1$
δ
$\tilde{\nu}_2$
ν_{as}
$\tilde{\nu}_3$

Figure 2.2: Vibrational normal modes for the linear carbon dioxide (left) and the non linear water molecule (right), divided into valence vibrations ν and deformational vibrations δ. Movement of the atoms in plane are depicted by arrows, out-of-plane movement by + and − signs.

Harmonic Oscillator

The easiest model to understand vibrations of molecules is the model shown in Figure 2.3. Two atoms with masses m_1 and m_2 are connected to each other by a spring with mass zero. The equilibrium distance between the masses is r_0. If the distance between the masses is changed, a force F driving the system back to equilibrium occurs. Assuming that the heavy atom (mass m_2) is stationary and only the light one (mass m_1) moves leads to the oscillator. In the case of the harmonic oscillator the force driving the system back to equilibrium is proportional to the displacement $x = \Delta r$ of the first mass,

$$F = -kx, \tag{2.11}$$

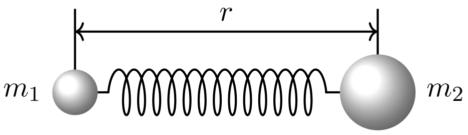

Figure 2.3: Simple mechanical model of two masses connected by a massless spring.

where k is the force constant. The potential resulting in this kind of force,

$$E_{\text{pot}} = \frac{1}{2}k(r - r_0)^2, \tag{2.12}$$

is a parabola with its minimum at the equilibrium distance r_0.

From quantum mechanics it is known that the harmonic oscillator can only absorb quantized energies. These energies $E(v)$ can be calculated by solving the Schrödinger equation with the Hamiltonian of the harmonic oscillator which gives the following eigenvalues (see e.g. [27] for the calculation):

$$E(v) = h\nu\left(v + \frac{1}{2}\right), \ v = 0, \ 1, \ 2, \ \ldots, \tag{2.13}$$

where ν is the classical vibrational frequency and v a quantum number. The minimum energy of the system is $E(v = 0) = 1/2h\nu$. Due to Heisenberg's uncertainty relationship the system cannot have energy $E(v) = 0$ [26]. According to quantum mechanics only transitions with $\Delta v = \pm 1$ are allowed (fundamental transitions). So the energy difference between initial and final state (and because of $\Delta v = \pm 1$ two adjacent states) is $\Delta E = h\nu$.

The vibrational frequency ν of the system is related to the force constant of the bond and the masses of the atoms by

$$\nu = \frac{1}{2\pi}\sqrt{\frac{k}{m_{\text{red}}}}. \tag{2.14}$$

Anharmonic Oscillator

As long as low numbers of v are considered, the harmonic oscillator is a useful model. However, for higher values of v deviations from this simplified picture occur: The energy levels do not go up to high v values with the same spacing. Instead they approach the dissociation energy D where the energy transferred to the molecule is so large that it dissociates [26]. This behaviour can be modelled by introducing an anharmonic potential, e.g. the Morse potential [28],

$$E_{\text{pot}} = D \cdot \left(1 - e^{-a\cdot(x - x_0)}\right)^2. \tag{2.15}$$

Here D is the dissociation energy and a is a constant depending on the molecule.

When using this potential in the Schrödinger equation the vibrational energies are modified by a correction term proportional to $\left(v + \frac{1}{2}\right)^2$:

$$E(v) = h\nu \left(v + \frac{1}{2}\right) - \frac{h^2\nu^2}{4D} \left(v + \frac{1}{2}\right)^2, \tag{2.16}$$

where ν is a function of a and D [26]:

$$\nu = \frac{a}{2\pi}\sqrt{\frac{2D}{m}}. \tag{2.17}$$

Figure 2.4 shows a comparison of the harmonic and anharmonic oscillator potentials and their vibrational energy states. The harmonic oscillator potential is shown in red, the anharmonic in blue. The energy levels (labelled by v) of the harmonic oscillator are equally spaced, these of the anharmonic oscillator approach the dissociation energy D. For low potential energies around the equilibrium distance r_0 the anharmonic oscillator potential can be modelled quite well by the harmonic oscillator potential. For higher values deviations occur.

In addition to the decreasing energy distance with increasing quantum number v, in the case of the anharmonic oscillator not only fundamental transitions are allowed, also transitions with $\Delta v = \pm 2,\ \pm 3,\ \ldots$ are allowed with smaller probability and therefore lower intensity.

Characteristic Frequencies

The result of a spectroscopic measurement is an intensity versus wavenumber plot, usually called spectrum. When the wavelength of the incoming electromagnetic wave matches that of a vibration it gets absorbed and less intensity reaches the detector (see the next section for more details). By comparing the obtained spectra with tabulated literature values or calculations the groups of atoms responsible for a peak at a certain wavenumber can be identified. These characteristic peaks occur when the atoms participating in the vibration have a big difference in mass and therefore only small coupling exists between them. The coupling is, of course, also influenced by the bond type: The valence vibrations frequency of single, double and triple bonds have a

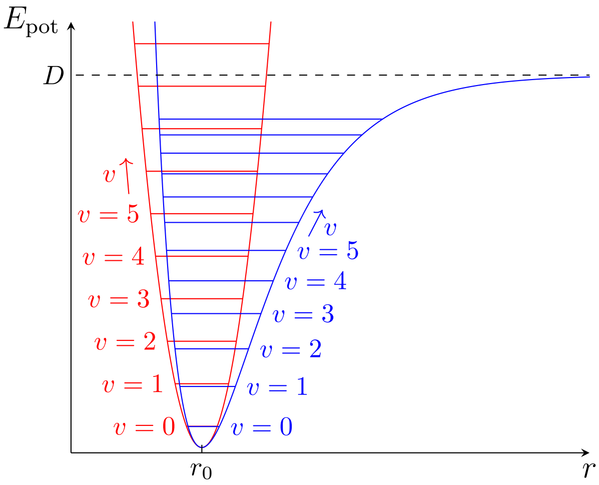

Figure 2.4: Comparison of the potentials of the harmonic (red) and anharmonic oscillator (blue) and their energy levels (labelled by v) [18].

ratio of approximately $1 : \sqrt{2} : \sqrt{3}$.

A special case is the vibration of a hydrogen attached to another atom. Because of the hydrogen's small mass the other atom is basically stationary. Therefore these vibrations are more less independent of the rest of the molecule. One can easily find frequency or wavenumber values indicating the presence of such a group. Similar to that, one can also define different regions in the spectra where other groups have their characteristic frequencies. Nearly every textbook on IR spectroscopy contains this kind of tables (see e.g. [18, 29]).

Water vapour, present in the atmosphere, for example leads to huge absorption between $3500\,\text{cm}^{-1}$ and $4000\,\text{cm}^{-1}$ as well as in the range from $1300\,\text{cm}^{-1}$ to $2000\,\text{cm}^{-1}$. Therefore it is crucial to remove water vapour from the spectrometer set-up, otherwise it will overlap peaks of the sample in that region (e.g. N−H in the higher wavenumber region, and e.g. C=O or C=N in the lower [29]). Usually IR spectrometers are pumped or flushed with dry air where water content was reduced significantly by filtering for that reason. Also the influence of CO_2 on the spectrum is reduced by these methods.

2.2 Introduction to Infrared Spectroscopy

Infrared light is divided into three different regions according to its wavelength: The near-IR ($\lambda = 0.8\,\mu\text{m}$ to $2.5\,\mu\text{m}$ or $\tilde{\nu} = 4000\,\text{cm}^{-1}$ to $12\,500\,\text{cm}^{-1}$), mid-IR ($\lambda = 2.5\,\mu\text{m}$ to $50\,\mu\text{m}$ or $\tilde{\nu} = 200\,\text{cm}^{-1}$ to $4000\,\text{cm}^{-1}$) and far-IR region ($\lambda = 50\,\mu\text{m}$ to $1000\,\mu\text{m}$ or $\tilde{\nu} = 10\,\text{cm}^{-1}$ to $200\,\text{cm}^{-1}$). In these regions excitation of rotations and vibrations, where rotations only occur in gas state samples, have to be considered. Higher energies of the incoming beam can lead to electronic transitions [26].

2.2.1 Absorption

In IR spectroscopy the intensity of the IR beam as a function of the wavenumber $\tilde{\nu}$ is recorded. When the energy of the beam matches that of a vibration of the molecule, energy gets absorbed and less intensity reaches the detector. However, not all vibrations are IR active. Absorption of IR light only occurs when the vibration causes a change of the dipole moment μ, or when the molecule itself has a permanent dipole moment, such as CO, HCl or NO.

Looking back to Figure 2.2 we can check for IR active vibrations. In the case of the symmetric valence vibration of the CO_2 molecule the dipole change due to the vibration in the left half of the molecule cancels that of the right half. So this vibration cannot be measured in IR spectroscopy. All the other vibrations of CO_2 and H_2O are IR active.

The intensity of an IR absorption band is proportional to the square of the dipole moment change

$$I \propto \left(\frac{\partial \mu}{\partial Q}\right)^2, \tag{2.18}$$

where μ is the dipole moment and Q the vibrational amplitude. Furthermore the intensity depends on the concentration of the molecule in the sample (Lambert-Beer law):

$$\log \frac{I_0}{I} = \log \frac{1}{T} = A = abC, \tag{2.19}$$

with I_0 the intensity of the incoming light, I the intensity after passing through the sample, T the transmittance, A the absorbance, a the absorption coefficient, b the sample thickness and C the concentration of the molecule in the sample.

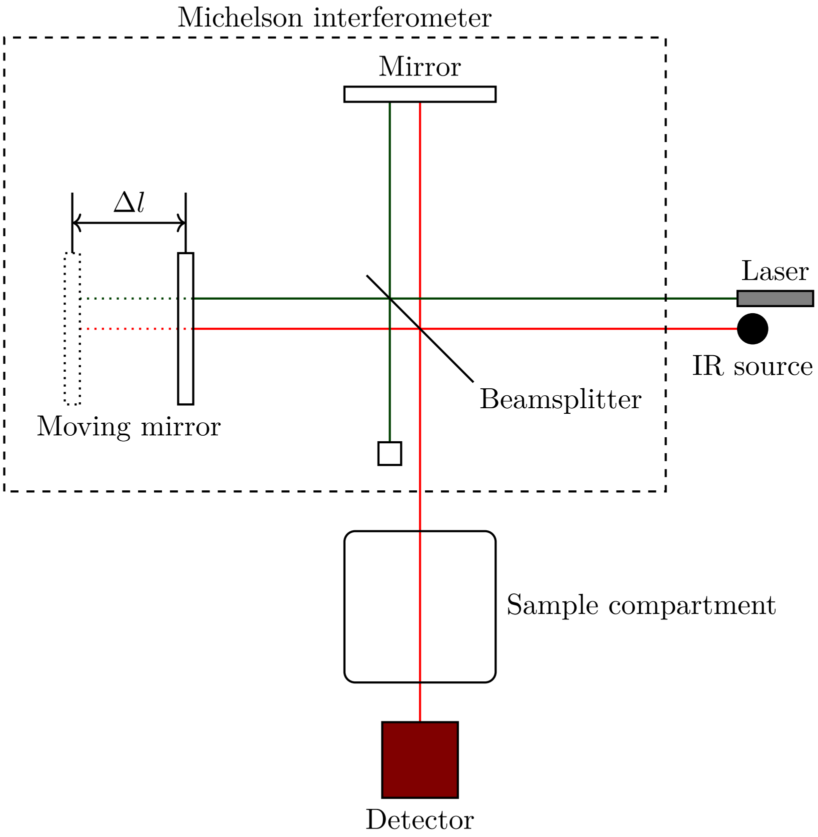
Michelson interferometer
Mirror
Δl
Laser
IR source
Beamsplitter
Moving mirror
Sample compartment
Detector

Figure 2.5: Schematic set-up of an infrared spectrometer with a Michelson interferometer (modified from [30]).

2.2.2 Fourier Transform Infrared Spectrometer

Figure 2.5 shows the basic set-up of an IR spectrometer with a Michelson interferometer. The light goes from the IR source to the beamsplitter where half of it gets reflected to the path to the fixed mirror, the other half is transmitted and goes to the moving mirror. Both components reflect the light back to the beamsplitter where, again half of the intensity is transmitted, the other half is going through. So 50 % of the total intensity is lost because it is going back to the IR source. The other half interferes in the bottom path, goes through the sample compartment and to the detector.

The position of the moving mirror with respect to its zero point is described by Δl. Therefore the path difference between the two beams is $2\Delta l$, the so called optical retardation. Let's assume the IR source emits only one wavelength λ_0. It enters the interferometer and if the optical retardation is zero or an integer times the wavelength ($\Delta l = 0,\ \lambda_0,\ 2\lambda_0,\ \ldots$), the two beams will interfere constructively and maximum intensity will reach the detector. While the mirror moves the intensity will decrease until it reaches its minimum when $\Delta l = \lambda_0/2,\ 3\lambda_0/2,\ \ldots$ So, as long as the speed of the moving mirror is constant the signal at the detector will be sinusoidal. Fourier transforming this signal will give a peak at the incident wavelength λ_0.

In reality a continuous IR source, usually a globar, is used. A globar is a bar made from silicone carbide which emits a spectrum close to that of a black body when heated. The signal at the detector will then be a superposition of all the sinusoidal signals from the different wavelengths. Only at zero retardation all wavelengths will interfere constructively, resulting in a big peak in the centre of the interferogram with fast decreasing intensity to the left and to the right.

To measure the mirror position a laser is used. It will give a sinusoidal signal at the detector from which the optical retardation Δl can be calculated.

Figure 2.6 shows an interferogram and the corresponding spectrum calculated by Fourier transformation. In the interferogram the intensity as a function of the optical retardation is plotted. By Fourier transformation this signal is converted from position to wavenumber space. The calculation was performed with Bruker's IR spectrometer software OPUS. It does not only perform a simple Fourier transform of the data, different corrections are applied before (apodization, phase computation, zerofilling) and afterwards (phase correction) [31]. The x-axis of the interferogram actually ranges from 0 to 21323 with values very close to zero outside of the plotted region. The resulting spectrum is not background corrected. Therefore it contains the wavelength dependent properties of the spectrometer (as discussed in subsection 2.2.3). Typical of an IR spectrum is the inverted x-axis in cm^{-1}, here going from 1.25 µm to 25 µm in wavelength (end of detectable range).

2.2.3 Measurement Methods

When collecting a single-beam IR spectrum the result includes all the wavelength dependent properties of the setup, e.g. the wavelength dependency of the source, beamsplitter, mirrors and detector. To eliminate these, a background or reference spectrum is recorded additionally to the sample spectrum and the final spectrum is

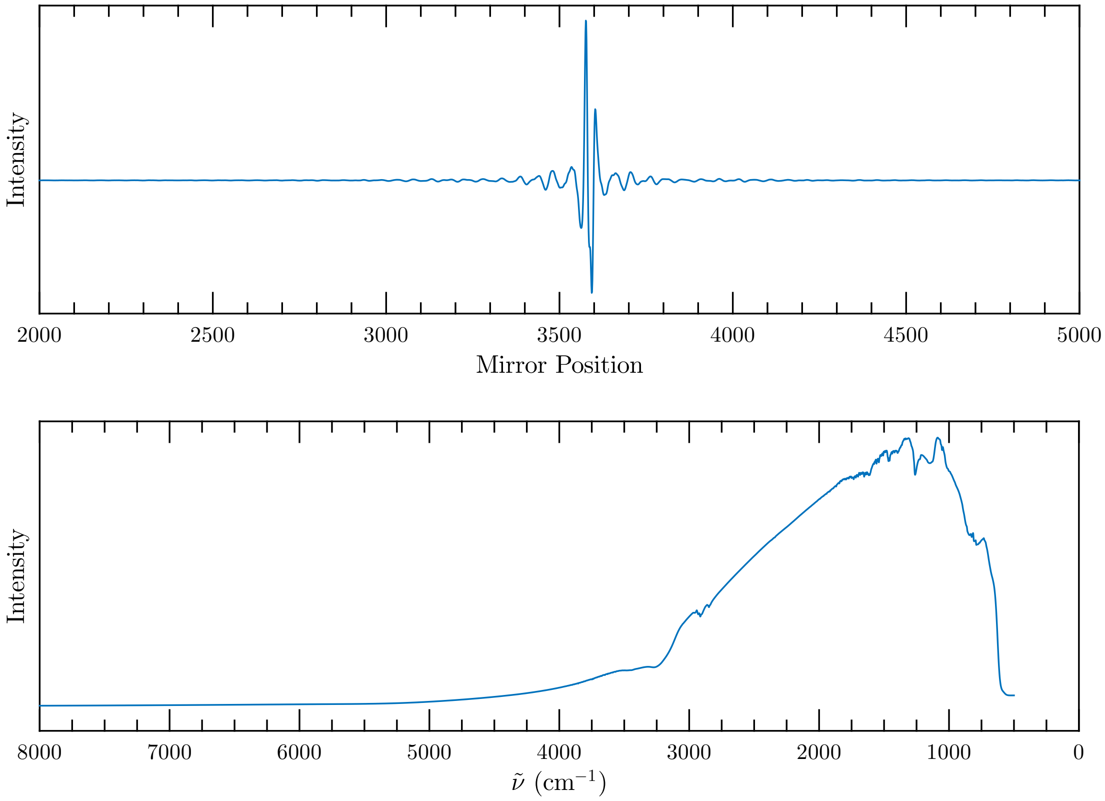

Figure 2.6: Interferogram (top) and resulting infrared spectrum (bottom).

then given by the ratio of the intensity of the sample and the reference measurement:

$$I = \frac{I_{\text{Sample}}}{I_{\text{Background}}} \tag{2.20}$$

Also double-beam IR spectrometer are available. Here the incident beam is divided into two, one going to the sample, the other one is used as reference beam. In the latter beam path the reference sample can be placed. However, the used instruments are single beam spectrometers, making two separate measurements of sample and background necessary.

For thin films on a substrate the background spectrum is usually a clean substrate, for a dissolved sample it normally is the signal of the solvent.

A problem sometimes occurring with samples with parallel surfaces are fringes due to multiple reflections at the boundaries of the sample. Although usually unwanted, because they make interpretation of the spectrum difficult or even impossible, they can be used to determine the sample thickness [32].

Transmission

The easiest way to record an IR spectrum is in transmission. The sample is placed directly in the beam path and the intensity going through is measured at the detector. Of course, this signal has to be divided by the background spectrum to remove wavelength dependencies of the set-up.

Not only solid samples or films can be measured in transmission, with special equipment also absorption measurements of liquids or gases can be performed. Powders can be measured in form of a potassium bromide (KBr) pellet (see subsection 3.7.1 for details) or as Nujol mull.

Reflection

Figure 2.7 shows the schematic set-up of an IR measurement in reflectance. Using mirrors the beam is directed onto the sample, where it reflects off. Then the light is collected by mirrors again and goes to the detector. As incidence angle α usually Brewster's angle of the sample is used because it should give the best signal-to-noise ratio [33]. To fulfil the specular condition the outgoing angle has to be the same as the incident angle.

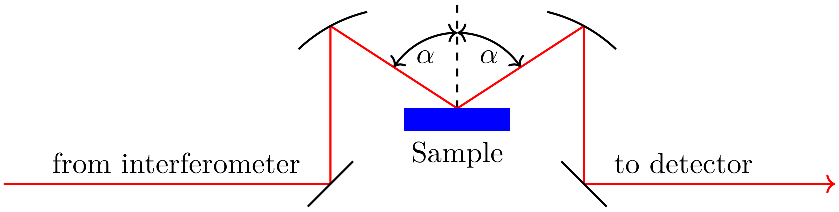

Figure 2.7: Schematic set-up of an infrared reflectance measurement.

Attenuated Total Reflection

In attenuated total reflection (ATR) the sample is placed on an ATR crystal (see Figure 2.8). To ensure good contact between the sample and the crystal pressure is

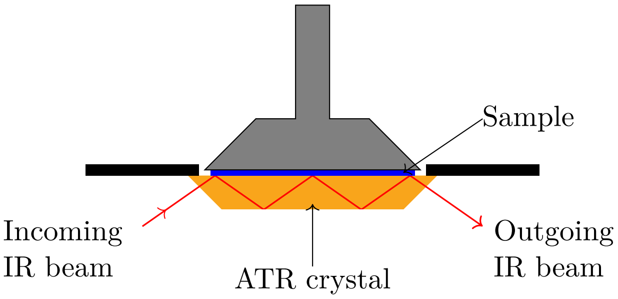

Figure 2.8: Schematic set-up of an attenuated total reflection measurement (reproduced from [34]).

applied. The IR beam is going through the crystal and hits the sample at an angle lower than the critical angle θ_c. An evanescent wave is formed at the crystal-sample interface which can interact with the sample, i.e. it can excite vibrations. The IR beam gets totally reflected but the wavelengths matching one of the vibrational levels have lower intensity now. To increase the signal the IR beam interacts with the sample more often by getting totally reflected at the bottom part of the ATR crystal as well (multi-bounce ATR). To get total reflection the incidence angle θ_i has to be smaller than the critical angle θ_c:

$$\theta_\mathrm{c} = \arcsin\left(\frac{n_2}{n_1}\right), \tag{2.21}$$

where n_1 is the refractive index of the ATR crystal and n_2 that of the sample. To reduce the incidence angle necessary for total reflection the ATR crystal should have a high refractive index. Germanium (Ge), zinc selenide (ZnSe) or diamond are usually used.

The main advantage of the ATR technique is that it can be used without sample preparation. Samples can be solid and liquid. Furthermore, surface phenomena can be studied easily because the wave is decaying exponentially and therefore no bulk signal is recorded.

2.3 Introduction to Raman Spectroscopy

Raman spectroscopy is based on the Raman effect, named after the Indian physicist C. V. Raman. A. Smekal predicted the phenomenon theoretically in 1923 [35], five years later Raman and his colleague K. S. Krishnan confirmed it experimentally in liquids [36], G. Landsberg and L. I. Mandelstam in crystals [37]. Raman was awarded the Nobel prize in physics “for his work on the scattering of light and for the discovery of the effect named after him” [38] in 1930.

2.3.1 Raman Scattering

Raman scattering is an inelastic two photon scattering process. An incoming photon is absorbed and a photon with an energy different from the energy of the absorbed photon is emitted.

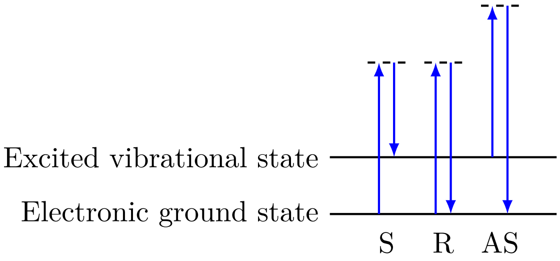

Figure 2.9: Energy levels of the sample and transitions explaining Stokes (S), Rayleigh (R) and anti-Stokes (AS) scattering.

Figure 2.9 shows the energy levels of a sample. The spacing between electronic ground state and excited vibrational state is drawn exaggerated. In Raman spectroscopy the incoming light needs a lower energy than that of an electronic transition. Usually lasers in the optical visible range are used. When the photon hits the sample it can excite it from the ground state to a virtual state (dashed lines). The relaxation process can then go back to the ground state, which leads to the so called Rayleigh scattering. Here the incoming and outgoing photons have the same energy. However, the relaxation can also go to another energy level, e.g. the first vibrational state. Then the outgoing photon has lower energy than the incoming one. This is the Stokes Raman scattering. If an occupied excited state is present when the photon hits the sample, this can also be transferred to a higher virtual state. Then relaxation to the ground state takes place and therefore the incoming photon has a lower energy than the outgoing one. This is anti-Stokes Raman scattering. During this thesis, mainly lattice phonon Raman spectroscopy is applied. Here, the excited states involved in the Raman scattering process are lattice vibrations.

There is an intensity difference between anti-Stokes and Stokes Raman scattering. For anti-Stokes Raman scattering an occupied excited state is required. At room temperature in thermodynamic equilibrium mostly ground states are occupied. Therefore the anti-Stokes process is much less probable. With increasing temperature energetically higher states get populated (described by the Boltzmann distribution) and the intensity of the anti-Stokes lines increase. The intensity ratio can therefore be used to determine temperature.

The intensity of Rayleigh scattering is approximately 10^{-3} less than that of the incoming light. The intensity of Raman scattered light is approximately 10^{-6} that of the incident beam. For a Raman active vibration a change in the polarizability during the vibration is needed. The measured intensity is proportional to the square of this value:

$$I_{\mathrm{R}} \propto \nu^4 I_0 N \left(\frac{\partial \alpha}{\partial Q}\right)^2 . \tag{2.22}$$

Here I_0 is the intensity and ν the frequency of the incoming laser, N the number of molecules in a state able to scatter from, α the polarizability and Q the vibrational amplitude.

Figure 2.10 shows a comparison between Raman scattering, absorption, fluorescence and IR absorption. S_0 and S_1 are the electronic ground and first excited state. The molecule can be in different vibrational states $\nu'' = 0,\ 1,\ 2,\ \ldots,\ \nu' = 0,\ 1,\ 2,\ \ldots$ respectively (the decreasing spacing between them are drawn exaggerated). In the plot no rotational states are included. They would be found at certain energy levels at every vibrational state.

On the left hand side Raman and Rayleigh scattering is shown. Excitation from the ground state to a virtual state and relaxation back to the ground state leads to Rayleigh scattering. When the secondary photon has higher energy than that of the incoming anti-Stokes Raman scattering is observed (left). In the case of Stokes Raman scattering the secondary photon has a lower energy than that of the incoming. If the energy of the exciting light is too high a transition from S_0 to S_1 can occur, leading to fluorescence during relaxation (middle). Usually this light is much more intense than that of Raman scattering making Raman scattering mostly unobservable. Therefore it is very important that no stable excited state is reached during excitation. Using excitation wavelengths close to or at an electronic transition is called resonant Raman spectroscopy [39], but will not be used in this work.

On the right hand side of Figure 2.10 the IR absorption is shown. Here a simple excitation of a molecular vibration is observed.

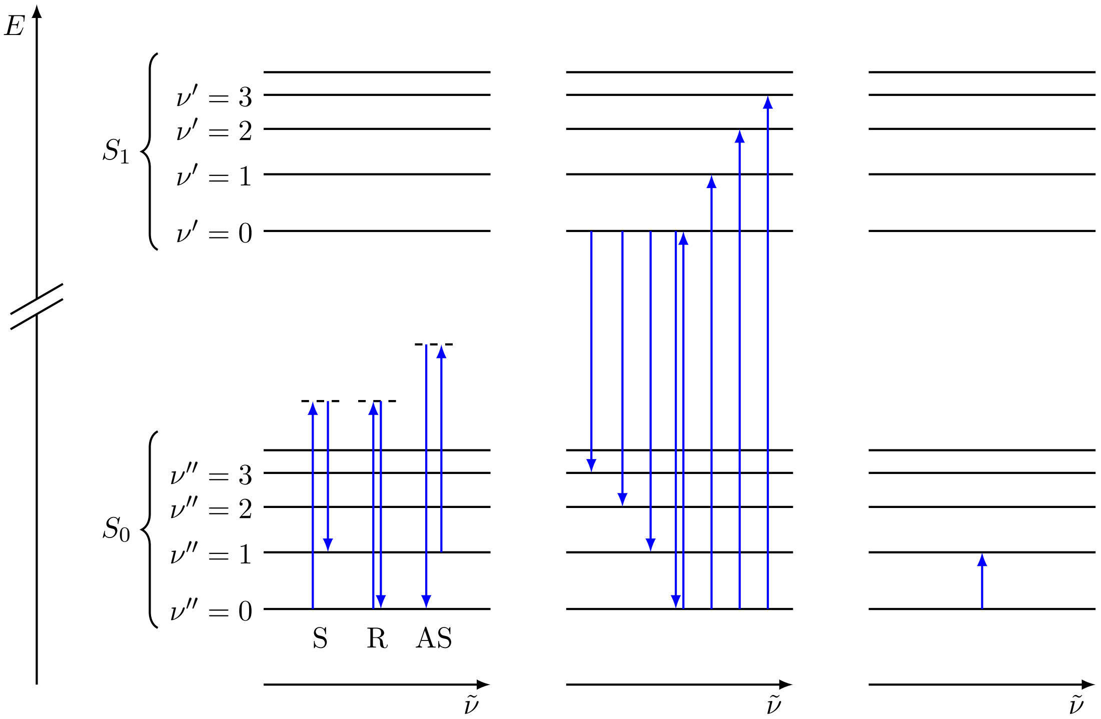

Figure 2.10: Comparison between Raman scattering (left), absorption/fluorescence (middle) and infrared absorption process (right). S_0 and S_1 are the electronic ground and first excited state. ν'' and ν' label the vibrational states. S stands for Stokes Raman scattering, AS for anti-Stokes Raman scattering, R for Rayleigh scattering.

2.3.2 Practical Realisation

The schematic set-up of a Raman spectrometer is quite simple (Figure 2.11). A monochromatic light source with wavenumber $\tilde{\nu}$, usually a laser, shines onto the sample and the scattered light is analysed. Because of the low intensity of Raman scattered light

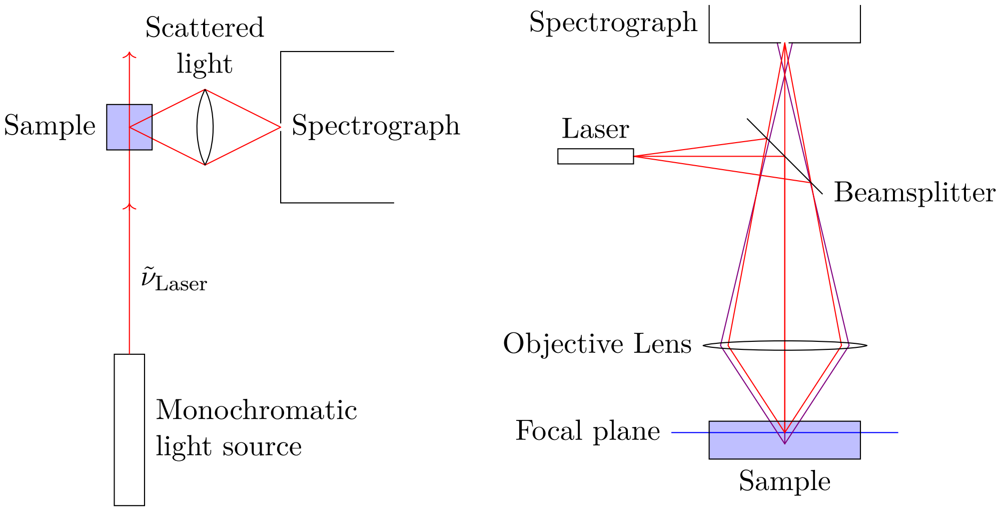
Scattered
light
Sample
Spectrograph
$\tilde{\nu}_{\text{Laser}}$
Monochromatic
light source
Spectrograph
Laser
Beamsplitter
Objective Lens
Focal plane
Sample

Figure 2.11: Schematic set-up of a Raman spectrometer (left) and combination with a microscope (right) [41].

high quality optics are needed for the monochromator. Usually grating monochromators, often more than one, are used. By changing the angle of the grating the wavenumber range can be sweeped.

Often the Raman spectrometer is coupled with a microscope (Figure 2.11). Then spatial resolution is possible. By exploiting confocality of the microscope also depth information can be obtained [40]. Changing the objective lenses shifts the depth of the focal plane. Beams having their focal point outside this plane won't pass through the entrance slit of the spectrograph (purple beam in the right image of Figure 2.11). Usually on the x-axis of Raman spectra the Raman shift is plotted which is defined as difference of the wavenumber of the secondary photon and the incidence laser wavenumber:

$$\text{Raman Shift} = \tilde{\nu} - \tilde{\nu}_{\text{Laser}}. \tag{2.23}$$

2.4 X-Ray Diffraction and X-Ray Reflectivity

In X-ray reflectivity (XRR) and X-ray diffraction (XRD) the sample is illuminated by monochromatic X-rays with wavelength λ. Diffraction occurs when the wavelength of the X-rays is comparable to the lattice constants of the crystal. In the case of XRD the X-rays diffract from planes of atoms. This is described by Bragg's law [42]:

$$\lambda = 2 d_{hkl} \sin\theta, \tag{2.24}$$

where d_{hkl} is the interplanar distance, θ the scattering angle and h, k and l are the Miller indices describing equidistant planes in the crystal. So from knowing the incident wavelength λ and the scattering angle θ the interplanar distance d_{hkl} (Equation 2.25) can be calculated. From the peak width (FWHM, Full Width Half Maximum) the crystallite size perpendicular to the sample surface D can be estimated (Equation 2.26, known as Scherrer equation [43]):

$$d_{hkl} = \frac{\lambda}{2\sin\theta}, \tag{2.25}$$

$$D = \frac{\lambda}{\mathrm{FWHM}\cos\theta}. \tag{2.26}$$

In XRR the angle of incidence is between $\alpha_{\mathrm{i}} = 0°$ and $\alpha_{\mathrm{i}} = 6°$. The beam will reflect optically off the sample surface or the interface between film and substrate (Figure 2.12). The beams then interfere and are detected at an angle $\alpha_{\mathrm{r}} = \alpha_{\mathrm{i}}$. When the incidence angle is θ, the detector has to be at an angle of 2θ to fulfil the specularity condition. For low θ values the beam gets totally reflected until it reaches the critical angle of total external reflection α_{c}. For higher incidence angles one gets angle dependent interferences, so called Kiessig fringes [44]. From the periodicity of these the film thickness can be determined (for $0\,\mathrm{nm} < d_{\mathrm{film}} \leq 200\,\mathrm{nm}$). However, these fringes do not occur for very rough surfaces. The roughness can be determined from the drop of the signal after the critical angle (Figure 2.12). Here two critical angles are visible due to the substrate and the film.

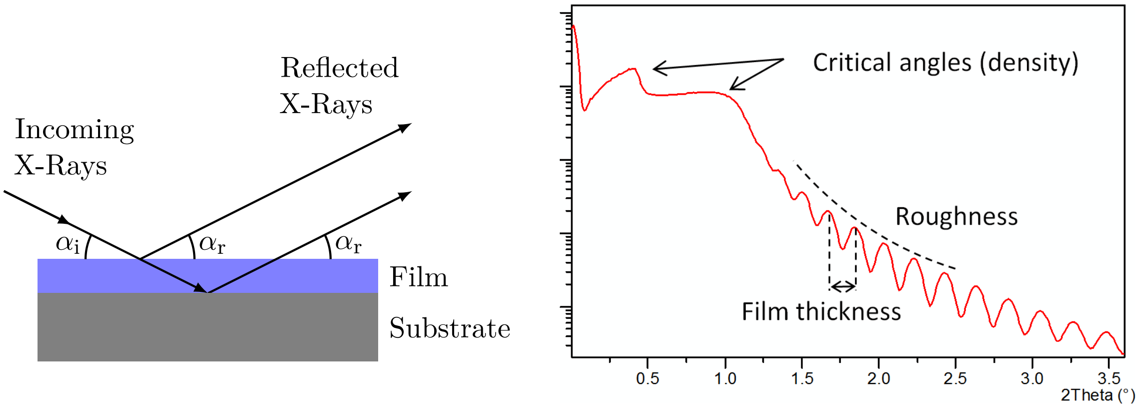
Reflected X-Rays
Incoming X-Rays
α_i
α_r
α_r
Film
Substrate
Critical angles (density)
Roughness
Film thickness
0.5
1.0
1.5
2.0
2.5
3.0
3.5
2Theta (°)

Figure 2.12: Beam paths in an X-ray reflectivity measurement (left) (reproduced from [23]) and resulting diffraction pattern and information gained from it (right).

2.4.1 Williamson-Hall Analysis

The width of a peak in an XRR pattern depends on two parts, the size and the strain broadening. Williamson and Hall suggest that the overall peak broadening $\Delta(2\theta)$ can be written as a sum of the two individual contributions [45]:

$$\Delta(2\theta) = \underbrace{\frac{\lambda}{L\cos\theta}}_{\text{Size Broadening}} + \underbrace{2\frac{\Delta a}{a}\tan\theta}_{\text{Strain Broadening}} . \tag{2.27}$$

Multiplying by $\cos\theta$ gives

$$\Delta(2\theta)\cos\theta = \frac{\lambda}{L} + 2\frac{\Delta a}{a}\sin\theta. \tag{2.28}$$

Comparing the last equation with the standard form of a linear function $y = kx + d$ gives the following result:

$$k = 2\frac{\Delta a}{a} \quad \text{and} \tag{2.29}$$

$$d = \frac{\lambda}{L}. \tag{2.30}$$

The graphical representation of the Williamson-Hall analysis is shown in Figure 2.13.

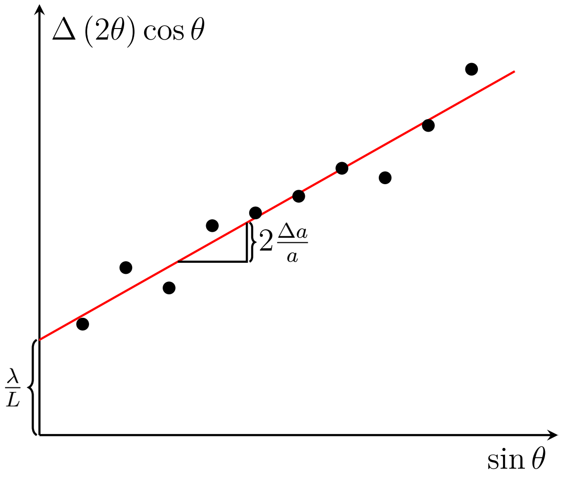

Figure 2.13: Graphical representation of a Williamson-Hall analysis. Dots represent the $\Delta(2\theta)\cos\theta$ values of the peaks in the X-ray diffraction measurement, the red line is a linear fit.

2.5 Grazing Incidence X-Ray Diffraction

In grazing incidence X-ray diffraction (GIXD) the angle of incidence of the X-rays is very small, usually close to the critical angle θ_c of the sample. When the beam hits the sample an evanescent wave which decays exponentially in the sample, is formed. Therefore the penetration depth of the beam is limited, no bulk signal is recorded and a surface sensitive investigation is possible. The peak pattern can then be related to the crystal structure of the film. The difference to specular X-ray diffraction is that in GIXD the in-plane order can be investigated as well, whereas in specular XRD only the out-of-plane properties are accessible.

3 Experimental Set-Up

This chapter describes the equipment used during this thesis. Furthermore additional information on the preparation of samples is given.

3.1 Bruker IFS 66v/S Infrared Spectrometer

Most of the IR spectra were recorded using a Bruker IFS 66v/S IR spectrometer (Figure 3.1) with Bruker's spectroscopy software OPUS, version 4.2. The spectrometer was equipped with a liquid nitrogen cooled mercury cadmium telluride (MCT) photodetector (InfraRed Associates Inc., Model D316/6). In this kind of detector the incoming electromagnetic wave can excite an electron to the conduction band of the semiconducting detector material, leading to an increased conductivity. This change can be measured with a bias current [46]. Mirror position was determined by a He-Ne laser. To avoid absorption signals due to carbon dioxide and water vapour in the air [47] the IFS 66v/S was pumped using a rotary vane pump. Measurements were started at a pressure of 7 mbar. If necessary the spectra were transformed to absorption spectra using OPUS' built in transmission to absorption converter. Further details on the applied OPUS settings are given in Table 3.1.

3.1.1 Transmission Measurements

For transmission measurements (see Figure 3.2) a primary-side aperture of 9 mm and a secondary-side aperture of 8 mm in diameter was used. The secondary aperture is directly mounted on the sample holder.

Table 3.1: Main OPUS settings used for recording infrared spectra with the Bruker IFS 66v/S.

Option	Value
Resolution	4 cm^{-1}
Measurement time	10 min
Beam splitter	KBr
Mirror speed	100 kHz
Acquisition mode	Double Sided, Forward-Backward
Low-pass filter	Open
Phase resolution	16
Phase correction mode	Mertz
Apodisation function	Triangular
Zerofilling factor	8

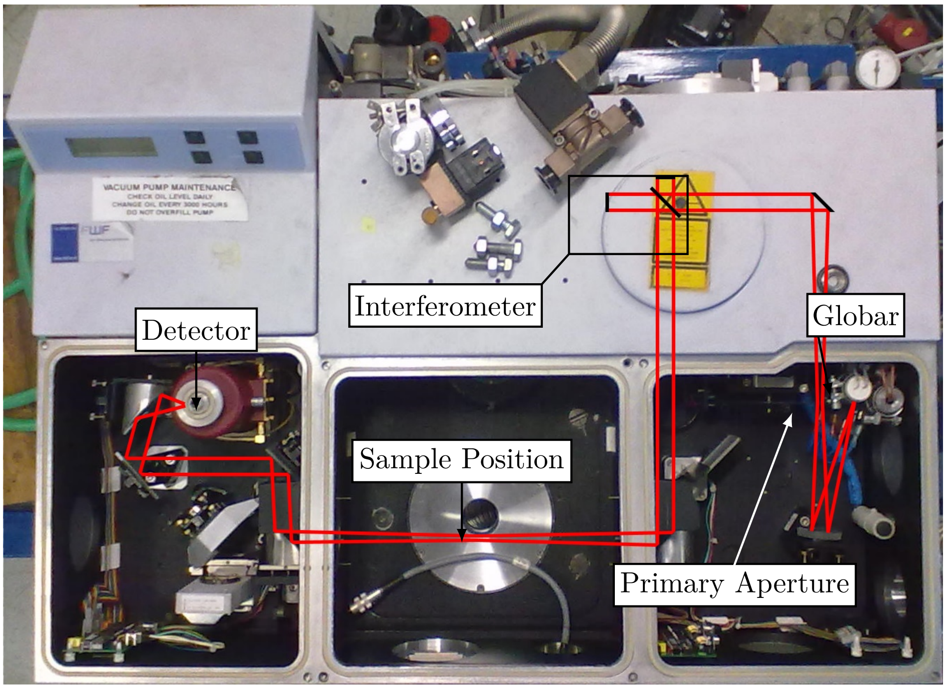
Interferometer
Globar
Detector
Sample Position
Primary Aperture
VACUUM PUMP MAINTENANCE
CHECK OIL LEVEL DAILY
CHANGE OIL EVERY 3000 HOURS
DO NOT OVERFILL PUMP

Figure 3.1: Drawing of the beam path in the Bruker IFS 66v/S. The interferometer part is not visible due to the cover.

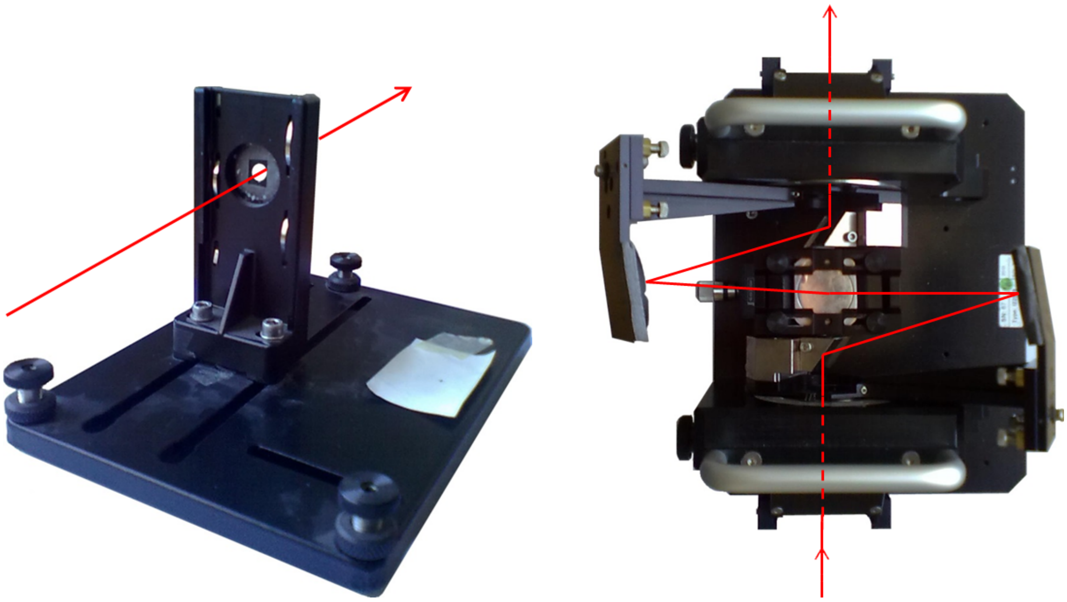

Figure 3.2: Used transmission (left) and reflection set-up (right) for the Bruker IFS 66v/S infrared spectrometer.

3.1.2 Reflection Measurements

For reflection measurements (see Figure 3.2) an aperture of 6 mm in diameter was used on the primary, no aperture on the secondary side. Because Brewster's angle of C_8O-BTBT-OC_8 is not known, the incidence and outgoing angles could not be set to it (as suggested in [33]). Instead Brewster's angle of the substrate was used, $\alpha_\mathrm{B} = 57°$.

3.2 Bomem MB-102 Infrared Spectrometer

IR spectra of the liquids were recorded using a Bomem MB-102 IR spectrometer. Instead of pumping to avoid absorption due to water and carbon dioxide the machine is flushed with H_2O and CO_2 filtered air. Furthermore the spectrometer is equipped with a different type of interferometer. Both mirrors are mounted on an oscillating arm resulting in an optical retardation between the two paths (see Figure 3.3). To ensure that the reflected beam is parallel to the incoming one cube corner mirrors are used. Another difference to the Bruker IFS 66v/S is that the signal is recorded with a pyroelectric detector. The incoming electromagnetic wave results in a temperature gradient across

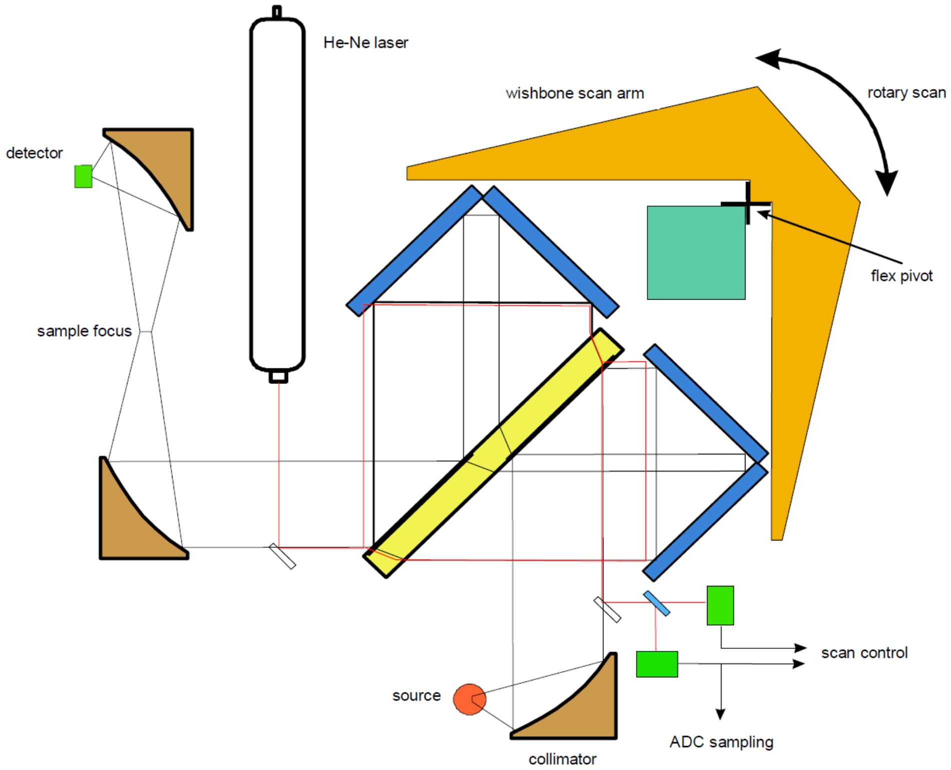
He-Ne laser
wishbone scan arm
rotary scan
detector
flex pivot
sample focus
scan control
source
ADC sampling
collimator

Figure 3.3: Schematic of the beam paths in a Bomem MB-102 infrared spectrometer [48]. Instead of the typical Michelson interferometer two mirrors are mounted on the oscillating wishbone scan arm resulting in a path difference.

the pyroelectric material leading to a polarization change in the detector material. This can be measured as a current [46]. The beam splitter is made from caesium iodide with a semiconductor coating. With the equipment available this spectrometer can only be used in transmission mode.

3.2.1 Solution Measurements

To record spectra of liquids a Specac demountable IR cell with potassium bromide (KBr) windows from “Korth Kristalle” was used. KBr is often used in IR set-ups due to its very high transmittance in this spectral range [18]. For both, the sample and the background spectrum 32 scans with a resolution of $4\,\mathrm{cm}^{-1}$, were measured.

3.3 Bruker Tensor 27 Infrared Spectrometer

ATR spectra were recorded using a Bruker Tensor 27 IR spectrometer with a RockSolid interferometer at Felmi ZFE, Graz. It was equipped with a MIRacle single bounce ATR element, using diamond as the ATR crystal. In a single bounce ATR set-up the electromagnetic wave interacts with the sample only once, not multiple times as shown in Figure 2.8. For detection of the IR radiation a DigiTect deuterated L-alanine doped triglycine sulfate (DLaTGS) detector system was used. DLaTGS is a pyroelectric material. The incoming IR beam creates a temperature gradient in the detector material resulting in a polarisation change and finally a measurable current [46]. Data collection was performed with OPUS as well.

3.4 HORIBA Jobin-Yvon T64000 Triple Monochromator Raman Microscope

The Raman spectra were collected with a HORIBA Jobin-Yvon T64000 Triple Monochromator Raman Spectrometer attached to an Olympus BX40 microscope equipped with 10 x, 20 x, 50 x and 100 x objectives (Figure 3.4) at the “Dipartimento Chimica Industriale ‘Toso Montanari’ ” at the University of Bologna, Italy. Optical microscopy images were taken by a JVC TK-C701EG. As incidence light a 647.1 nm Krypton laser (COHERENT Innova 90C) was used. At the beginning a liquid nitrogen cooled charge-coupled device (CCD) detector (operating temperature of −134 °C) was used which was changed to a CCD detector with a Peltier cooler (operating temperature of −60 °C) later. Using a polariser directly after the laser and an analyser in front of the entrance slit of the spectrograph the polarisation effects by the sample could be studied. Unless mentioned differently, no analyser was used and the incident laser beam was polarised horizontally. The spectrometer was operated with HORIBA’s LabSpec software.

3.4.1 Alignment of Intermolecular Raman Spectra

Due to the set-up used, recorded Raman spectra have to be shifted along the x-axis to ensure the correct peak positions. For films on silicon oxide this is quite simple because

SiO_x has a prominent peak at 21 cm^{-1}. For samples without a substrate (e.g. crystals or powder) lines of a neon lamp [49] were used for calibration. The 6506.5281 Å line gives rise to a peak at a Raman shift of 84 cm^{-1}. With the difference between this number and the measured Raman shift also crystal and powder spectra can be aligned.

3.5 PANalytical Empyrean

XRR and XRD measurements were performed on a PANalytical Empyrean in $\theta/2\theta$ mode. As X-ray source a water cooled copper tube with a working point of 40 mA and 40 kV and a wavelength of 1.54 Å was used. The PANalytical was equipped with a nickel beam attenuator, which was placed in the beam path automatically if the intensity at the detector exceeds a certain value. To make the individual X-ray beams parallel to each other an X-ray mirror was used. On the primary side a 1/32° slit and a 10 mm beam mask were used. On the secondary side a 0.1 mm anti scatter slit and 0.02 rad Soller slits were mounted. As a detector a PIXcel3D 1x1 detector in receiving slit mode was used. Three channels were active during the measurements resulting in an active length of 0.165 mm. A DHS 900 from "Anton Paar" was used as sample stage, even if not heating. For heating a graphite dome can be placed over the sample and flushed with nitrogen to avoid oxidation.

During heating XRR patterns of the (001) peak were recorded from $2\theta = 1.5°–4.5°$ with a step size of $\Delta\theta = 0.025°$ and 2.64 s data collection time per step. The range from 0° to 16° was measured with a step size of 0.01° and 0.44 s collection time per step.

3.6 BESSY KMC-2 Beamline

GIXD patterns were recorded at the KMC-2 beamline at BESSY II, Berlin, with X-rays of a wavelength of 1.00 Å and an incidence angle of approximately 0.12°. The beamline was equipped with a 2d cross-wire detector from Bruker. Reciprocal space conversion was performed with the *xrayutilities* software package [50].

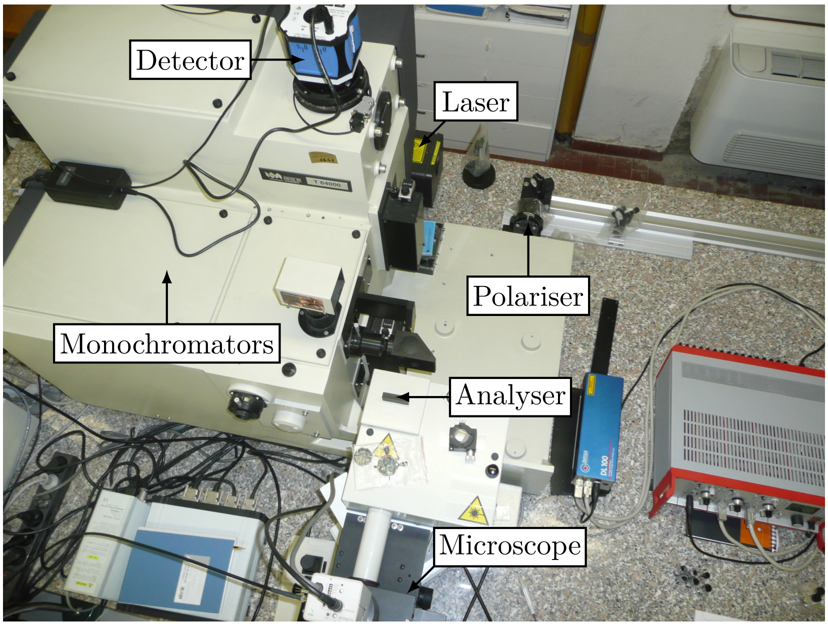
Detector
Laser
Polariser
Monochromators
Analyser
Microscope

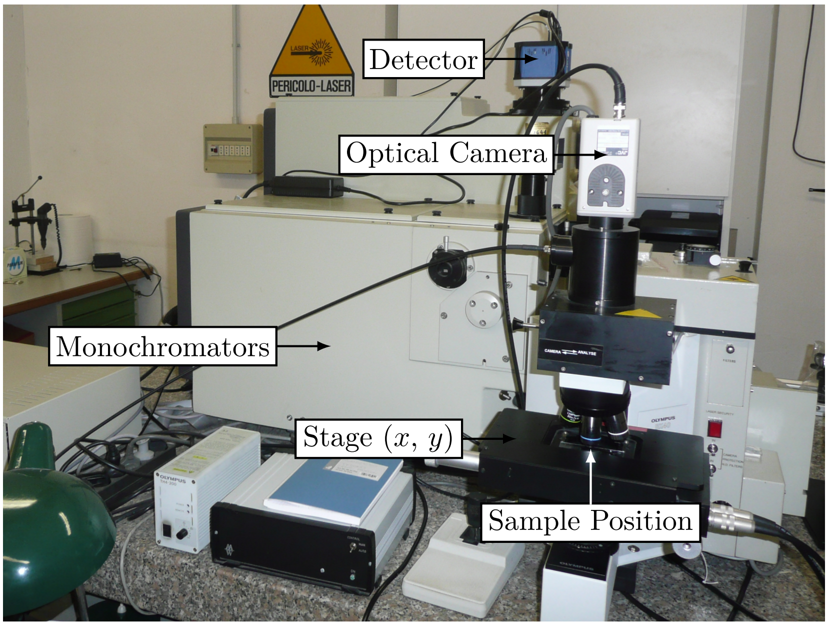
PERICOLO-LASER
Detector
Optical Camera
Monochromators
Stage $(x,\ y)$
Sample Position

Figure 3.4: Images of the HORIBA Jobin-Yvon T64000 Triple Monochromator Raman microscope equipped with the detector with Peltier cooling. The monochromators and the analyser cannot be seen due to the cover.

3.7 Sample Preparation

All samples, except for the single crystals, were prepared at the organic semiconductors lab at the "Institute of Solid State Physics", Graz University of Technology. The single crystals were grown at the University of Bologna.

3.7.1 Potassium Bromide (KBr) Pellet

A standard technique used to collect IR spectra of powders is embedding the substance in a matrix of IR transparent material, usually KBr. The KBr pellet with a diameter of 13 mm was produced by mixing approximately half a gram of KBr with a small amount of C_8O-BTBT-OC_8, grinding it gently and pressing it in a mechanical press at eleven tons for three minutes. For the background spectra a pure KBr pellet was produced following the same procedure.

3.7.2 Crystal Growth

Crystals were grown by dissolving C_8O-BTBT-OC_8 in different solvents (close to saturation concentration) and evaporation of the solvent. To influence the evaporation speed the vial was either uncovered or covered by Parafilm with a small hole in it.

3.7.3 Substrate

As substrates for the films 2 cm × 2 cm silicon wafers with a 150 nm thermally grown oxide layer were used. Prior to film deposition they were cleaned in a heated ultra sonic bath in acetone for ten minutes, were rinsed with isopropanol and dried with CO_2 gas.

3.7.4 Drop Casting

Drop casting was performed by dropping 100 µL of C_8O-BTBT-OC_8/o-xylene solution of different concentrations onto the substrate. Evaporation of the solvent took place under the fume hood.

3.7.5 Spin Coating

To ensure that at least for one sample the phase transition from HB to bulk can be observed the same spin coating parameters as in [4] were used: coating 150 µL of C_8O-BTBT-OC_8/o-xylene solution at 2500 rpm for 45 s. However, different concentrations were used as well.

3.7.6 Solvent Vapour Annealing

SVA was done by placing up to three samples on upside-down petri dishes in a small dish and filling with 50 mL of o-xylene. The dish was closed by aluminium foil taped to the outside.

4 Results

In this chapter the results of the investigations of C_8O-BTBT-OC_8 obtained during this thesis are given, starting from polycrystalline powder measurements ranging to drop casted and spin coated films.

4.1 Polycrystalline Powder

Since C_8O-BTBT-OC_8 is a powder the easiest thing to measure is a spectrum of the plain substance as it is. It is very easy to collect Raman spectra of powder samples with the set-up described in section 3.4. To record IR spectra of the powder two different methods were used: ATR measurements and embedding the powder in potassium bromide (KBr) and measuring the resulting pellet in transmittance.

4.1.1 Raman Spectroscopy

Figure 4.1 shows the Raman spectrum of simple and grinded C_8O-BTBT-OC_8 powder. The as-is spectrum was collected with 50 x magnification and three cycles with 120 s each. The grinded powder spectrum was collected with a magnification of 20 for six cycles with 45 s each. On the x-axis the Raman shift in inverse centimetres is plotted. The y-axis shows the intensity of the Raman signal. The curves were normalised so that the highest peaks have the same height to make comparison easier. Otherwise the intensity differences would be too big due to the different measurement times.

On the far left, around $0\,\text{cm}^{-1}$, there is a huge peak due to Rayleigh scattering. According to Equations 2.2 and 2.23 a Raman shift of $0\,\text{cm}^{-1}$ means that the incoming and outgoing photons have the same energy, i.e. the photon scatters elastically. The peaks at higher wavenumbers are due to Stokes scattering (outgoing photon energy is lower than that of the incoming). In experiments usually only the Stokes region

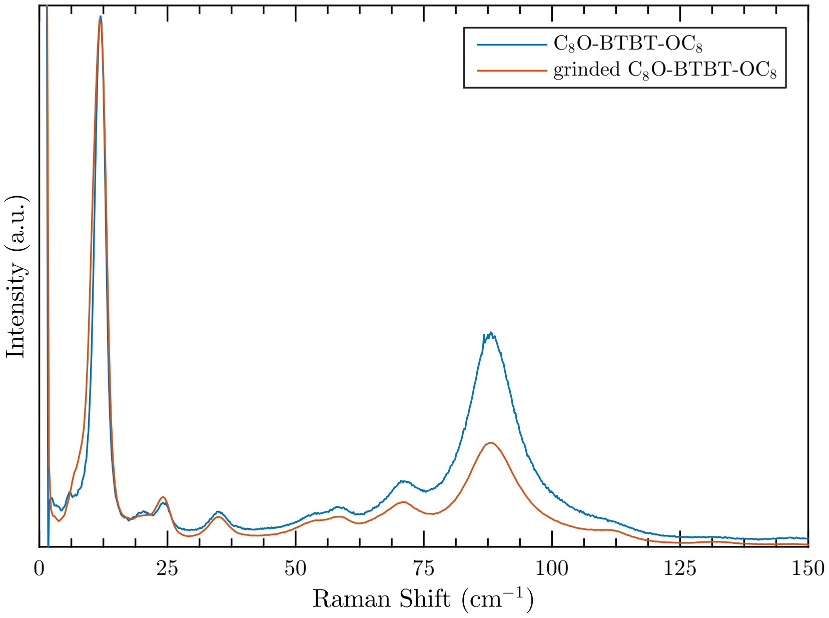

Figure 4.1: Raman spectra of untreated and grinded C_8O-BTBT-OC_8 in the region of the lattice phonons (also called intermolecular modes).

is measured because of the higher intensity there. The anti-Stokes region would be mirrored to the left of the Rayleigh peak with the same peak positions but lower intensity (see subsection 4.3.1 for a measurement of the anti-Stokes and Stokes region). At the wavenumber range from $5\,\mathrm{cm}^{-1}$ to $150\,\mathrm{cm}^{-1}$ lattice phonons are probed. These are highly influenced by intermolecular interactions which depend on the crystal structure. Therefore the phononic Raman spectrum can be seen as the fingerprint of a crystal structure [40]. However, at this stage it is not possible to relate the spectrum to one of the crystal structures of C_8O-BTBT-OC_8 because there is not enough information available yet.

According to Equation 2.22 the intensity of a Raman line depends on the polarisability of the molecule. Because of the anisotropy of the polarisability the sample orientation will influence the intensity. Furthermore in samples with a preferred orientation some modes may not be accessible because they cannot be excited due to geometric reasons. Therefore C_8O-BTBT-OC_8 powder was ground and measured as well. Grinding should give better statistics so that all possible crystal orientations are present in the sample. Comparing the two results shows that there are changes in the intensity of the Raman peaks due to polarisation effects. However, the overall shape of the measured spectra is the same (see Figure 4.1).

Figure 4.2 shows the Raman spectrum for higher Raman shifts (50 x magnification, three cycles à 60 s). Here the intramolecular modes are probed, so the result can be used to identify the chemical compound. The rising overall intensity with higher Raman shifts is due to increasing fluorescence effects. In the plot there are some spikes visible. These are measurement artefacts, most likely from stray light entering the set-up during measurement. Unfortunately these will occur in most of the following measurements as well. However, due to their shape they are easily distinguishable from real Raman peaks.

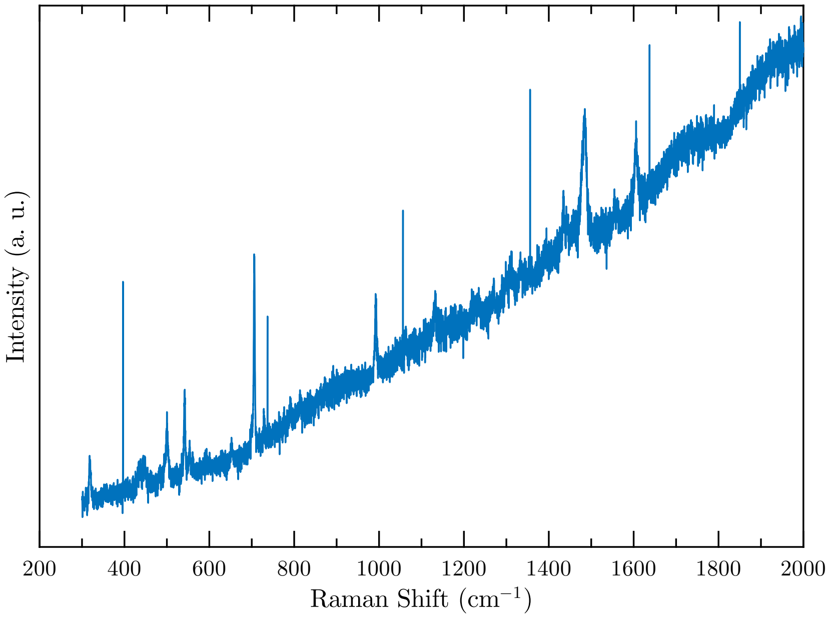

Figure 4.2: Intramolecular modes of the Raman spectrum of C_8O-BTBT-OC_8. The sharp spikes are artefacts due to stray light entering the set-up.

Because the main task was distinguishing different crystal structures, the focus was put on the intermolecular modes. Spectra of the intramolecular modes were recorded to ensure that differences appearing in the phonon spectra are due to changes in the crystal structure, not the chemical composition.

4.1.2 Attenuated Total Reflection Measurements

Figure 4.3 shows the ATR signal of the simple C_8O-BTBT-OC_8 powder. By comparing the resulting spectrum with tabulated literature values (e.g. [18, 29]) the peaks can be assigned to the corresponding vibrations as shown in the figure. Around $3000\,\mathrm{cm}^{-1}$ different C-H stretching vibrations can be found. Peaks at wavenumbers slightly above $3000\,\mathrm{cm}^{-1}$ originate from C-H vibrations of aromatic rings. Vibrations of C-H bonds in alkyl chains result in peaks slightly below $3000\,\mathrm{cm}^{-1}$. In the fingerprint region (Figure 4.3) nearly all peaks can be identified. Of course this is easier because the chemical composition of C_8O-BTBT-OC_8 is known. Identifying a completely unknown substance from an IR spectrum is very difficult.

The wavenumber range from $2500\,\mathrm{cm}^{-1}$ to $1800\,\mathrm{cm}^{-1}$ is not shown in Figure 4.3 because no peaks are visible there.

4.1.3 Potassium Bromide Pellet

A C_8O-BTBT-OC_8 KBr pellet was produced as described in subsection 3.7.1 and measured with the Bruker IFS 66v/S IR spectrometer (section 3.1) in transmission mode. Again, the peaks can be annotated with the different excited vibrations resulting in the higher absorption values. The result is shown in Figure 4.4.

Comparing this image with the ATR measurement (Figure 4.3) shows shifts for some of the vibrational peaks, e.g. the aromatic ring–oxygen stretch shifts from $1265\,\mathrm{cm}^{-1}$ in the transmission measurement to $1262\,\mathrm{cm}^{-1}$ in the ATR measurement. The largest difference can be found for the peak at $1214\,\mathrm{cm}^{-1}$ in the ATR measurement. In the transmission measurement of the pellet this peak can be found at $1218\,\mathrm{cm}^{-1}$. These shifts probably are the result of the pressure applied to the sample during the ATR measurement [33, 51].

Figure 4.5 shows the wavenumber region of the potassium bromide pellet which was left out in Figure 4.4. On the left hand side some of the C-H stretching peaks are visible. In the centre there is a large drop of the absorbance signal. This peak is not an IR absorption peak. One indication is that the peak direction is going down, whereas all the other peaks are going up. Furthermore the peak is much broader than the upwards pointing peaks. The described peak originates from multiple reflections at the parallel surfaces of the pellet. Due to interference effects absorbance at $2500\,\mathrm{cm}^{-1}$ is very low.

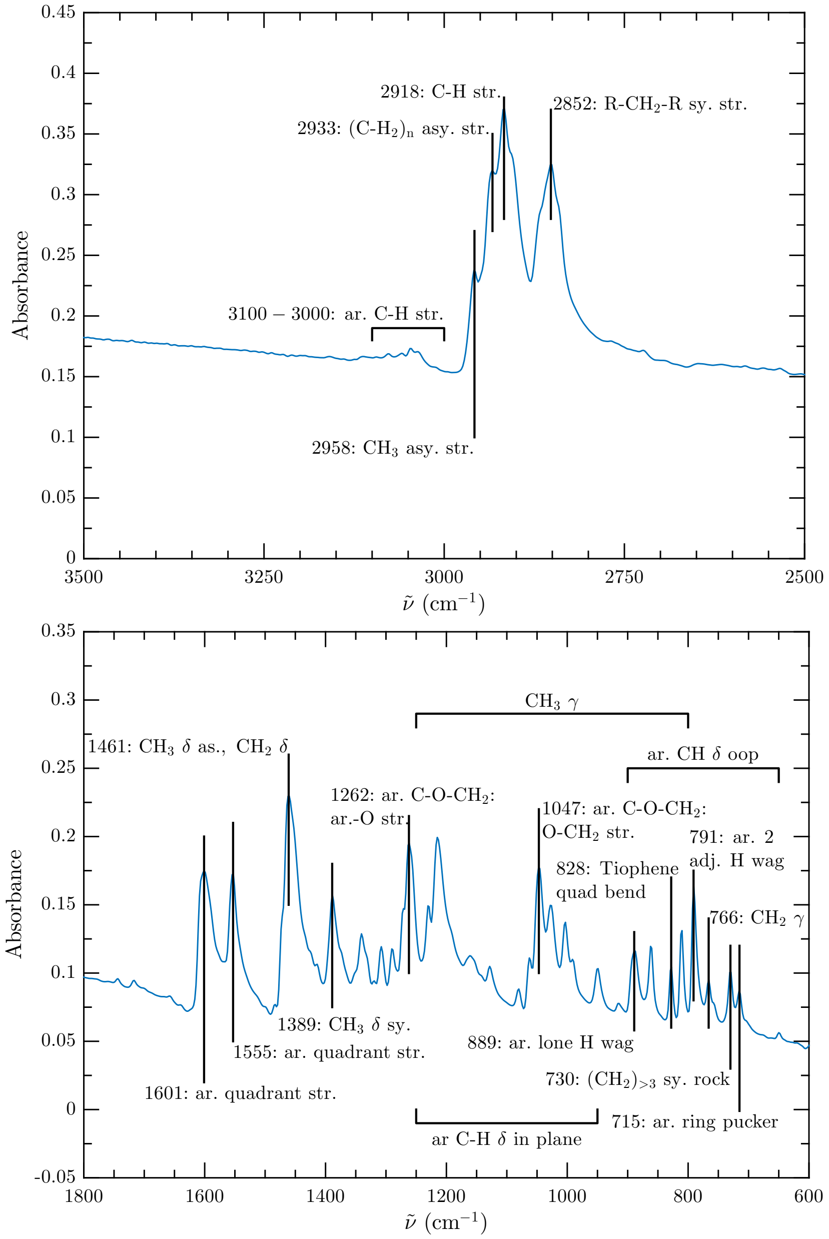

Figure 4.3: Attenuated total reflection spectrum of the plain C_8O-BTBT-OC_8 powder. Zoomed into the region of the C-H stretches (top) and the fingerprint region (bottom).[a]

---

[a] **Abbreviations used:** ar. aromatic; asy. asymmetric; δ deformation; γ vibration of the back bone; ip. in-plane; oop. out-of-plane; str. stretch; sy. symmetric.

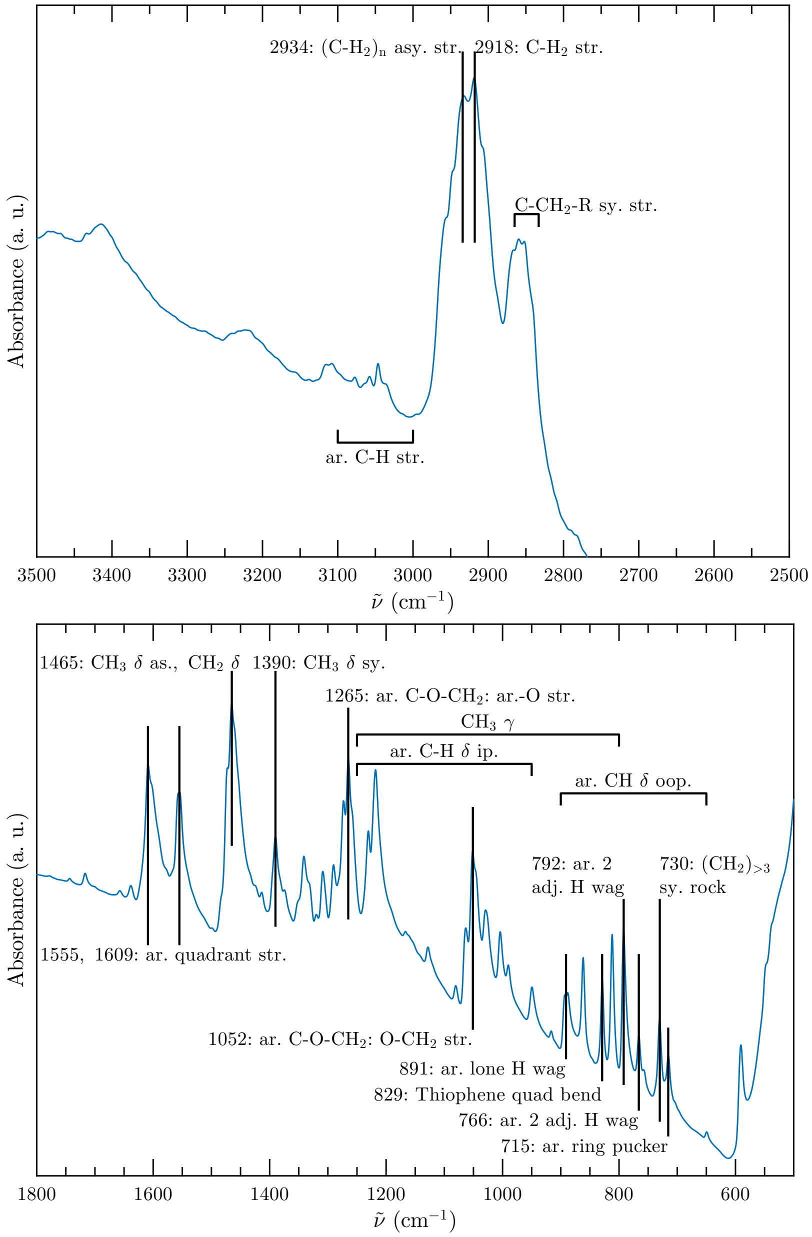

Figure 4.4: Infrared transmission spectrum of the C_8O-BTBT-OC_8 potassium bromide pellet. Zoomed into the region of the C-H stretches (top) and the fingerprint region (bottom).[a]

---

[a] **Abbreviations used:** ar. aromatic; asy. asymmetric; δ deformation; γ vibration of the back bone; ip. in-plane; oop. out-of-plane; str. stretch; sy. symmetric.

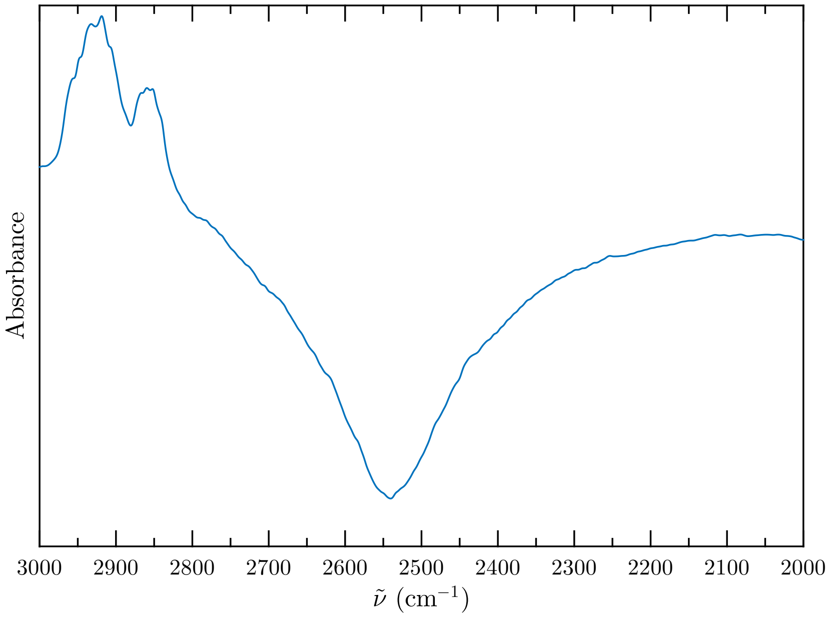

Figure 4.5: Infrared transmission spectrum of the KBr pellet showing an inverted peak due to multiple reflections at the parallel surfaces of the sample.

4.2 C_8O-BTBT-OC_8 in Solution

An IR transmission spectrum of a 10.8 g/L C_8O-BTBT-OC_8/o-xylene solution was measured with the Bomem MB-102 IR spectrometer (section 3.2). As background spectrum the signal of the pure solvent, measured in the same liquid cell, was used. The result is shown in Figure 4.6. Unfortunately, many of the bands are overlapped by bands of the solvent. However, some differences can be observed: In the o-xylene with C_8O-BTBT-OC_8 spectrum a peak at 1263 cm^{-1} is visible. This is due to the vibration of the oxygen attached to the benzene ring. Furthermore, additional peaks (e.g. 1213, 1064, 950 and 809 cm^{-1}) occur due to the CH_3 γ vibration of the long alkyl chain in C_8O-BTBT-OC_8. For most of the other peaks it cannot be decided whether their origin is the solvent or C_8O-BTBT-OC_8. Vertical lines are drawn in Figure 4.6 at the above mentioned wavenumbers to make the differences clearer.

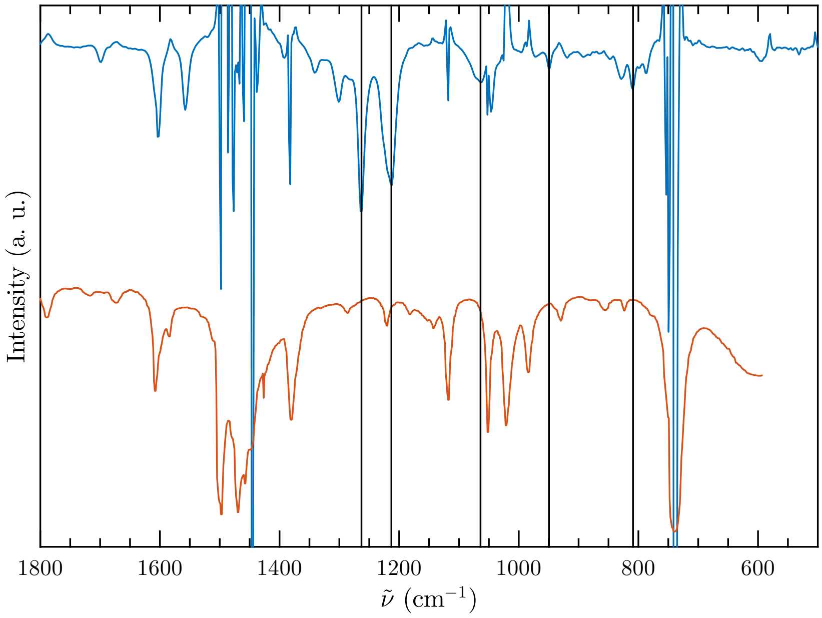

Figure 4.6: Fingerprint region of the infrared absorption spectrum of C_8O-BTBT-OC_8 in o-xylene (blue) compared to a literature spectrum of pure o-xylene (red) [52].

4.3 Crystals

As described in subsection 3.7.2 crystals from different solvents were grown. Figure 4.7 shows optical microscopy images of them. One can already see that there are basically three different types present:

1. crystals with very regular morphology and large extension from the uncovered chloroform and o-xylene solutions,
2. needle like shaped crystals from the uncovered hexane solution and
3. compact crystals from the covered hexane and uncovered acetone and methanol solutions.

The crystal grown from ethyl acetate solution in an uncovered vial is a mixture of cases two and three.

Two crystals from hexane solution were grown. After it turned out that the crystal from the uncovered vial, i.e. the one with higher evaporation rate, was in the herringbone structure (see subsections 4.3.1 and 4.4.3), other solvents were tested only uncovered. It

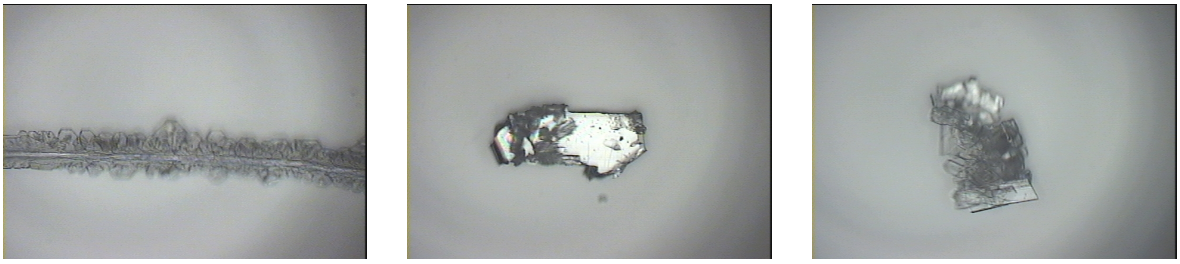

(a) from uncovered hexane solution

(b) from covered hexane solution

(c) from uncovered acetone solution

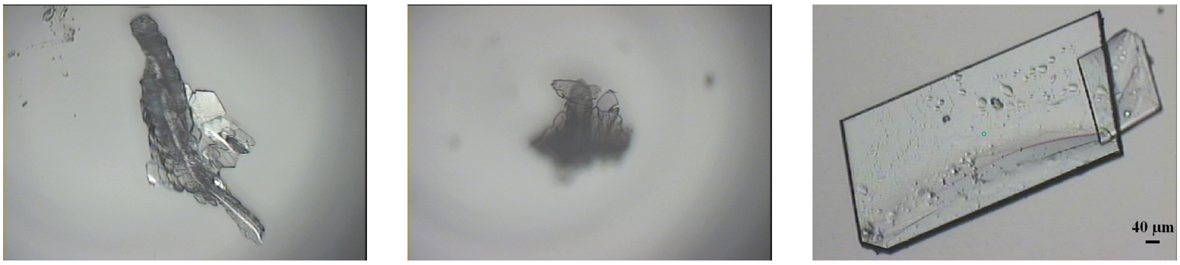

(d) from uncovered ethyl acetate solution

(e) from uncovered methanol solution

(f) from uncovered chloroform solution

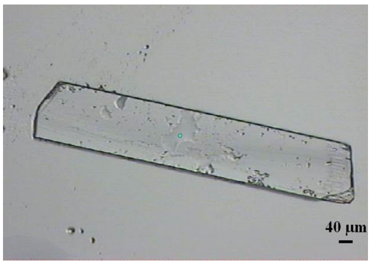

(g) from uncovered o-xylene solution

Figure 4.7: Optical microscopy images of C_8O-BTBT-OC_8 crystals grown from different solutions in covered or uncovered vials. Images (a) to (e) have the same scale as images (f) and (g). These images were recorded with the microscope attached to the Raman spectrometer (see section 3.4).

turned out that due to the higher evaporation speed the system does not have enough time to reach the thermodynamically most stable structure, the bulk form. Instead it goes to the kinetic phase of the herringbone. As will be shown in subsections 4.3.1 and 4.4.3, the crystals from hexane and ethyl acetate solution, both grown in uncovered vials, are the only ones in the herringbone phase. All others are, as well as the polycrystalline powder, in the bulk form.

Although evaporation of the chloroform solution was expected to be fast, it was very slow, explaining the very regular shape of the resulting crystal. This low rate could not be achieved again in experiments done in Graz. Here evaporation of C_8O-BTBT-OC_8/chloroform solution was much faster and led to irregularly shaped crystals. The reason could be that the experiment in Bologna was done under ambient conditions whereas in Graz it was performed under the fume hood. Since chloroform vapour is approximately four times heavier than air [53], vapour will be staying in the vial above the solution if no measures are taken to remove it. Under the fume hood the chloroform vapour is more likely to be removed, leading to faster evaporation.

4.3.1 Raman Spectroscopy

For the crystal from the uncovered hexane solution lattice phonon Raman spectra were measured once in the anti- as well as the Stokes region, both at the same position of the sample. The result is shown in Figure 4.8. Actually the picture shows two spectra, one for Raman shifts smaller, the other for shifts larger than zero. Although both spectra were recorded for three cycles à 60 s it seems that the anti-Stokes side has a higher intensity. This is because the spectrum in the anti-Stokes region was recorded without analyser in front of the spectrometer entrance slit, the Stokes region with a horizontal analyser. This of course reduces the measured intensity. The reason why the analyser was removed to record the anti-Stokes spectrum is simply that the already low intensity should not be decreased further with additional optics in the beam path. Nevertheless it can be seen that the anti- and Stokes peaks are symmetric around the intense Rayleigh peak. Asymmetries in the region close to $0\,\mathrm{cm}^{-1}$ are due to the filtering of the elastically scattered light.

As mentioned before, orientation of the sample will influence the obtained Raman spectrum. Furthermore, also the polarisation of the incoming light plays a role. Therefore

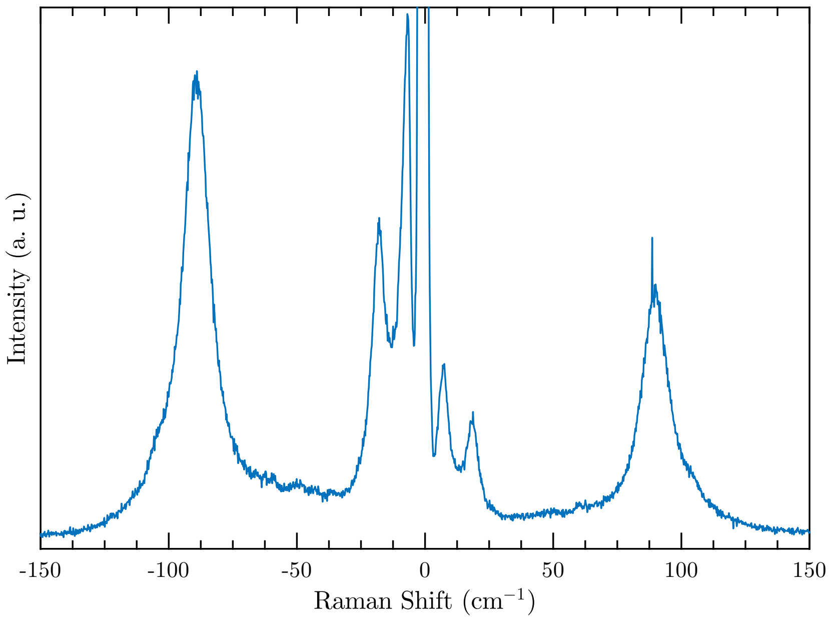

Figure 4.8: Raman spectra of the crystal grown in an uncovered vial from the hexane solution in the anti- and Stokes region.

Raman spectra of the crystals with various combinations of polariser and analyser direction as well as different sample orientation were measured.

Figure 4.9 shows Raman spectra of the crystal from the uncovered hexane solution compared to that of the plain C_8O-BTBT-OC_8 powder. For the measurement the crystal was placed on a stage which enabled rotating the sample. The spectra were recorded for 0°, 45° and 90° sample rotation. Comparing the powder and crystal spectra one can clearly see differences: The plain powder spectrum has two prominent peaks at $14\,\mathrm{cm}^{-1}$ and $87\,\mathrm{cm}^{-1}$, whereas the crystal spectra show peaks at $7\,\mathrm{cm}^{-1}$ and $19\,\mathrm{cm}^{-1}$ and in the higher wavenumber region two peaks at $89\,\mathrm{cm}^{-1}$ and $105\,\mathrm{cm}^{-1}$, independent of sample rotation.

Figure 4.10 shows Raman spectra of the crystal from the uncovered hexane solution recorded with a horizontal analyser and a horizontal or vertical polariser for different sample rotations. Independent of the polarisation of the incidence light and sample rotation the peaks always appear at the same wavenumber, only changes in the intensity are visible. The spectrum from the plain C_8O-BTBT-OC_8 powder cannot be observed with any of the polariser/sample orientation combinations.

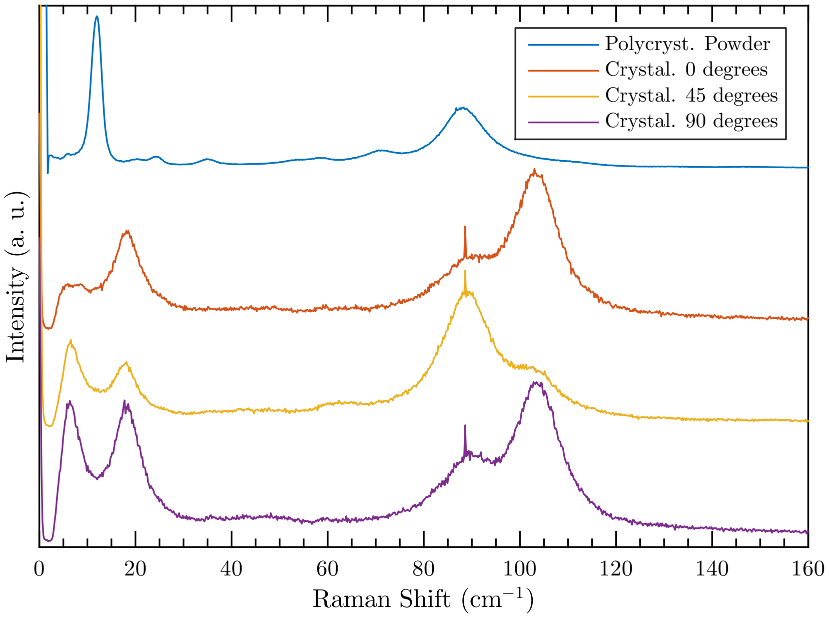

Figure 4.9: Raman spectra of the crystal grown in an uncovered vial from the hexane solution with 0 (=horizontal), 45 and 90° (=vertical) sample orientation compared to the plain C_8O-BTBT-OC_8 powder spectrum.

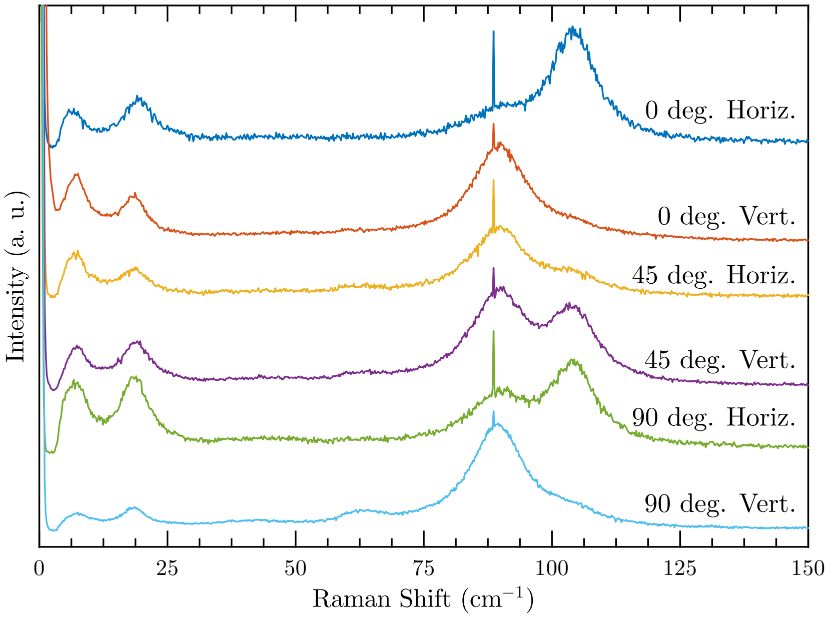

Figure 4.10: Raman spectra of the crystal grown in an uncovered vial from the hexane solution at different orientations (first part of the legend entry) and with different polarisation directions of the incoming laser beam (second part of the legend entry).

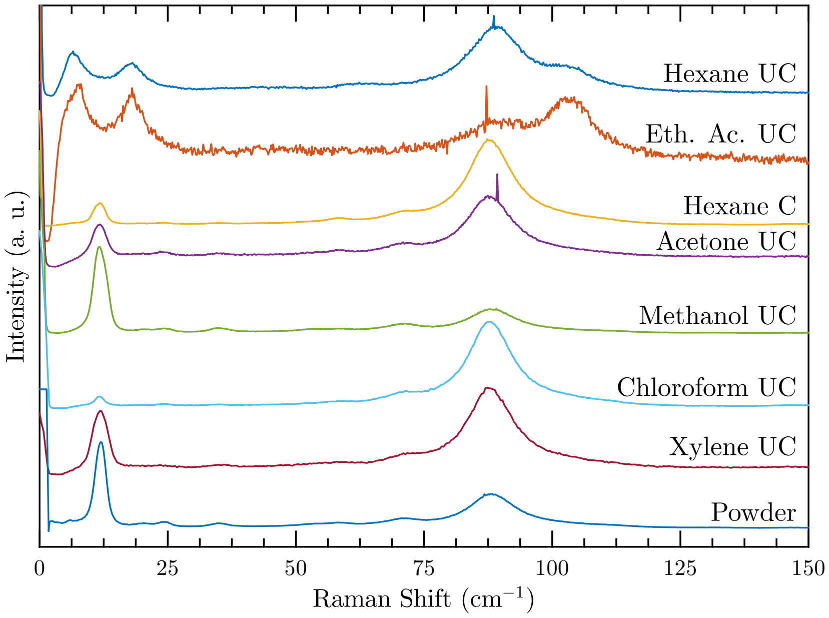

Figure 4.11: Overview of the Raman spectra of the crystals grown from different solvent in uncovered (UC) or covered vials (C). Eth. Ac. stands for ethyl acetate.

The measurements described above were repeated for all the crystals. They did not show different results than obtained for the crystal from the uncovered hexane solution or the plain powder. Either there are peaks at 14 cm^{-1} and 87 cm^{-1} or at 7 cm^{-1} and 19 cm^{-1} and in the higher wavenumber region two peaks at 89 cm^{-1} and 105 cm^{-1}. The polarisation only changes the intensity ratio between these peaks.

Figure 4.11 shows selected spectra of the crystals. What can be clearly seen is that all crystals except for the crystals grown from hexane and ethyl acetate solutions in an uncovered vial have the same spectra as the powder. Moreover, as the phononic parts of the spectra are shown, they also have the same crystal structures.

4.3.2 Attenuated Total Reflection Measurements

In a next step, ATR spectra of the crystal from hexane solution (covered) and from ethyl acetate solution (uncovered) as well as the simple C_8O-BTBT-OC_8 powder were recorded. Figure 4.12 shows different regions of them: The CH_3 asymmetric stretch (around 2956 cm^{-1}), the aromatic quadrant stretch (around 1600 cm^{-1}), the thiophene quad bend (around 830 cm^{-1}) and the aromatic C-H δ out-of-plane vibration (around

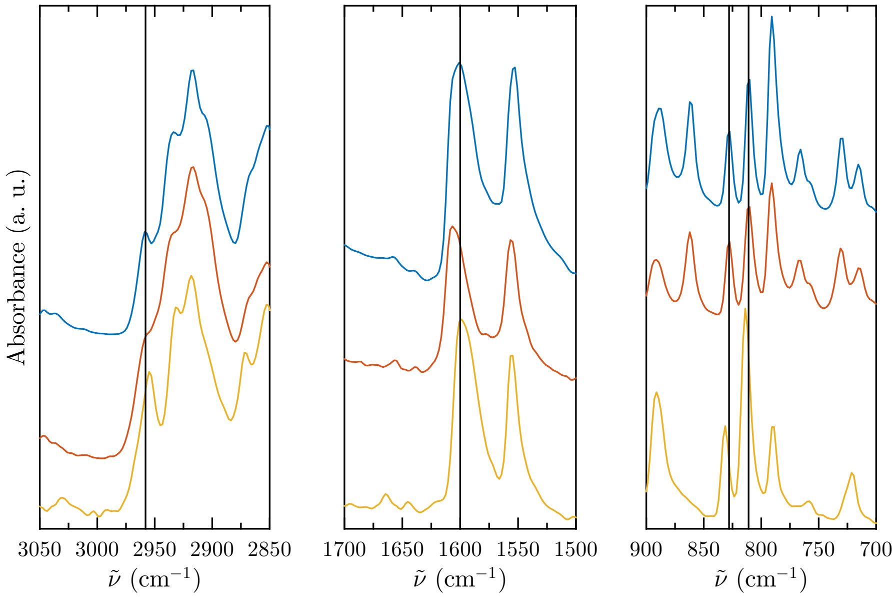

Figure 4.12: Attenuated total reflection spectra of the C_8O-BTBT-OC_8 powder (blue), the crystal from hexane solution (covered) (red) and from ethyl acetate solution (uncovered) (yellow) in the CH_3 asymmetric stretch (left), aromatic quadrant stretch (middle) and thiophene quad bend and aromatic C-H δ out-of-plane region (right). Vertical lines at 811, 828, 1600 and 2958 cm^{-1}.

815 cm^{-1}). In the measurements of the crystal grown from ethyl acetate solution in an uncovered vial a shift of the CH_3 asymmetric stretch to a lower wavenumber and a shift of the thiophene quad bend and an aromatic C-H δ out-of-plane peak to higher wavenumbers compared to powder and hexane crystal (covered) were found. In the spectrum of the crystal from hexane solution (covered) the aromatic quadrant stretch peak is shifted to higher wavenumbers compared to the powder and the ethyl acetate solution crystal (uncovered). Other peaks remain at their position. Therefore the error that the whole spectrum is shifted can be excluded. However, as mentioned before, peak shifts in ATR spectra can also occur due to the pressure applied onto the sample. Therefore one has to be careful when analysing peak positions here.

4.3.3 Overview

Table 4.1 gives a short overview of the results from Raman spectroscopy obtained for the powder and the different crystals.

Table 4.1: Most prominent Raman peaks of the plain C_8O-BTBT-OC_8 powder and crystals grown from different solutions and boiling points T_{boil} of the used solvents.

Sample	Raman Peaks (cm^{-1})	T_{boil} °C	Source
Powder	14, 87		
Crystal from			
• hexane solution, uncovered	7, 19, 89, 105	69	[54]
• ethyl acetate solution, uncovered	7, 19, 89, 105	77	[55]
• hexane solution, covered	14, 87	69	[54]
• acetone solution, uncovered	14, 87	56	[56]
• methanol solution, uncovered	14, 87	65	[57]
• chloroform solution, uncovered	14, 87	61	[53]
• xylene solution, uncovered	14, 87	144	[58]

The spectra obtained by ATR measurements show peak shifts in the CH_3 asymmetric stretch, aromatic quadrant stretch, thiophene quad bend and aromatic C-H δ out-of-plane region, whereas other peaks remain at their positions.

Looking only at the two crystals from hexane solution, grown in an uncovered and a covered vial, one reason for getting the herringbone structure in the one case and the bulk form in the other may be the evaporation speed. At higher evaporation speed the system has not enough time to go to the thermodynamically most stable form and appearance of the herringbone is preferred. However, the forming of the herringbone phase cannot be simply related to one property of the solvent such as the boiling point of the solvent (see Table 4.1). Other components playing a role are the relative vapour density (as explained for the crystal from chloroform solution above) and the vapour pressure. Also unintentional seeding as well as many other parameters play a role when growing crystals [59].

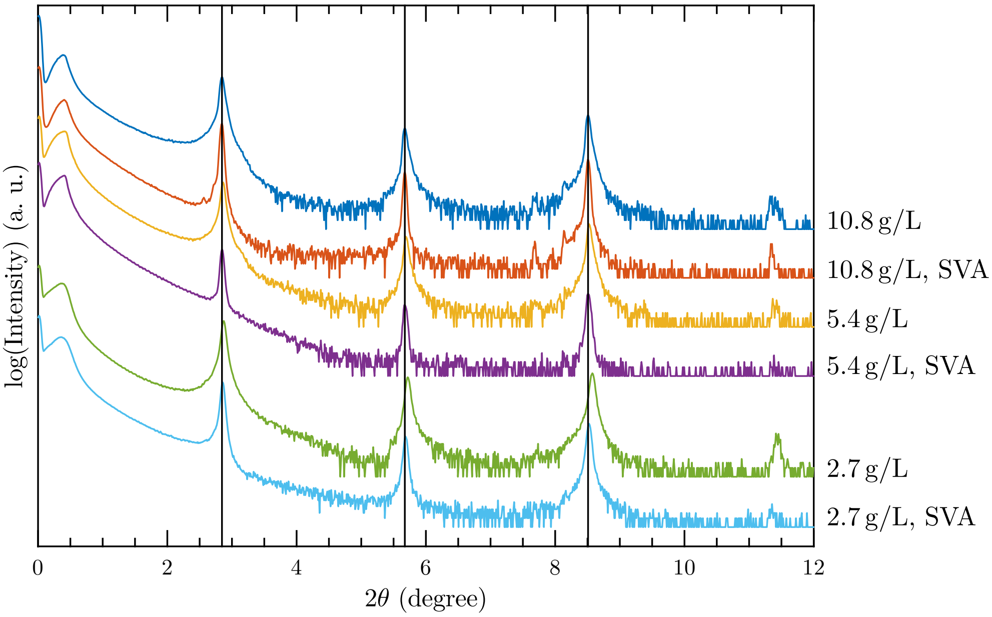

Figure 4.13: X-ray diffraction patterns of drop casted samples. Vertical lines at $2\theta = 2.8454$, 5.6740 and 8.5088° (corresponding to the (001), (002) and (003) peaks).

4.4 Drop Casted Films

To overcome the possibly pressure related peak shifts in ATR measurements, samples were drop casted from C_8O-BTBT-OC_8/o-xylene solutions as described in subsection 3.7.4. The following concentrations were used: 10.8, 5.4, 4.5, 3.6, 2.7 and 1.0 g/L. From every concentration two samples were casted, one was solvent vapour annealed for five days after preparation. This long annealing time was chosen to ensure that the structural phase transition is complete, the same approach as in [4].

4.4.1 X-Ray Reflectivity and X-Ray Diffraction

XRR and XRD patterns were recorded for the 10.8, 5.4, and 2.7 g/L samples. The results are shown in Figure 4.13. For the lowest concentration a slight shift of the (001), (002) and (003) peaks are visible. Furthermore the peaks of the annealed samples are sharper, indicating larger crystallites. With the software `Fityk` [60] the peak positions and peak widths were determined using a Pseudo-Voigt fit. From that the interplanar spacing (Equation 2.25) and the crystallite size perpendicular to the sample surface

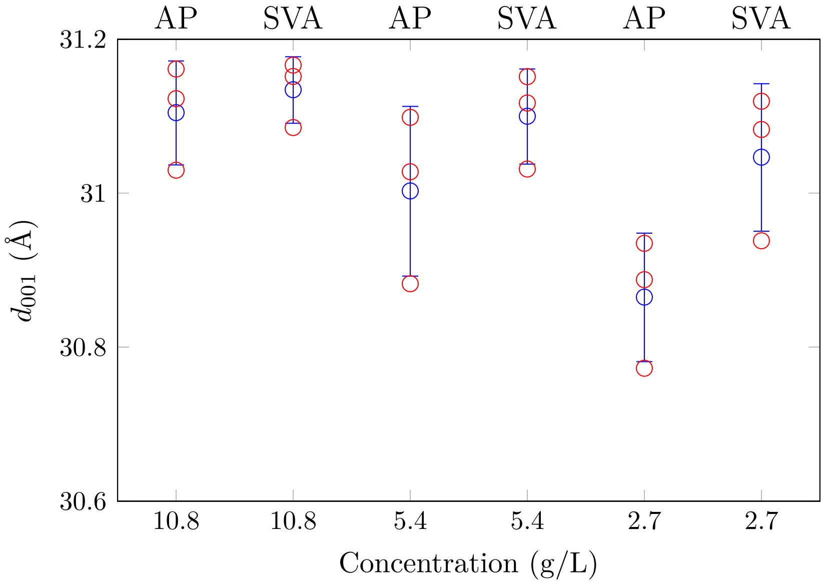

Figure 4.14: Interplanar distance d_{001} for drop casted samples of different concentrations. The upper x-axis shows whether the sample is as prepared (AP) or solvent vapour annealed (SVA).

(Equation 2.26) were calculated. These results are shown in Figures 4.14 and 4.15. The red circles represent the values calculated for the $(00l)$, $l = 1, 2, 3,$ peaks. In blue the average with the standard deviation is plotted. In [4] a lattice spacing of 30.85 Å for the as-prepared, and $d = 31.10$ Å for the annealed sample was found. Looking at Figure 4.14 one finds that only the 2.7 g/L as prepared sample has an averaged d value close to that of the as-prepared sample from [4]. All the other samples have averaged values larger than 31 Å. The crystallite size perpendicular to the sample surface is shown in Figure 4.15. It can be clearly seen that solvent vapour annealing increases the crystallite size, which can be confirmed by optical microscopy.

In the low 2θ range hardly any fringes are visible. The periodicity of the fringes slightly occurring in for example the annealed 5.4 g/L sample gives a thickness of approximately 150 nm, which is the thickness of the thermal oxide of the substrate. The drop of the signal after the critical angle indicates a very rough surface, which can also be confirmed by optical microscopy. As mentioned before, very rough surfaces won't lead to Kiessig fringes, making a thickness determination of the drop casted C_8O-BTBT-OC_8 film by XRR impossible.

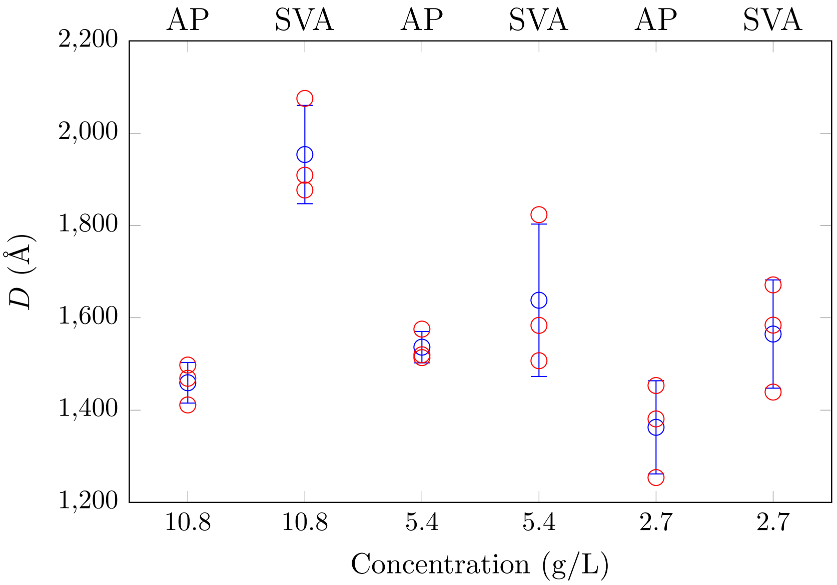

Figure 4.15: Crystallite size perpendicular to the sample surface D (bottom) for drop casted samples of different concentrations.

Williamson-Hall Analysis

A Williamson-Hall analysis was performed with the data obtained in the previous section. The resulting strain and size broadening is shown in Figure 4.16, the calculated L values are given in Table 4.2.

It can be clearly seen that the size broadening λ/L is higher for the as-prepared samples, i.e. $L = \lambda/(\Delta\,(2\theta)\cos\theta$ is larger for the solvent vapour annealed samples. This was already found in the previous section. However, the calculated values can only

Table 4.2: Crystal size perpendicular to the sample surface resulting from the Williamson-Hall analysis.

Sample	L (Å)
10.8 g/L	1435
10.8 g/L, SVA	1950
5.4 g/L	1600
5.4 g/L, SVA	2000
2.7 g/L	1595
2.7 g/L, SVA	1835

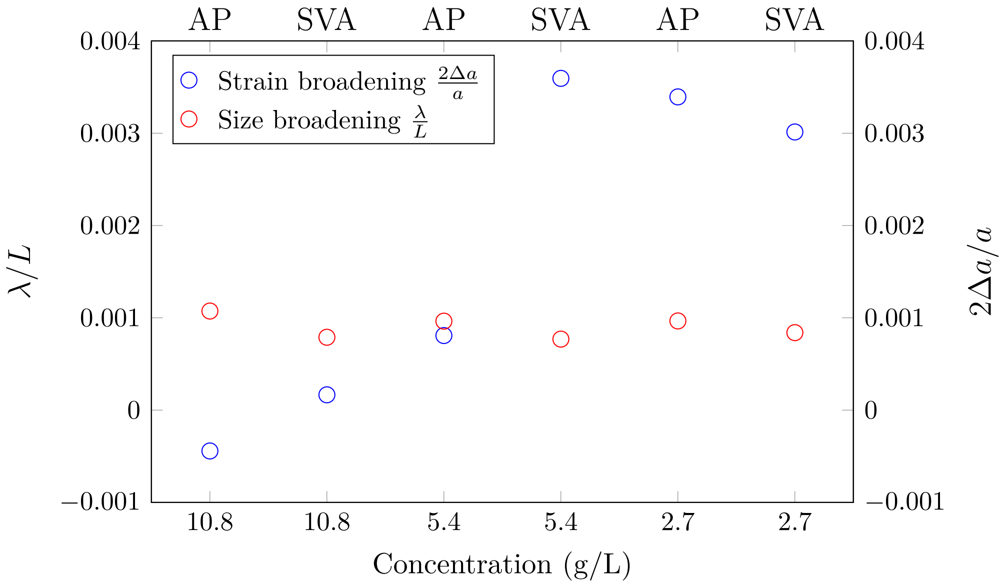

Figure 4.16: Results of the Williamson-Hall analysis for the drop casted samples.

show a trend. The absolute value cannot be used because the described lengths are already close to the coherence length of the X-ray source. Furthermore, instrumental broadening was not taken into account for the calculation.

In the case of the strain broadening the trend is not that clear. For the as-prepared 10.8 g/L sample the value is even smaller than zero. This is probably due to bad fitting. Literature gives strain values between 3×10^{-4} [61] and 14×10^{-3} [62] for organic films. The calculated values, except the one for the 10.8 g/L sample, are within this range.

4.4.2 Grazing Incidence X-Ray Diffraction

A set of 10.8, 5.4, 2.7 and 1.0 g/L drop casted samples were measured at BESSY, Berlin (section 3.6). In [4] it is described that the peaks are observed along rods. Therefore the resulting GIXD images were integrated to see the rod position clearer (Figure 4.17). However, due to experimental problems (e.g. positioning of the curved detector, bad statistics due to drop casted films) a big error is present in the data. The latter problem could be resolved by rotating the sample during the measurement. The mathematical correction of the changed detector position would be possible if a correction measurement was performed.

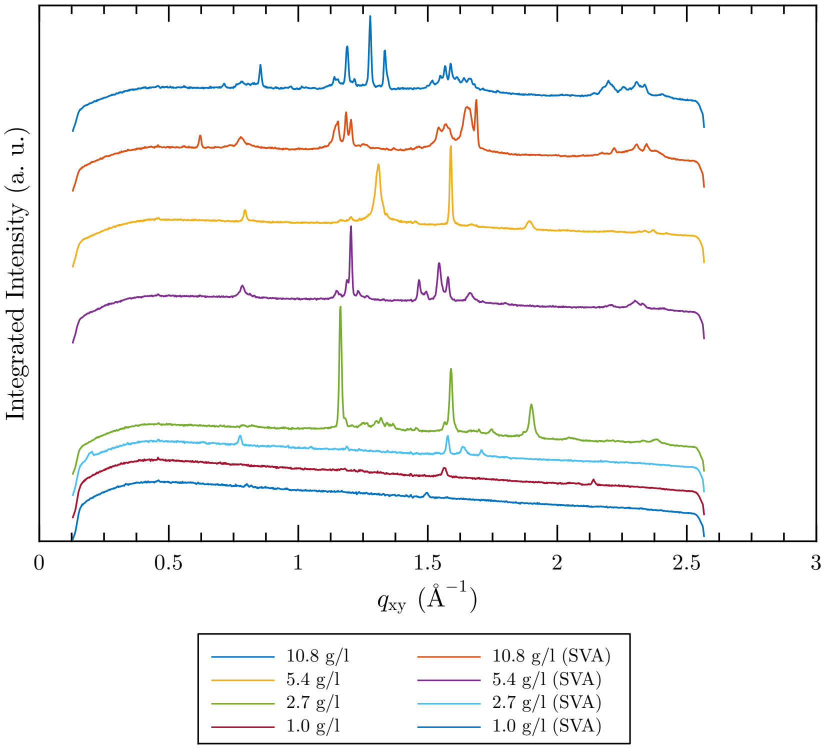

Figure 4.17: Integrated grazing incidence X-ray diffraction images, showing the positions of rods.

From the unit-cell parameters given in Table 1.1 the peak positions of the different C_8O-BTBT-OC_8 phases were calculated with the software `PyGid` [63]. The rod positions are given in Table 4.3. Clear indications for the herringbone structure are for example peaks at 1.3 and 1.9 Å^{-1}. The lower feature can be found in the three thickest as-prepared samples. The peak at the higher q_{xy} value can be found in the as-prepared films with a concentration of 5.4 and 2.7 g/L C_8O-BTBT-OC_8/o-xylene. However, in the thickest and third thickest as-prepared films also peaks around 1.2 Å^{-1} are visible, indicating the presence of the bulk form.

Although the GIXD images are heavily influenced by errors, it can be said that they are more sensitive for smaller quantities of one or the other phase. The Raman and IR spectroscopy measurements in the following sections show more a black and white image, either the one phase or the other is present, whereas GIXD reveals a phase mixing between both.

Table 4.3: Rod positions in films of C_8O-BTBT-OC_8 and the corresponding crystal structures [4].

Rod Positions q_{xy} ($\mathrm{Å}^{-1}$)	Structure
0.8	Both
1.0	Herringbone
1.2	Bulk
1.3	Herringbone
1.6	Both
1.9	Herringbone
2.1	Herringbone
2.2	Both
2.3	Bulk
2.4	Both

4.4.3 Raman Spectroscopy

Figure 4.18 shows the Raman spectra of some of the drop casted films, before and after SVA, compared to two spectra obtained for the crystals from covered hexane and uncovered ethyl acetate solution. Because of films on a substrate peaks due to the substrate are visible as well, e.g. the most prominent peak at $21\,\mathrm{cm}^{-1}$. This peak is used to align the spectra (subsection 3.4.1).

In the spectra of the 10.8 and 5.4 g/L samples, no matter if as prepared or annealed, there is a peak at $14\,\mathrm{cm}^{-1}$ and slightly below $90\,\mathrm{cm}^{-1}$, which correspond to the peaks of the crystal grown from hexane solution in a covered vial. The 2.7 g/L as prepared sample has no peak at $14\,\mathrm{cm}^{-1}$ but at $7\,\mathrm{cm}^{-1}$, corresponding to the peak position of the left most peak from the ethyl acetate solution crystal grown in an uncovered vial. In this crystal there is a second peak at $19\,\mathrm{cm}^{-1}$, which is not visible in the as prepared 2.7 g/L sample. In Raman spectrosocopy the incindence laser is perpendicular to the sample surface. So in the case of C_8O-BTBT-OC_8 it hits the (*ab*) crystal face of the monoclinic structure. Because of this orientation some lattice phonons cannot be excited, not because they are not symmetry allowed, but because they are geometrically not accessible. In a crystal, although there is a preferred orientation, the possibility is higher that all crystal faces can be accessed, especially when the crystals are very irregular as the ones investigated (compare Figure 4.7).

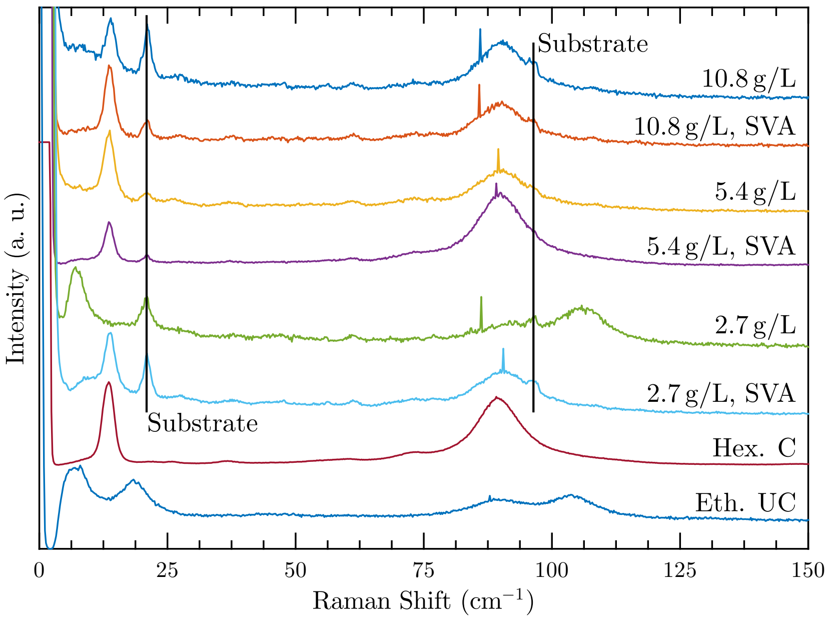

Figure 4.18: Raman spectra of drop casted samples compared to the spectra of the crystal from covered hexane (Hex. C) and uncovered ethyl acetate solution (Eth. UC).

The solvent-vapour-annealed 2.7 g/L sample has the same peak positions as the four thickest ones.

From literature it is known that SVA turns the herringbone into the bulk structure [4]. Therefore the spectrum of the crystal from uncovered hexane solution can be related to the herringbone, the spectrum of the crystal grown in the covered vial to the bulk structure. Comparing this result to the other samples it can be said that all the films with a concentration higher than 2.7 g/L are in the bulk structure. Most likely these films are so thick that only bulk form is present, not the phase of the herringbone. The only sample where the expected structural change due to SVA can be observed is the 2.7 g/L film.

4.4.4 Infrared Reflection Measurements

Figure 4.19 shows IR reflection spectra of the drop casted films with the same regions enlarged as in the ATR measurements of the crystals.

Looking at the 1.0 g/L sample there are clear differences in the spectra: In the CH_3 asymmetric stretch region the as-prepared film has one peak (2950 cm^{-1}), whereas the

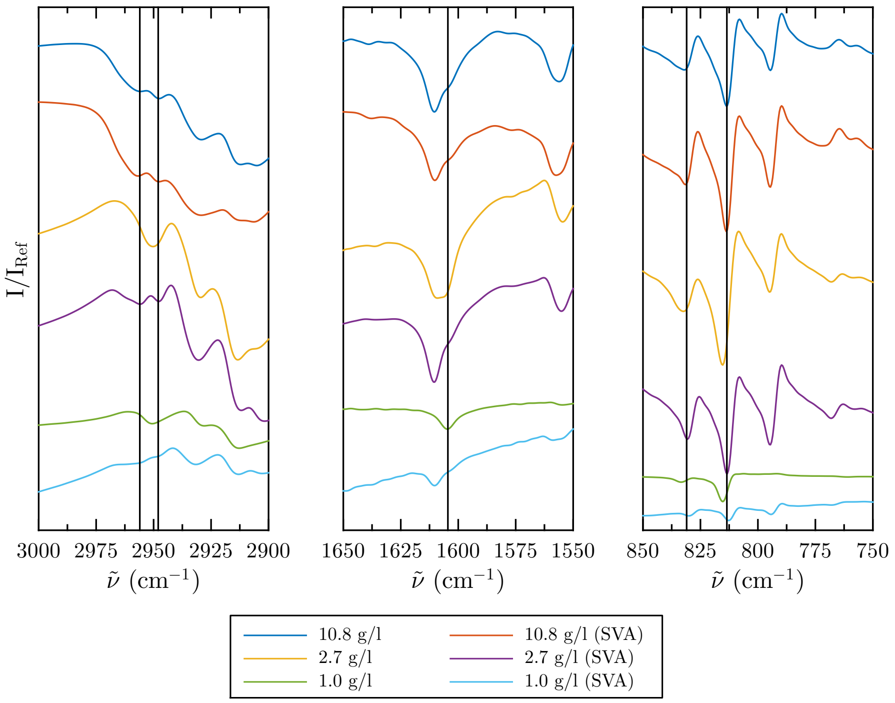

Figure 4.19: Infrared reflection spectra of some drop casted samples in the CH_3 asymmetric stretch (left), aromatic quadrant stretch (middle) and thiophene quad bend and aromatic C-H δ out-of-plane region (right). Vertical lines at 814, 831, 1605, 2948 and 2956 cm^{-1}.

annealed film has two (2948 and 2956 cm^{-1}). In the region around 1600 wavenumbers there is a shift of the aromatic quadrant stretch peak from 1605 cm^{-1} in the as-prepared film to 1610 cm^{-1} in the annealed sample. Also in the lower wavenumber region differences in peak position occur. The thiophene quad bend peak shifts from 833 to 829 cm^{-1}, the aromatic C-H δ out-of-plane peak from 815 to 813 cm^{-1}. From literature it is known that the annealed films are in the bulk form, therefore the annealed 1.0 g/L sample spectrum can be identified with the bulk structure, the as prepared sample spectrum with the herringbone.

Comparing the other spectra with respect to the differences explained above confirms the results from the lattice phonon Raman spectra. An interesting feature is the broad double peak of the 2.7 g/L sample in the aromatic quadrant stretch region, indicating a mixture between bulk and herringbone structure. This cannot be confirmed, neither with Raman spectroscopy nor any of the other regions of the IR spectrum. The same can be seen in the 4.5 g/L sample (not shown in Figure 4.19).

4.4.5 Infrared Transmission Measurements

The results from IR transmission measurements are shown in Figure 4.20. In the left most image no differences in peak number for the two thick films as in the reflection measurements (Figure 4.19) are visible. Only for the 1.0 g/L sample there might be two peaks for the annealed sample and one for the as prepared, although the peak intensity is already quite low. In the middle image no peak shifts occur in the two thick films. In the 1.0 g/L sample there might be a peak position difference. However, intensity is not good here neither. The intensity is sufficient in the right plot. For the thin sample a clear peak shift is visible in both the thiophene quad bend and the aromatic C-H δ out-of-plane peaks. The thick films are more or less unchanged again, confirming the results from the measurements in reflection in this region.

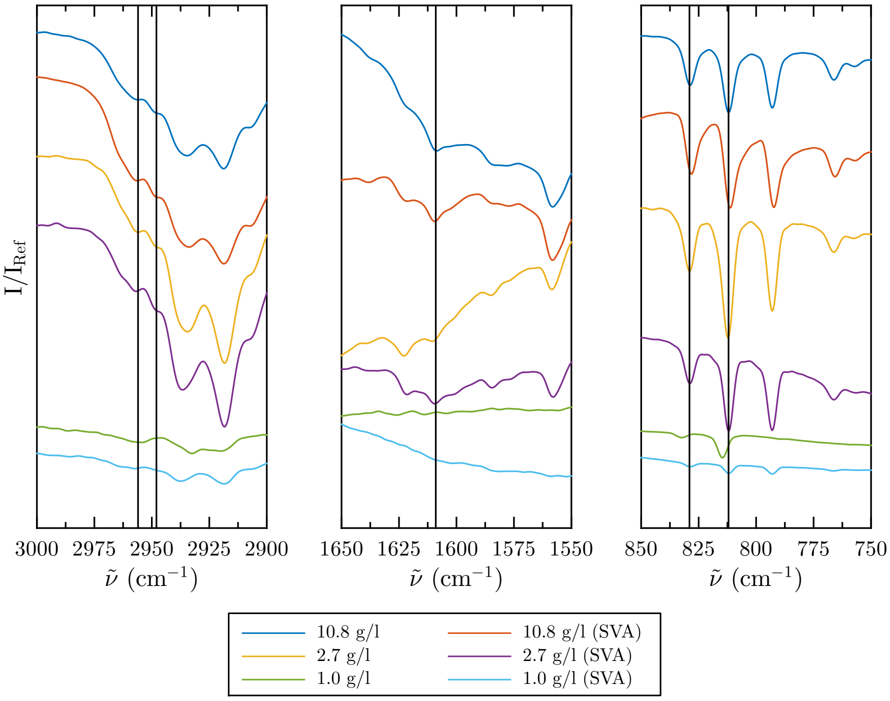

Figure 4.20: Infrared transmission spectra of some drop casted samples in the CH_3 asymmetric stretch (left), aromatic quadrant stretch (middle) and thiophene quad bend and aromatic C-H δ out-of-plane region (right). Vertical lines at 812, 829, 1609, 2948 and 2956 cm^{-1}.

4.4.6 Overview

Figure 4.21 shows an overview of the obtained results from the different measurement methods for the drop casted samples. On the bottom axis the different concentrations are plotted. The upper horizontal axis shows whether the sample is as prepared (AP) or solvent vapour annealed (SVA). On the left the possible crystal structures are given: herringbone (HB), bulk or a mixture between both. Every symbol represents a certain experimental technique or in the case of IR spectroscopy a certain wavenumber region where differences occurred in the spectra. If a symbol is not present in a column at all, it means that this technique was not used on this sample, e.g. no Raman spectra were recorded for the 4.5, 3.6 and 1.0 g/L samples. The plus sign + shows the expectation: As prepared films are in the herringbone structure and turned into bulk form by solvent vapour annealing [4]. However, this can only be confirmed for samples drop casted from solutions with concentrations less than 5.4 g/L C_8O-BTBT-OC_8/o-xylene.

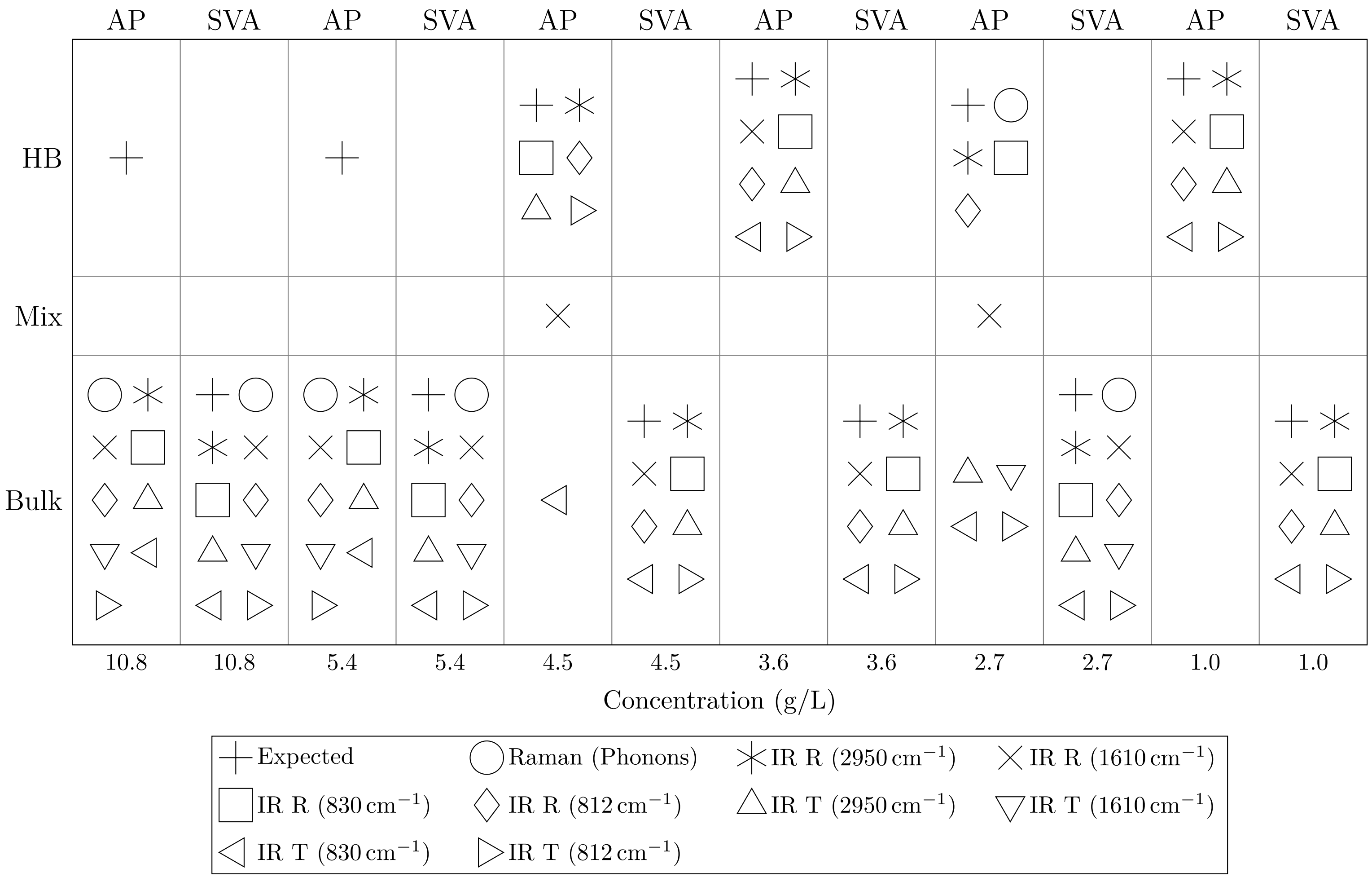

Figure 4.21: Overview of the results for the drop casted samples. IR R stands for IR spectroscopy in reflection, IR T for IR spectroscopy in transmission.

4.5 Spin Coated Films

The following concentrations were used to prepare spin coated samples as described in subsection 3.7.5: 10.8, 5.4, 2.7 and 1.0 g C_8O-BTBT-OC_8 per litre o-xylene.

4.5.1 X-Ray Reflectivity and X-Ray Diffraction

XRR and XRD measurements were performed on the 10.8, 5.4 and 2.7 g/L C_8O-BTBT-OC_8/o-xylene samples. The result is shown in Figure 4.22.

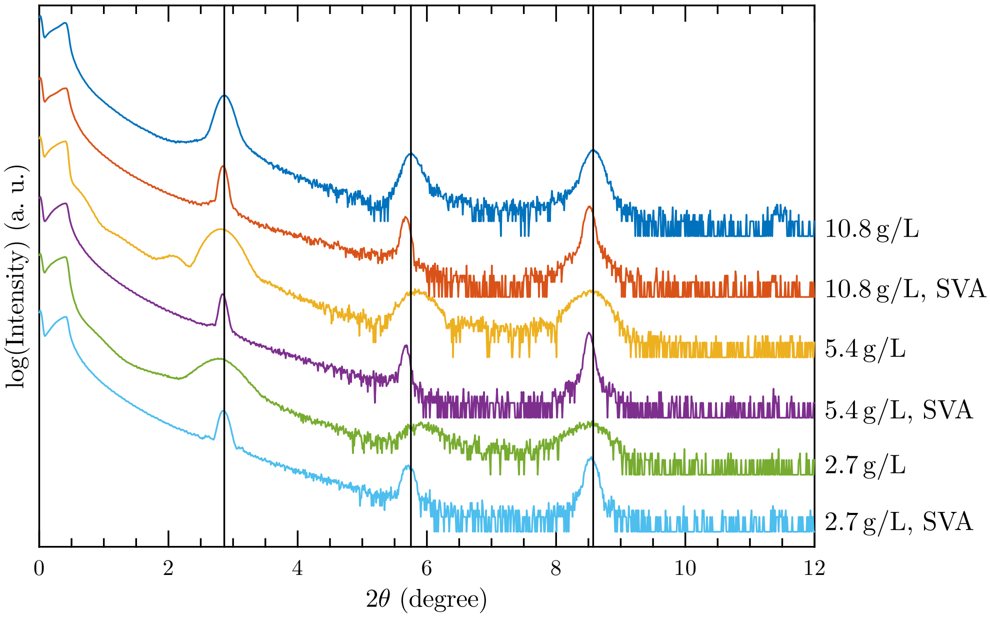

Figure 4.22: X-ray diffraction patterns of drop casted samples. Vertical lines at $2\theta = 2.8640$, 5.7528 and 8.5737° (corresponding to the (001), (002) and (003) peaks).

As before it can be observed that SVA makes the peaks in the XRD pattern sharper, indicating bigger crystallites. Furthermore peak shifts occur, a sign for changes in the interplanar distance.

Again, as for the drop casted films, the lattice spacing d and the crystallite size perpendicular to the surface D were calculated (Figure 4.23). For the thin as-prepared films peak position and width determination was difficult due to the low signal, resulting in higher errors. From Figure 4.23 it can be seen that the two thickest as-prepared samples have averaged d values slightly below 31 Å. In [4] an interplanar distance of

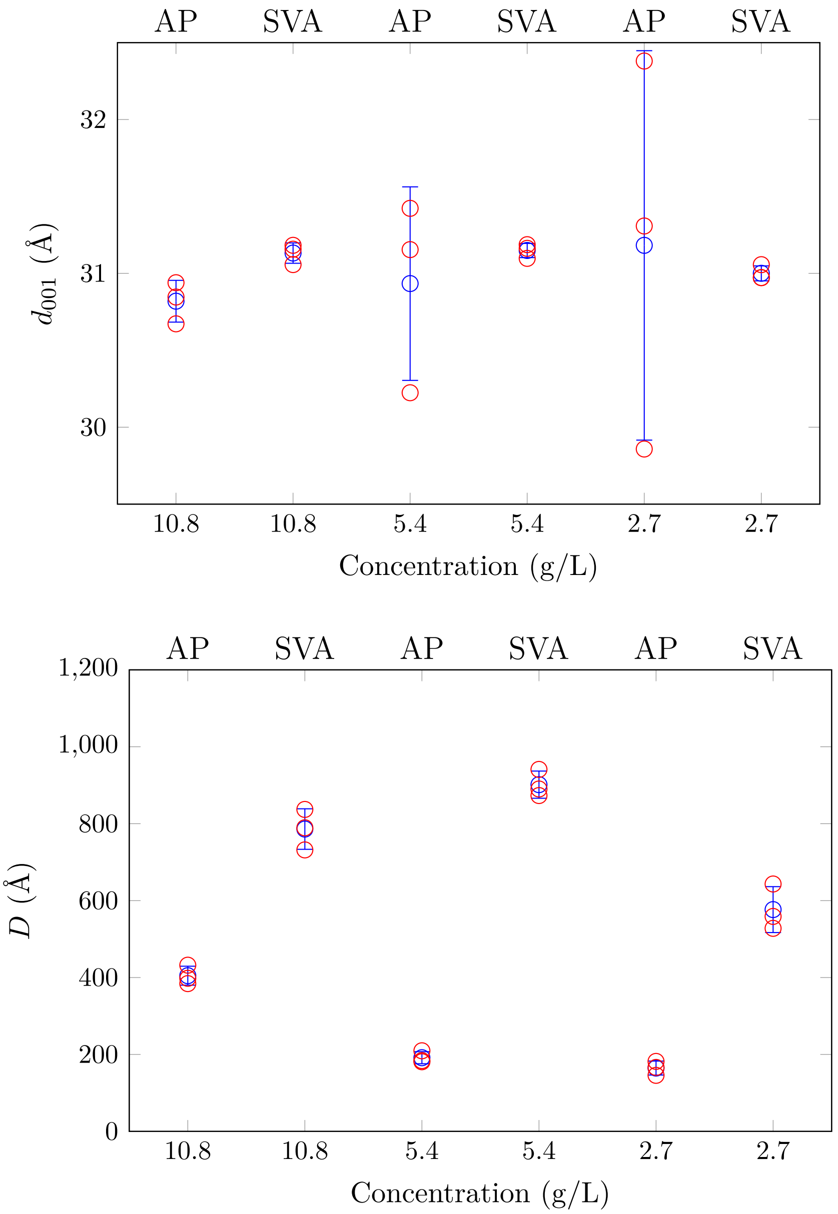

Figure 4.23: Interplanar distance d_{001} (top) and crystallite size perpendicular to the surface D (bottom) for spin coated samples of different concentrations. The upper x-axis shows whether is as prepared (AP) or solvent vapour annealed (SVA).

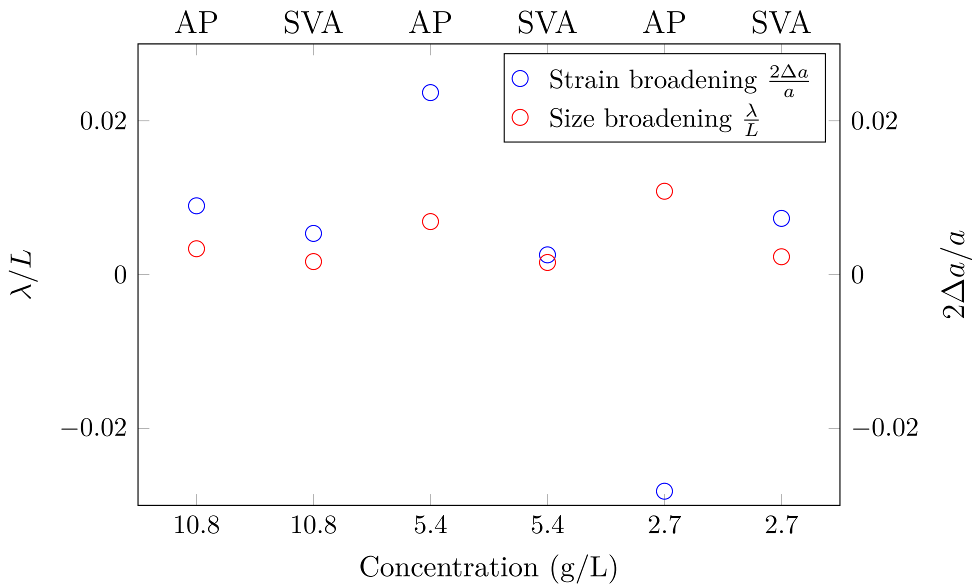

Figure 4.24: Results of the Williamson-Hall analysis for the spin coated samples.

30.85 Å was found for the as-prepared films, which is similar to the above result. The solvent-vapour-annealed films have larger averaged d values (slightly above 31 Å). Again, this matches the results from [4]. However, the errors are quite large due to a worse signal because of the thinner films, especially for the 2.7 g/L sample.

In Figure 4.22 some fringes are visible in the low 2θ range. These, again, correspond to the thickness of the thermal oxide of the wafer (150 nm).

Williamson-Hall Analysis

With the data obtained in the previous section a Williamson-Hall plot was created (Figure 4.24). From that the L values can be calculated (Table 4.4). Again, it can be found that the size broadening λ/L is larger for the as-prepared films, indicating bigger crystallite size L for the annealed samples. Also here one sample has a strain broadening smaller than zero, which is due to the low signal and therefore difficult parameter extraction. One of the strain broadening values is lying over the highest reported literature value [62] of $14 \cdot 10^{-3}$, what could also be due to the difficulties related to parameter determination.

Table 4.4: Crystal size perpendicular to the sample surface resulting from the Williamson-Hall analysis.

Sample	L (Å)
10.8 g/L	455
10.8 g/L, SVA	905
5.4 g/L	225
5.4 g/L, SVA	970
2.7 g/L	140
2.7 g/L, SVA	660

4.5.2 Raman Spectroscopy

In Figure 4.25 Raman spectra of the thickest spin coated sample before and after SVA compared to the spectrum of a clean substrate are plotted. What can be seen is that basically all peaks are due to the substrate. Even increasing the measurement time did not give better results. Due to the low thickness of the film – stylus profilometry showed a film thickness of (50 ± 15) nm – it is not possible to collect a Raman spectrum within

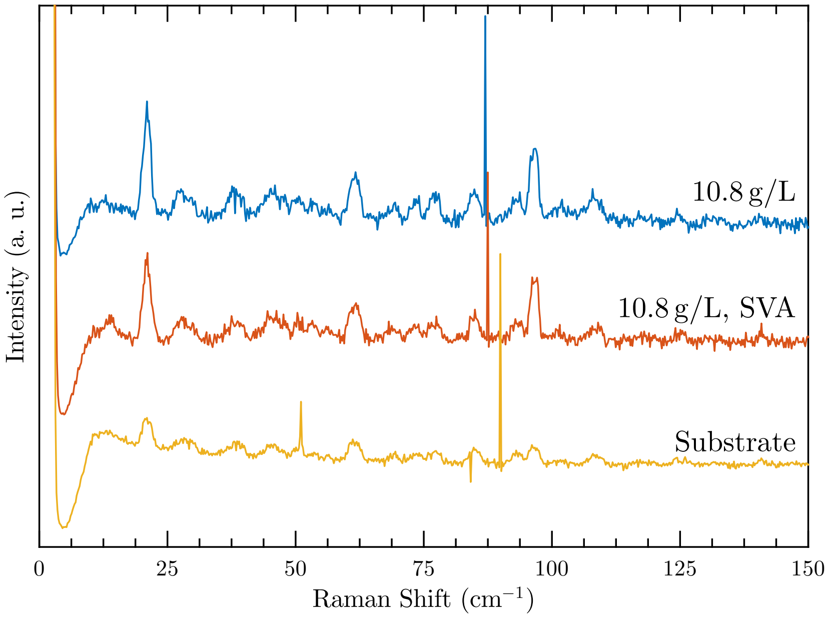

Figure 4.25: Raman spectra of the two thickest spin coated samples compared to the spectrum of a clean substrate.

a reasonable measurement time. The measurement time has to be limited, otherwise the focussed laser beam may damage the sample.

4.5.3 Infrared Reflection Measurements

Figure 4.26 shows IR reflection spectra of some of the spin coated samples. Especially for the lowest concentration sample one can see that it is already quite difficult to evaluate the spectrum with respect to the differences described in subsection 4.4.4. Furthermore for the 1.0 g/L sample in the region around 1600 cm^{-1} peaks due to water vapour appear, making interpretation even more difficult. However, for the thicker samples evaluation is still possible. For all of the samples except for the 2.7 g/L sample the expected behaviour can be seen. In the case of the 2.7 g/L sample, both, the as-prepared and annealed samples are in the herringbone structure. Due to the fact that also the 2.7 g/L drop casted sample showed an unexpected behaviour the problem may be lying in the solution used.

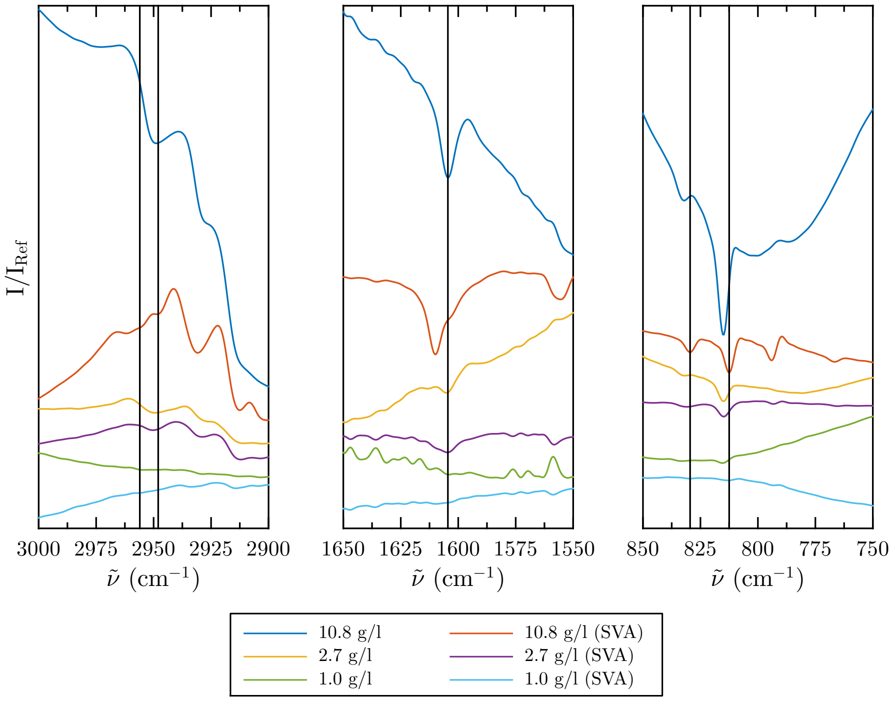

Figure 4.26: Infrared reflection spectra of some of the spin coated samples. Vertical lines at 812.5, 829.5, 1604.5, 2948 and 2956 cm^{-1}.

4.5.4 Infrared Transmission Measurements

Figure 4.27 shows the IR transmission spectra of the spin coated samples. Especially differences of the thiophene quad bend and aromatic C-H δ out-of-plane peaks are visible. These peaks are shifted to higher wavenumbers in the as-prepared 10.8 and 5.4 g/L samples, indicating the herringbone structure. For the 2.7 g/L sample the same conclusions as from the reflection measurements can be drawn: Both, the as-prepared and the annealed samples are in the herringbone. For the 1.0 g/L sample it is quite difficult to decide. It seems that the peak positions correspond to that of the herringbone structure, no matter if annealed or as prepared.

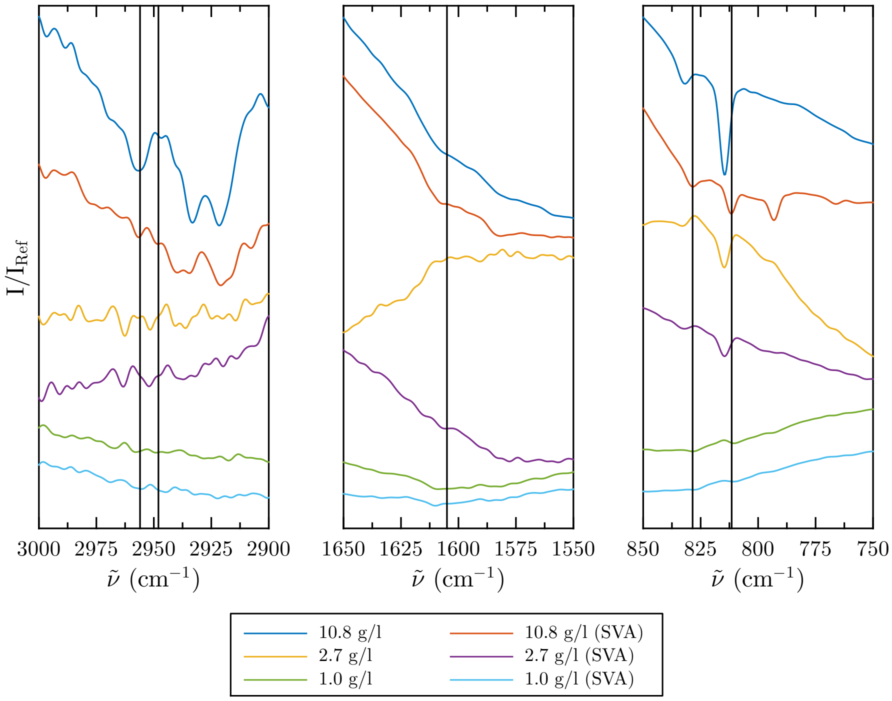

Figure 4.27: Infrared transmission spectra of some of the spin coated samples. Vertical lines at 811.5, 828.5, 1605, 2948 and 2956 cm^{-1}.

4.5.5 Overview

Figure 4.28 shows an overview of the results for the spin coated samples. For the two thickest samples the expected result can be observed: as-prepared samples are in the herringbone structure, whereas solvent vapour annealed samples are in the bulk form

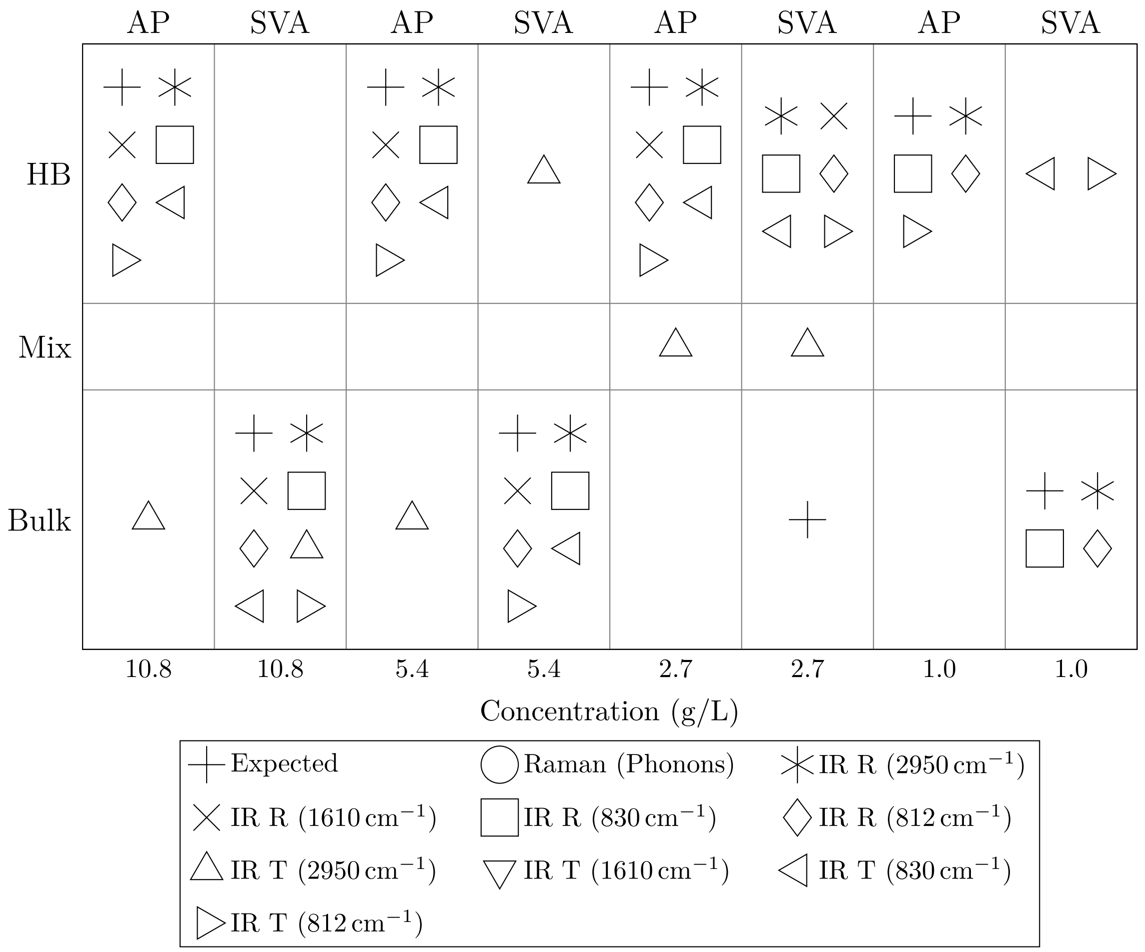

Figure 4.28: Overview of the results for the spin coated samples. IR R stands for IR spectroscopy in reflection, IR T for IR spectroscopy in transmission.

(+ symbol). The 2.7 g/L sample shows the characteristics of the herringbone structure, no matter if as prepared or annealed. Maybe there was a problem during the annealing process, or, since the drop casted 2.7 g/L sample showed an unexpected behaviour as well, an issue with the solution. For the 1.0 g/L sample it is already very difficult to decide from the IR spectra which phase is present. Therefore many of the symbols are missing in the two corresponding columns.

4.6 Heating

Four samples were drop casted as described in subsection 3.7.4 with the 2.7 g/L C_8O-BTBT-OC_8/o-xylene solution. One was used as reference, the other three were heated as described below.

Simple heating experiments were done to investigate the presence of phase transitions. Figure 4.29 shows the heating experiment up to 99 °C. Below 90 °C one peak at $2\theta = 2.8°$ is present. At the next heating step (95 °C) a second peak arises at 3.3°, which stays also for higher temperatures whereas the peak at the lower 2θ angle vanishes completely at 99 °C. During cool down the second peak shifts from 3.3° to 3.4°. Furthermore the first peak shows up again (2.8°). However, after four days under ambient conditions only one peak remains at $2\theta = 2.9°$.

Heating over 99 °C shows that the peak at 3.3° is stable up to 162 °C. At 172 °C a peak at 3.0° appears. At 182 °C no peaks are visible anymore, indicating the melt of the film. During cool down a peak at 3.45° reappears. However, after four days this peak is gone and a peak at 2.9° is present.

From these measurements it can be found that phase transitions take place at 99 °C, 172 °C and 182 °C. So three new samples were heated to these temperatures, cooled down again and measured with IR spectroscopy afterwards.

4.6.1 Heating Process

During the heating process XRR/XRD was performed to observe the occurring phase transitions. Table 4.5 shows an overview of the peak positions.

Table 4.5: Overview of the peak positions obtained during X-ray diffraction measurements at different temperatures of the samples heated to 99, 172 and 182°.

Heating	Before	at 99 °C	at 172 °C	at 182 °C	After cool down
to 99 °C	2.845°	3.319°			2.882°, 3.478°
to 172 °C	2.845°	3.341°	3.057°		2.867°, 3.183°, 3.533°
to 182 °C		3.317°	3.039°	–	2.882°, 3.209°, 3.554°

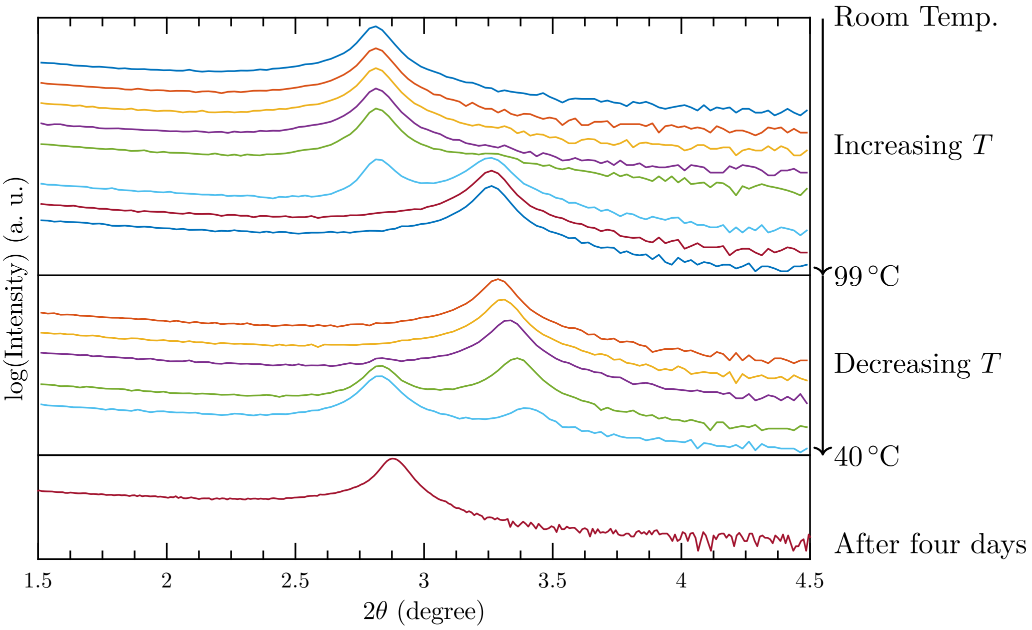

Figure 4.29: Heating to 99 °C and cooling down again. Spectra were recorded at the following temperatures: 75, 80, 85, 90, 95, 97, 99, 80, 70, 60, 50 and 40 °C.

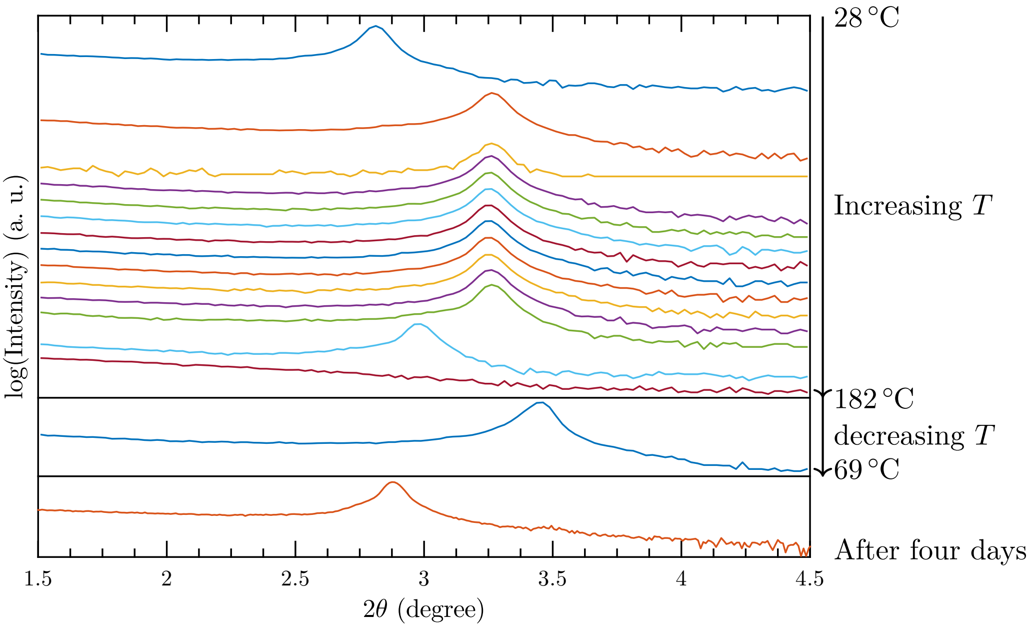

Figure 4.30: Heating to 182 °C and cooling down again. Patterns shown were collected at temperatures of 28, 97, 102, 107, 112, 117, 122, 127, 132, 142, 152, 162, 172, 182 and 69 °C.

4.6.2 Infrared Spectroscopy

The heat treated samples were measured by IR spectroscopy in reflection and transmission and analysed for the differences obtained in the previous sections. Table 4.6 shows the results summed up.

Table 4.6: Overview of the results obtained from infrared spectroscopy in reflection (IR R) and transmission (IR T) at different wavenumbers of the heated samples.

Sample	IR R (2950)	IR R (1610)	IR R (830)	IR T (830)	IR T (812)
Control	Bulk	Bulk	Bulk	Bulk	Bulk
To 99 °C	HB	HB	HB	HB	HB
To 172 °C	HB	HB	HB	Bulk	Bulk
To 182 °C	HB	HB	HB	Bulk	Bulk

What can be seen is that the control sample is in the bulk form, although expected to be in the herringbone structure. However, as it was seen in subsection 4.4.6, this could also be an issue with the solution.

The problem is that it cannot be determined whether the other samples were in bulk form prior to heating as well because no IR spectroscopy data was collected for them before heating. However, a transition from the most stable form to a kinetic phase would be very unlikely anyway.

5 Conclusions

During this thesis C_8O-BTBT-OC_8 crystals from highly and less volatile solvents were grown by evaporation of the solvent. To influence the evaporation speed the vial was either uncovered or covered by Parafilm with a small hole in it. Moreover the plain powder in solid state as well as in solution was investigated. Furthermore films of differently concentrated C_8O-BTBT-OC_8/o-xylene solutions were prepared by drop casting and spin coating. To increase the speed of the phase transition from herringbone to bulk form films were solvent vapour annealed for five days. Samples were investigated with different methods, including X-ray reflectivity, X-ray diffraction, grazing incidence X-ray diffraction, infrared and lattice phonon Raman spectroscopy, with special focus on the differentiation of the two known polymorphic phases of C_8O-BTBT-OC_8 [4] by the two latter methods.

The infrared transmission spectrum of C_8O-BTBT-OC_8 dissolved in o-xylene shows many overlapping bands of the solvent and the solute. However, some peaks can be related solely to C_8O-BTBT-OC_8, e.g. the aromatic ring–oxygen stretching vibration at $1263\,\mathrm{cm}^{-1}$. Further additional peaks show up due to the CH_3 γ vibration of the long alkyl chain. However, for most of the peaks it cannot be decided whether they are from o-xylene or C_8O-BTBT-OC_8.

Attenuated total reflection spectra of the crystals and the powder show peak shifts in the CH_3 asymmetric stretch, aromatic quadrant stretch, thiophene quad bend and aromatic C-H δ out-of-plane vibration. However, these could also be due to the pressure applied during the measurement.

Lattice phonon Raman spectroscopy shows the same spectra for the crystals grown from hexane and ethyl acetate solution, both in an uncovered vial. All other crystals have the same spectrum as the powder, however different from the two above mentioned crystals. By comparing the peak positions with results of the films it can be deduced that the crystals with the same spectrum as the powder are in the bulk form and the crystals

Table 5.1: Most prominent Raman peaks of the plain C_8O-BTBT-OC_8 powder and crystals grown from different solutions and their crystal structures.

Sample	Crystal Structure
Powder	Bulk
Crystal from	
• hexane solution, uncovered	Herringbone
• ethyl acetate solution, uncovered	Herringbone
• hexane solution, covered	Bulk
• acetone solution, uncovered	Bulk
• methanol solution, uncovered	Bulk
• chloroform solution, uncovered	Bulk
• xylene solution, uncovered	Bulk

grown from hexane and ethyl acetate solution in uncovered vials are in the herringbone structure (see Table 5.1). The formation of the herringbone structure has a kinetic reason. Due to the different evaporation speeds the material does not have enough time to go to the thermodynamically most stable form but goes to the herringbone phase instead. However, the appearance of the herringbone structure cannot simply be related to a single parameter of the solvent, more properties play a role (e.g. boiling point, vapour pressure, vapour density, seeding, atmospheric influences, . . .). In [4] the idea of the herringbone being a substrate-induced phase was discussed. However, crystals of substrate-induced phases cannot be grown. Therefore this idea does not hold anymore. Different crystal orientations and analyser/polariser combinations were used to study the influence of the anisotropy of the polarisability and the polarisation of the incident laser beam. Here only intensity differences of the peaks could be observed.

Optical microscopy images of the films prepared show highly rough surfaces with large individual crystals and exposed substrate in between. Solvent vapour annealing increases the crystallite size even more, which can also be confirmed by X-ray diffraction measurements. The absence of Kiessig fringes in X-ray reflectivity patterns and the intensity drop after the critical angle confirm the high roughness of the films. Williamson-Hall analysis gives strain values up to approximately 4×10^{-3} for the drop casted, and up to about 2.5×10^{-2} for the spin coated films. In literature strain values for organic films between 3×10^{-4} [61] and 14×10^{-3} [62] can be found. The value for the drop casted films lie in this range, one of the values of the spin coated samples is out of this range. This could be a problem due to difficult parameter extraction with the Pseudo-Voigt fits due to low signal because of the low film thickness. Lattice phonon Raman spectra of the drop casted samples show two distinct peak patterns for the as-prepared 2.7 g/L sample in the herringbone structure (peaks at 7, 19, 89 and 105 cm^{-1}) and the annealed 2.7 g/L sample in the bulk form (14 and 87 cm^{-1}). Drop casting concentrations higher than 5.4 g/L lead to films in the bulk structure, no matter if as prepared or annealed. Raman spectra could only be recorded for the thick drop casted films. Already the thickest spin coated sample with a thickness of (50 ± 15) nm does not give a sufficient signal. Also infrared spectra in the region of intramolecular vibrations can be used to determine the crystal structure. A different peak number was found in the CH_3 asymmetric stretch region for the as-prepared samples compared to the annealed films. In the aromatic quadrant stretch, thiophene quad bend and aromatic C-H δ out-of-plane region peak shifts occur for the differently treated samples (see Table 5.2). Interestingly, infrared spectroscopy can also be used on the thinner spin coated films to determine the crystal structure. An overview of all the results for the drop casted and spin coated films is given in Figure 4.21 and Figure 4.28.

Table 5.2: Overview of the peak positions (in cm^{-1}) for the annealed films in bulk phase and as-prepared films in herringbone (HB) structure for infrared spectroscopy measurements in reflection (IR R) and transmission (IR T).[a]

Method	Structure	CH_3 asy. str.	ar. quadrant str.	Thiophene quad bend	ar. C-H δ oop.
IR R	Bulk	2956, 2948	1611	831	813
	HB	2950	1605	834	815
IR T	Bulk	2956, 2948	1611	829	812
	HB	2950	1605	833	815

[a] **Abbreviations used:** ar. aromatic; asy. asymmetric; δ deformation; oop. out-of-plane; str. stretch.

Heating experiments of drop casted films in combination with X-ray diffraction measurements showed phase transitions at 99 °C and 172 °C; the films melt at 182 °C but go back to a crystalline state during cool down. Although the crystal structure of the heated films could be determined the results are, due to problems with the used solution, not trustworthy.

Abbreviations and Acronyms

AP	As Prepared
ATR	Attenuated Total Reflection
BTBT	Benzothieno-Benzothiophene
CCD	Charge-Coupled Device
DLaTGS	Deuterated L-Alanine Doped Triglycine Sulfate
FTIR	Fourier Transform Infrared
GIXD	Grazing Incidence X-Ray Diffraction
HB	Herringbone
IR	Infrared
MCT	Mercury Cadmium Telluride
SIP	Substrate-Induced Phase
SVA	Solvent Vapour Annealing/Annealed
XRD	X-Ray Diffraction
XRR	X-Ray Reflectivity

Abbreviations Used for the Description of Vibrations:

ar.	aromatic
asy.	asymmetric
δ	deformation
γ	vibration of the back bone
ip.	in-plane
oop.	out-of-plane
str.	stretch
sy.	symmetric

List of Figures

1.1 Schematic drawing of a herringbone packing, looking down the long axis of the molecule. 16
1.2 Molecular structure of C_8O-BTBT-OC_8 ($C_{30}H_{40}O_2S_2$). 17
1.3 Crystal structure and unit cell of the C_8O-BTBT-OC_8 single crystal [4]. 17

2.1 Simple mechanical model of two masses at a fixed distance r. 20
2.2 Vibrational normal modes for the linear carbon dioxide and the non linear water molecule. 23
2.3 Simple mechanical model of two masses connected by a massless spring. 23
2.4 Comparison of the potentials of the harmonic and anharmonic oscillator. 26
2.5 Schematic set-up of an infrared spectrometer with a Michelson interferometer. 28
2.6 Interferogram and resulting infrared spectrum. 30
2.7 Schematic set-up of an infrared reflectance measurement. 31
2.8 Schematic set-up of an attenuated total reflection measurement. 32
2.9 Energy levels of the sample and transitions explaining Stokes, Rayleigh and anti-Stokes scattering. 33
2.10 Comparison between Raman scattering, absorption/fluorescence and infrared absorption process. 35
2.11 Schematic set-up of a Raman spectrometer and combination with a microscope. 36
2.12 Beam paths in an X-ray reflectivity measurement and resulting diffraction pattern and information gained from it. 38
2.13 Graphical representation of a Williamson-Hall analysis. Dots represent the $\Delta(2\theta)\cos\theta$ values of the peaks in the X-ray diffraction measurement, the red line is a linear fit. 39

3.1 Drawing of the beam path in the Bruker IFS 66v/S. 42
3.2 Used transmission and reflection set-up for the Bruker IFS 66v/S infrared spectrometer. 43
3.3 Schematic of the beam paths in a Bomem MB-102 infrared spectrometer. 44

3.4 Images of the HORIBA Jobin-Yvon T64000 Triple Monochromator Raman microscope equipped with the detector with Peltier cooling. 47

4.1 Raman spectra of untreated and grinded C_8O-BTBT-OC_8 in the region of the lattice phonons. 52
4.2 Intramolecular modes of the Raman spectrum of C_8O-BTBT-OC_8. . . . 53
4.3 Attenuated total reflection spectrum of the plain C_8O-BTBT-OC_8 powder. Zoomed into the region of the C-H stretches and the fingerprint region. 55
4.4 Infrared transmission spectrum of the C_8O-BTBT-OC_8 potassium bromide pellet. Zoomed into the region of the C-H stretches and the fingerprint region. 56
4.5 Infrared transmission spectrum of the KBr pellet showing an inverted peak due to multiple reflections at the parallel surfaces of the sample. . 57
4.6 Fingerprint region of the infrared absorption spectrum of C_8O-BTBT-OC_8 in o-xylene compared to a literature spectrum of pure o-xylene. 58
4.7 Optical microscopy images of C_8O-BTBT-OC_8 crystals grown from different solutions in covered or uncovered vials. 59
4.8 Raman spectra of the crystal grown in an uncovered vial from the hexane solution in the anti- and Stokes region. 61
4.9 Raman spectra of the crystal grown in an uncovered vial from the hexane solution with 0, 45 and 90° sample orientation compared to the plain C_8O-BTBT-OC_8 powder spectrum. 62
4.10 Raman spectra of the crystal grown in an uncovered vial from the hexane solution at different orientations and with different polarisation directions of the incoming laser beam. 62
4.11 Overview of the Raman spectra of the crystals grown from different solvent in uncovered or covered vials. 63
4.12 Attenuated total reflection spectra of the C_8O-BTBT-OC_8 powder, the crystal from hexane solution (covered) and from ethyl acetate solution (uncovered) in the CH_3 asymmetric stretch, aromatic quadrant stretch and thiophene quad bend and aromatic C-H δ out-of-plane region. . . . 64
4.13 X-ray diffraction patterns of drop casted samples. 66
4.14 Interplanar distance d_{001} for drop casted samples of different concentrations. 67
4.15 Crystallite size perpendicular to the surface D for drop casted samples of different concentrations. 68
4.16 Results of the Williamson-Hall analysis for the drop casted samples. . . 69
4.17 Integrated grazing incidence X-ray diffraction images, showing the positions of rods. 70
4.18 Raman spectra of drop casted samples compared to the spectra of the crystal from covered hexane and uncovered ethyl acetate solution. . . . 72

4.19 Infrared reflection spectra of some drop casted samples in the CH_3 asymmetric stretch, aromatic quadrant stretch and thiophene quad bend and aromatic C-H δ out-of-plane region. 73
4.20 Infrared transmission spectra of some drop casted samples in the CH_3 asymmetric stretch, aromatic quadrant stretch and thiophene quad bend and aromatic C-H δ out-of-plane region. 74
4.21 Overview of the results for the drop casted samples. 76
4.22 X-ray diffraction patterns of drop casted samples. 77
4.23 Interplanar distance d_{001} and crystallite size perpendicular to the surface D for spin coated samples of different concentrations. 78
4.24 Results of the Williamson-Hall analysis for the spin coated samples. . . 79
4.25 Raman spectra of the two thickest spin coated samples compared to the spectrum of a clean substrate. 80
4.26 Infrared reflection spectra of some of the spin coated samples. 81
4.27 Infrared transmission spectra of some of the spin coated samples. . . . 82
4.28 Overview of the results for the spin coated samples. 83
4.29 Heating to 99 °C and cooling down again. 85
4.30 Heating to 182 °C and cooling down again. 85

A.1 Calculated infrared spectrum compared to the measurement of the potassium bromide pellet with C_8O-BTBT-OC_8. 105
A.2 Calculated Raman spectrum compared to the measurement of the polycrystalline C_8O-BTBT-OC_8 powder. 106

List of Tables

1.1 Unit-cell parameters of the two known crystal structures of C_8O-BTBT-OC_8. 18

3.1 Main OPUS settings used for recording infrared spectra with the Bruker IFS 66v/S. 42

4.1 Most prominent Raman peaks of the plain C_8O-BTBT-OC_8 powder and crystals grown from different solutions and boiling points T_{boil} of the used solvents. 65
4.2 Crystal size perpendicular to the sample surface resulting from the Williamson-Hall analysis. 68
4.3 Rod positions in films of C_8O-BTBT-OC_8 and the corresponding crystal structures [4]. 71
4.4 Crystal size perpendicular to the sample surface resulting from the Williamson-Hall analysis. 80
4.5 Overview of the peak positions obtained during X-ray diffraction measurements at different temperatures of the samples heated to 99, 172 and 182°. 84

5.1 Most prominent Raman peaks of the plain C_8O-BTBT-OC_8 powder and crystals grown from different solutions and their crystal structures. . . 88
5.2 Overview of the peak positions (in cm^{-1}) for the annealed films in bulk phase and as-prepared films in herringbone structure for infrared spectroscopy measurements in reflection and transmission. 89

Bibliography

[1] T. L. Threlfall. Analysis of organic polymorphs. A review. *The Analyst* 120.10 (1995).

[2] R. G. Della Valle, A. Brillante, E. Venuti, L. Farina, A. Girlando, and M. Masino. Exploring the polymorphism of crystalline pentacene. *Organic Electronics* 5.1-3 (Mar. 2004).

[3] C. C. Mattheus, A. B. Dros, J. Baas, A. Meetsma, J. L. d. Boer, and T. T. M. Palstra. Polymorphism in pentacene. *Acta Crystallographica Section C Crystal Structure Communications* 57.8 (Aug. 15, 2001).

[4] A. O. F. Jones, Y. H. Geerts, J. Karpinska, A. R. Kennedy, R. Resel, C. Röthel, C. Ruzié, O. Werzer, and M. Sferrazza. Substrate-Induced Phase of a [1]Benzothieno[3,2-*b*]benzothiophene Derivative and Phase Evolution by Aging and Solvent Vapor Annealing. *ACS Applied Materials & Interfaces* 7.3 (Jan. 28, 2015).

[5] B. Wedl, R. Resel, G. Leising, B. Kunert, I. Salzmann, M. Oehzelt, N. Koch, A. Vollmer, S. Duhm, O. Werzer, G. Gbabode, M. Sferrazza, and Y. Geerts. Crystallisation kinetics in thin films of dihexyl-terthiophene: the appearance of polymorphic phases. *RSC Advances* 2.10 (2012).

[6] A. Brillante, I. Bilotti, R. G. Della Valle, E. Venuti, and A. Girlando. Probing polymorphs of organic semiconductors by lattice phonon Raman microscopy. *CrystEngComm* 10.8 (2008).

[7] R. J. Mesley, R. L. Clements, B. Flaherty, and K. Goodhead. The polymorphism of phenobarbitone. *Journal of Pharmacy and Pharmacology* 20.5 (May 1968).

[8] T. J. Cholerton, J. H. Hunt, G. Klinkert, and M. Martin-Smith. Spectroscopic studies on ranitidine–its structure and the influence of temperature and pH. *Journal of the Chemical Society, Perkin Transactions 2* 11 (1984).

[9] C. Westermeier, A. Cernescu, S. Amarie, C. Liewald, F. Keilmann, and B. Nickel. Sub-micron phase coexistence in small-molecule organic thin films revealed by infrared nano-imaging. *Nature Communications* 5 (June 11, 2014).

[10] N. Koch, A. Vollmer, I. Salzmann, B. Nickel, H. Weiss, and J. P. Rabe. Evidence for Temperature-Dependent Electron Band Dispersion in Pentacene. *Physical Review Letters* 96.15 (Apr. 19, 2006).

[11] Y. Hosoi, K. Okamura, Y. Kimura, H. Ishii, and M. Niwano. Infrared spectroscopy of pentacene thin film on SiO_2 surface. *Applied Surface Science* 244.1-4 (May 2005).

[12] H. Ebata, T. Izawa, E. Miyazaki, K. Takimiya, M. Ikeda, H. Kuwabara, and T. Yui. Highly Soluble [1]Benzothieno[3,2-*b*]benzothiophene (BTBT) Derivatives for High-Performance, Solution-Processed Organic Field-Effect Transistors. *Journal of the American Chemical Society* 129.51 (Dec. 2007).

[13] T. Uemura, Y. Hirose, M. Uno, K. Takimiya, and J. Takeya. Very High Mobility in Solution-Processed Organic Thin-Film Transistors of Highly Ordered [1]Benzothieno[3,2-*b*]benzothiophene Derivatives. *Applied Physics Express* 2.11 (Nov. 6, 2009).

[14] H. Iino, T. Kobori, and J.-i. Hanna. Improved Thermal Stability in Organic FET Fabricated with a Soluble BTBT Derivative. *Journal of Non-Crystalline Solids* 358.17 (Sept. 2012).

[15] T. Izawa, E. Miyazaki, and K. Takimiya. Molecular Ordering of High-Performance Soluble Molecular Semiconductors and Re-evaluation of Their Field-Effect Transistor Characteristics. *Advanced Materials* 20.18 (July 30, 2008).

[16] G. De Luca, E. Treossi, A. Liscio, J. M. Mativetsky, L. M. Scolaro, V. Palermo, and P. Samorì. Solvent Vapour Annealing of Organic Thin Films: Controlling the Self-Assembly of Functional Systems across Multiple Length Scales. *Journal of Materials Chemistry* 20.13 (2010).

[17] K. C. Dickey, J. E. Anthony, and Y.-L. Loo. Improving Organic Thin-Film Transistor Performance through Solvent-Vapor Annealing of Solution-Processable Triethylsilylethynyl Anthradithiophene. *Advanced Materials* 18.13 (July 4, 2006).

[18] P. Larkin. *Infrared and Raman Spectroscopy: Principles and Spectral Interpretation.* Amsterdam; Boston: Elsevier, 2011.

[19] E. Lindner. IR-Spektroskopie. *Untersuchungsmethoden in der Chemie – Einführung in die moderne Analytik.* 2., durchgesehene Auflage. Stuttgart New York: Georg Thieme Verlag, 1990.

[20] M. Adelhelm. Ramanspektroskopie. *Untersuchungsmethoden in der Chemie – Einführung in die moderne Analytik.* 2., durchgesehene Auflage. Stuttgart New York: Georg Thieme Verlag, 1990.

[21] M. Birkholz, P. F. Fewster, and C. Genzel. *Thin Film Analysis by X-Ray Scattering.* Weinheim: Wiley-VCH, 2006.

[22] D. W. Bennett. *Understanding Single-Crystal X-Ray Crystallography.* Weinheim: Wiley-VCH, 2010.

[23] R. Resel. Slides for the Lecture “X-Ray Physics”. Technische Universität Graz, 2014.

[24] I. Martinson and L. J. Curtis. Janne Rydberg – his life and work. *Nuclear Instruments and Methods in Physics Research Section B: Beam Interactions with Materials and Atoms* 235.1-4 (July 2005).

[25] P. J. Mohr, B. N. Taylor, and D. B. Newell. CODATA Recommended Values of the Fundamental Physical Constants: 2010. *Reviews of Modern Physics* 84.4 (Nov. 13, 2012).

[26] L. Windholz. *Arbeitsunterlagen zur Vorlesung „Experimentelle Methoden der Spektroskopie, Quantenoptik und Quantenmeßtechnik“.* SS 2013. Institut für Experimentalphysik der Technischen Universität Graz.

[27] W. Nolting. *Quantenmechanik – Grundlagen.* 7., aktualisierte Auflage. Berlin: Springer, 2009.

[28] P. M. Morse. Diatomic Molecules According to the Wave Mechanics. II. Vibrational Levels. *Physical Review* 34.57 (July 1, 1929).

[29] E. Pretsch, P. Bühlmann, and M. Badertscher. *Spektroskopische Daten zur Strukturaufklärung organischer Verbindungen.* Berlin, Heidelberg: Springer, 2010.

[30] Gasesmag. *Infrared Spectroscopy.* URL: `http://www.gasesmag.com/Assets/images/0109/art3fig10.gif` (visited on Oct. 20, 2014).

[31] Bruker. *Spectroscopic Software OPUS Reference Manual.*

[32] PIKE Technologies. *Calculating the Thickness of Free-Standing Films by FTIR.* URL: `http://www.piketech.com/skin/fashion_mosaic_blue/application-pdfs/CalculatingThickness-FreeStandingFilms-byFTIR.pdf`.

[33] E. Gilli and R. Schennach. Detection of Coatings on Paper Using Infra Red Spectroscopy. *Lenzinger Berichte.* Vol. 87. 2009.

[34] J. Mistry. Review: ATR-IR Spectroscopy for the Coatings Industry. *Missouri S&T Coatings Institute Newsletters* 6.3 (2010).

[35] A. Smekal. Zur Quantentheorie der Dispersion. *Die Naturwissenschaften* 11.43 (Oct. 1923).

[36] C. V. Raman. A new radiation. *Indian Journal of Physics* 2 (Mar. 16, 1928).

[37] G. Landsberg and L. Mandelstam. Eine neue Erscheinung bei der Lichtzerstreuung in Krystallen. *Die Naturwissenschaften* 16.28 (July 1928).

[38] Nobel Media AB. *The Nobel Prize in Physics 1930.* URL: `http://www.nobelprize.org/nobel_prizes/physics/laureates/1930/index.html` (visited on July 24, 2015).

[39] B. B. Johnson and W. L. Peticolas. The Resonant Raman Effect. *Annual Review of Physical Chemistry* 27.1 (Oct. 1976).

[40] A. Brillante, I. Bilotti, C. Albonetti, J.-F. Moulin, P. Stoliar, F. Biscarini, and D. M. de Leeuw. Confocal Raman Spectroscopy of α-Sexithiophene: From Bulk Crystals to Field-Effect Transistors. *Advanced Functional Materials* 17.16 (Nov. 5, 2007).

[41] T. Salzillo. *Lattice phonons and XRD: a synergy for structure identification. Application to 9-anthracene-carboxylic acid (Poster PLC workshop).* 2013.

[42] W. H. Bragg and W. L. Bragg. The Reflection of X-rays by Crystals. *Proceedings of the Royal Society A: Mathematical, Physical and Engineering Sciences* 88.605 (July 1, 1913).

[43] P. Scherrer. Bestimmung der Größe und der inneren Struktur von Kolloidteilchen mittels Röntgenstrahlen. *Nachrichten von der Gesellschaft der Wissenschaften zu Göttingen, Mathematisch-Physikalische Klasse* 1918 (1918).

[44] H. Kiessig. Interferenz von Röntgenstrahlen an dünnen Schichten. *Annalen der Physik* 402.7 (1931).

[45] G. K. Williamson and W. H. Hall. X-Ray Line Broadening from Filed Aluminium and Wolfram. *Acta Metallurgica* 1.1 (Jan. 1953).

[46] U. Sharma. *Infra-red detectors.* M. Tech Credit Seminar Report. https://www.ee.iitb.ac.in/~esgroup/es_mtech04_sem/es_mtech04_sem.htm. Electronic Systems Group, EE Dept, IIT Bombay, Oct. 2004.

[47] J. M. Chalmers. Mid-Infrared Spectroscopy: Anomalies, Artifacts and Common Errors. *Handbook of Vibrational Spectroscopy.* Ed. by J. M. Chalmers and P. R. Griffiths. Chichester, UK: John Wiley & Sons, Ltd, Aug. 15, 2006.

[48] ABB Laboratory Spectrometers. *FT-IR Reference Manual.* Aug. 2003.

[49] National Institute of Standards and Technology. *Strong Lines of Neon (Ne).* June 25, 2015. URL: `http://physics.nist.gov/PhysRefData/Handbook/Tables/neontable2.htm` (visited on June 25, 2015).

[50] D. Kriegner, E. Wintersberger, and J. Stangl. *xrayutilities*: a versatile tool for reciprocal space conversion of scattering data recorded with linear and area detectors. *Journal of Applied Crystallography* 46.4 (Aug. 1, 2013).

[51] F. Friedrich and P. G. Weidler. Contact Pressure Effects on Vibrational Bands of Kaolinite During Infrared Spectroscopic Measurements in a Diamond Attenuated Total Reflection Cell. *Applied Spectroscopy* 64.5 (May 2010).

[52] National Institute of Standards and Technology. *Infrared Spectrum of o-Xylene.* July 17, 2015. URL: `http://webbook.nist.gov/cgi/cbook.cgi?ID=C95476\&Type=IR-SPEC\&Index=2#IR-SPEC` (visited on July 17, 2015).

[53] Pubchem. *Physical Properties of Chloroform.* URL: `http://pubchem.ncbi.nlm.nih.gov/compound/chloroform` (visited on July 20, 2015).

[54] Pubchem. *Physical Properties of n-Hexane.* URL: `http://pubchem.ncbi.nlm.nih.gov/compound/hexane` (visited on July 20, 2015).

[55] Pubchem. *Physical Properties of Ethyl Acetate.* URL: `http://pubchem.ncbi.nlm.nih.gov/compound/ethyl_acetate` (visited on July 20, 2015).

[56] Pubchem. *Physical Properties of Acetone.* URL: `http://pubchem.ncbi.nlm.nih.gov/compound/acetone` (visited on July 20, 2015).

[57] Pubchem. *Physical Properties of Methanol.* URL: `http://pubchem.ncbi.nlm.nih.gov/compound/methanol` (visited on July 20, 2015).

[58] Pubchem. *Physical Properties of o-Xylene.* URL: `http://pubchem.ncbi.nlm.nih.gov/compound/o-xylene` (visited on July 20, 2015).

[59] J. D. Dunitz and J. Bernstein. Disappearing Polymorphs. *Accounts of Chemical Research* 28.4 (Apr. 1995).

[60] M. Wojdyr. Fityk: a General-Purpose Peak Fitting Program. *Journal of Applied Crystallography* 43.5 (Oct. 1, 2010).

[61] H.-J. Brandt, R. Resel, J. Keckes, B. Koppelhuber-Bitschnau, N. Koch, and G. Leising. Determination of Crystallite Size and Lattice Strain in Hexaphenyl Thin Films by Line Profile Analysis. *MRS Proceedings* 561 (Jan. 1999).

[62] M. Oehzelt, G. Koller, J. Ivanco, S. Berkebile, T. Haber, R. Resel, F. P. Netzer, and M. G. Ramsey. Organic Heteroepitaxy: p-Sexiphenyl on Uniaxially Oriented α-Sexithiophene. *Advanced Materials* 18.18 (Sept. 18, 2006).

[63] A. Moser. Crystal Structure Solution Based on Grazing Incidence X-ray Diffraction: Software Development and Application to Organic Films. PhD thesis. Graz University of Technology, May 2012.

Appendix

A.1 Calculation of Infrared and Raman Spectra

Raman and IR spectra were calculated with `Gaussian 09` using the 6-31G basis set. The resulting IR spectrum, compared to the measurement of the KBr pellet, is shown in Figure A.1. Especially in the high wavenumber region a shift of the calculated frequencies to higher values can be observed. For example, the C-H valence vibrations, experimentally observed slightly below 3000 cm^{-1}, are above this value in the calculation. For lower wavenumbers the shift is decreasing. One reason for the difference between experiment and calculation is that for the calculation isolated C_8O-BTBT-OC_8 molecules

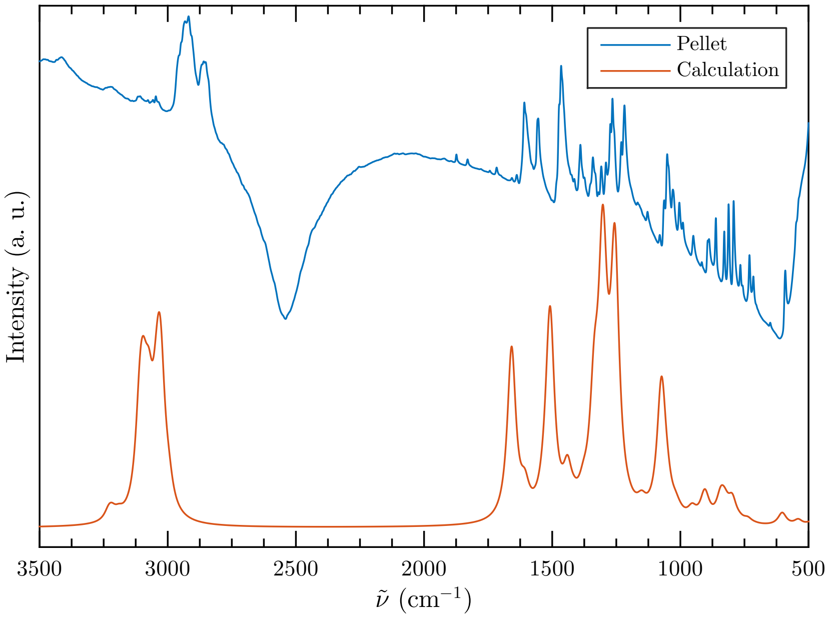

Figure A.1: Calculated infrared spectrum compared to the measurement of the potassium bromide pellet with C_8O-BTBT-OC_8.

were used. Furthermore the simplification introduced using the basic 6-31G basis set results in a shift as well.

Figure A.2 shows the calculated Raman spectrum compared to that of the experimentally determined spectrum. Again, a shift due to the same reasons as described for the IR spectrum can be observed. However, also the experimental data is shifted slightly. Due to limited range of the Raman spectrometer the measurement window had to be changed during the measurement. This leads to a shift in the horizontal axis as well. Removing this error source requires a measurement of the individual ranges followed by a measurement of the Ne lines to align them correctly (as described in subsection 3.4.1).

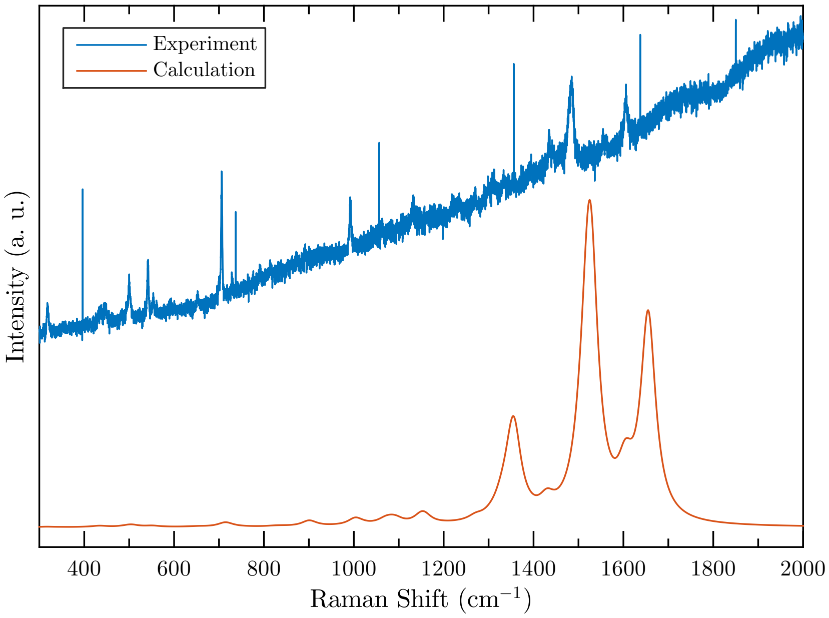

Figure A.2: Calculated Raman spectrum compared to the measurement of the polycrystalline C_8O-BTBT-OC_8 powder.